UNIVERSITY OF CALIFORNIA SAN DIEGO

Satellite and airborne observations of ocean-driven mass-balance processes on Ross Ice Shelf, Antarctica

A dissertation submitted in partial satisfaction of the
requirements for the degree
Doctor of Philosophy

in

Oceanography

by

Maya Karina Becker

Committee in charge:

Helen Amanda Fricker, Chair
Adrian Borsa
Jennifer Burney
Ian Eisenman
Laurie Padman
Fiamma Straneo

2023

The dissertation of Maya Karina Becker is approved, and it is acceptable in quality and form for publication on microfilm and electronically.

University of California San Diego

2023

DEDICATION

To Drake

EPIGRAPH

By all means, move at a glacial pace.

You know how that thrills me.

—Miranda Priestly (portrayed by Meryl Streep)

in *The Devil Wears Prada* (2006)

TABLE OF CONTENTS

LIST OF FIGURES

LIST OF TABLES

ACKNOWLEDGEMENTS

I was fortunate to meet, learn from, and laugh with many wonderful people during my graduate school career. I am sure that I will miss someone here—there are simply too many people to thank.

First, I am incredibly grateful to my advisor and committee chair, Helen Amanda Fricker, for making my decision to come to Scripps so easy and a great one. Beyond the tremendous scientific guidance and opportunities that she gave me, I feel so lucky to have had her as a role model, a mentor, and an advocate. I am thankful to Helen and her family for always making me feel welcome and appreciated. Thank you to my unofficial co-advisor, Laurie Padman, for sharing so much of his time and vast knowledge with me. I tried desperately to be a sponge during each and every one of our conversations.

I am thankful to my entire committee for their remarkable wisdom and generosity, as well as their flexibility while I navigated the path to graduating. I have learned a great deal from Adrian Borsa about geophysics and what it means to be a good person, and I am thankful to him for always supporting my non-academic career goals. I so admire Jen Burney's intelligence, kindness, and ability to respond to emails quickly. I have enjoyed many long conversations about science and life with Ian Eisenman, and I thanked myself throughout the first year for taking his MATLAB class right when I moved to San Diego. Thank you to Fiamma Straneo for her honesty, patience, and warmth, especially during a hard moment for me when we were in Greenland together. I also had a great time chicken- and Maple-sitting for her and her lovely family!

Thank you to my professors at Columbia and Scripps who helped me get to and through graduate school, especially Frank Nitsche, who introduced me to Antarctic science during my senior thesis project. I am thankful to my rockstar coauthors and collaborators—including Robin Bell, Isabel Cordero, Indrani Das, Helen, Susan Howard, Cyrille Mosbeux, Laurie, Matt Siegfried, Kirsty Tinto, and Till Wagner—for helping me become a better scientist and writer. Some of my best graduate school memories are from the field. I participated in two incredible field seasons at

McMurdo Station, Antarctica, with the awesome and dynamic ROSETTA-Ice team. I will not soon forget my friendships from the Arctic Glacier Field Course in Qeqertarsuaq, Greenland, and the International Summer School in Glaciology in McCarthy, Alaska. I am grateful to Helen, Fiamma, and everyone else who made those experiences (and the science!) possible.

Helen and Fiamma have fostered a supportive and productive Ice–Ocean group within the Scripps Polar Center, and I have enjoyed sharing science, coffee, and treats with its current and former members. Helen's other students and postdocs—including Susheel Adusumilli, Cyrille, Fernando Paolo, and Matt—have been a terrific resource to me throughout my academic journey, and I am grateful to them for never tiring of my pestering questions. Thank you to everyone who works tirelessly to enable and promote IGPP and Scripps science, especially Gilbert Bretado, Christine Coulibaly, Rob Monroe, and Shelley Weisel. I must also thank Rob and the rest of the Scripps Communications Office for allowing me and many other students to attend United Nations Climate Change Conferences, which were truly eye-opening experiences.

Toward the end of my time at Scripps, I was fortunate to be awarded a Sea Grant Knauss Fellowship and be placed in the Office of U. S. Senator Lisa Murkowski. I am indebted to California Sea Grant, the National Sea Grant Office, my fellow fellows, my colleagues in Senator Murkowski's office (especially "Team Ocean," a.k.a. Carly Besh, Abbie Lyons, Cristina Nelson, and Jamie O'Connor), the many Alaskans I met, and Senator Murkowski for a year of immense personal and professional growth.

I cannot imagine a better, more passionate, and more thoughtful community of people than the Scripps graduate student community. The 2015 Geophysics cohort—which included Susheel, Daniel Blatter, Thomas Chaparro, Chloe Gustafson, and Drake Singleton—is a prime example of this. They quite literally got me through the first year, and I look forward to many more reunions with them and honorary members Derek Alcorn and Jenny Lewis. I will always think fondly of time spent with my San Diego roommates (Meredith Fish Farrell, Camille Pagniello, Drake, and Kara Voss), office-mates (including Susheel and Jessie Saunders), and MESOM-Basement-mates

(Susheel, Margaret Lindeman, Bobby Sanchez, and often Chloe and Zoe Yin). Thank you to my peer mentor, Dara Goldberg, and the many other current and former Scripps students who mentored me more informally. I am also grateful for the support and friendship of Sureena Basra, Matt Cook, Will Cyr, Adrian Doran, Patrick Farrell, Dan Flanigan, Elizabeth Howland, Wesley Neely, and Olivia Padilla Neely. A special thank-you to Susheel and Meredith for helping to boost my confidence these last few years—I don't know what I would have done without them.

I appreciate my childhood and college friends for taking an interest in my work and cheering me on from afar (and, in some cases, coming to visit me in California!). Thank you to my soon-to-be family—especially Sheila, Mark, and Renata—and sweet Layla for their constant encouragement. It has been a source of comfort and happiness to live close to Mark and Renata these last few years. Thank you to my Aunt Julie for showing me what it means to be strong and for never judging me. I always benefited from Oma's pep talks (particularly the one the day before my defense) and open arms, and I only wish that Opa could have seen me graduate. My parents have been my scientific inspiration since day one. I can't thank them enough for their unwavering support and love.

Finally, to Drake, without whom I would not have gotten to this point: Meeting you was the highlight of all of the highlights of my time at Scripps. I am so excited to experience life beyond graduate school with you!

Chapter 2 is coauthored with Fricker, H. A., Padman, L., Cordero, S. I., Das., I., Tinto, K. J., Bell, R. E., Mosbeux, C., & Wagner, T. J. W. The dissertation author was the primary investigator and author of this material.

Chapter 3, in full, is a reprint of the material as it appears in the journal *Geophysical Research Letters*. Becker, M. K., Howard, S. L., Fricker, H. A., Padman, L., Mosbeux, C., & Siegfried, M. R. (2021). Buoyancy-driven flexure at the front of Ross Ice Shelf, Antarctica, observed with ICESat-2 laser altimetry. *Geophysical Research Letters*, *48*(12), e2020GL091207. doi: 10.1029/2020GL091207. The dissertation author was the primary investigator and author of

this paper.

Chapter 4, in part, is currently being prepared for submission for publication of the material. Becker, M. K., Fricker, H. A., Padman, L., Howard, S. L., & Siegfried, M. R. The dissertation author was the primary investigator and author of this material.

VITA

2015	B. A. in Earth Science with a Special Concentration in Sustainable Development *magna cum laude*, Columbia College, Columbia University
2016	M. S. in Earth Sciences, University of California San Diego
2019	Teaching assistant, University of California San Diego
2015–2021	Graduate student researcher, University of California San Diego
2021–2022	NOAA Sea Grant John A. Knauss Marine Policy Fellow, Office of U. S. Senator Lisa Murkowski
2022–2023	Graduate student researcher, University of California San Diego
2023	Ph. D. in Oceanography, University of California San Diego

PUBLICATIONS

Tinto, K. J., Padman, L., Siddoway, C. S., Springer, S. R., Fricker, H. A., Das, I., Caratori Tontini, F., Porter, D. F., Frearson, N. P., Howard, S. L., Siegfried, M. R., Mosbeux, C., **Becker, M. K.**, Bertinato, C., Boghosian, A., Brady, N., Burton, B. L., Chu, W., Cordero, S. I., Dhakal, T., Dong, L., Gustafson, C. D., Keeshin, S., Locke, C., Lockett, A., O'Brien, G., Spergel, J. J., Starke, S. E., Tankersley, M., Wearing M. G., & Bell, R. E. (2019). Ross Ice Shelf response to climate driven by the tectonic imprint on seafloor bathymetry. *Nature Geoscience*, *12*(6), 441–449. doi: 10.1038/s41561-019-0370-2

Boghosian, A. L., Pratt, M. J., **Becker, M. K.**, Cordero, S. I., Dhakal, T., Kingslake, J., Locke, C. D., Tinto, K. J., & Bell, R. E. (2019). Inside the ice shelf: Using augmented reality to visualise 3D lidar and radar data of Antarctica. *The Photogrammetric Record*, *34*(168), 346–364. doi: 10.1111/phor.12298

Mosbeux, C., Wagner, T. J. W., **Becker, M. K.**, & Fricker, H. A. (2020). Viscous and elastic buoyancy stresses as drivers of ice-shelf calving. *Journal of Glaciology*, *66*(258), 643–657. doi: 10.1017/jog.2020.35

Walker, C. C., **Becker, M. K.**, & Fricker, H. A. (2021). A high resolution, three-dimensional view of the D-28 calving event from Amery Ice Shelf with ICESat-2 and satellite imagery. *Geophysical Research Letters*, *48*(3), e2020GL091200. doi: 10.1029/2020GL091200

Becker, M. K., Howard, S. L., Fricker, H. A., Padman, L., Mosbeux, C., & Siegfried, M. R. (2021). Buoyancy-driven flexure at the front of Ross Ice Shelf, Antarctica, observed with ICESat-2 laser altimetry. *Geophysical Research Letters*, *48*(12), e2020GL091207. doi: 10.1029/2020GL091207

ABSTRACT OF THE DISSERTATION

Satellite and airborne observations of ocean-driven mass-balance processes on Ross Ice Shelf, Antarctica

by

Maya Karina Becker

Doctor of Philosophy in Oceanography

University of California San Diego, 2023

Helen Amanda Fricker, Chair

Increasing mass loss from the Antarctic Ice Sheet has contributed to recent acceleration in the rate of global mean sea-level rise (SLR). Its full SLR potential is ∼58 m, and its future contribution remains highly uncertain. The flow of Antarctica's grounded ice into the ocean, and thus its contribution to SLR, is regulated by buttressing from floating ice shelves. Ice-shelf mass loss can reduce this buttressing effect. In this dissertation, I used satellite and airborne remote sensing data to explore three processes by which the ocean drives mass change on Antarctica's large Ross Ice Shelf (RIS).

First, I compared RIS thicknesses estimated from satellite laser altimetry and ROSETTA-

Ice airborne radar data to identify a potential area of basal marine-ice accretion (i.e., local mass gain) in the ice-shelf interior. Large uncertainties prevent a definitive conclusion; reducing uncertainties will require additional measurements of ice-column density and firn properties. Second, I showed that airborne radar thickness profiles capture near-front thinning of RIS associated with basal melting by seasonally warmed upper-ocean water.

Finally, I investigated the bending of the RIS front due to buoyancy created by the melting-related development of a submerged bench of ice, a mechanism that may lead to mass loss by calving of small icebergs. Profiles of the ice-shelf surface height from two satellite laser altimetry missions (ICESat, 2003–2009; and ICESat-2, 2018–present) reveal that this bending is larger on the eastern section of the RIS front, reflecting along-front variability in near-front ice thickness and ocean conditions. I also found that the surface deformation increased overall between 2018 and 2022. Between the two satellite mission periods, these surface structures grew along sections of the RIS front that experienced large calving events in the early 2000s.

Taken together, these studies demonstrate that important mass-balance processes at the interface of ice shelf and ocean occur at small spatial scales that can only be resolved over large areas by high-resolution satellite and airborne sensors. Better understanding of these processes will require a combination of improved data density and models that correctly represent ocean properties and ice mechanical processes.

Chapter 1

Introduction

1.1 Motivation and background

1.1.1 The Antarctic Ice Sheet and sea-level rise

Global mean sea level has been rising at a rate of $\sim 3 \pm 0.4$ mm a^{-1} since 1993 (Nerem et al., 2018), leading to significant consequences and risks for coastal societies and ecosystems (Oppenheimer et al., 2019). Ocean thermal expansion and mass loss from ice sheets, mountain glaciers, and ice caps have accounted for nearly all of this trend. Between 1993 and 2017, the rate of global mean sea-level rise accelerated by 0.084 ± 0.025 mm a^{-2} due to climate change (Nerem et al., 2018); mass loss from Antarctica, which contains enough ice to raise global sea level by 57.9 ± 0.9 m (Morlighem et al., 2020; Figure 1.1), contributed the most to this acceleration. However, the potential for nonlinear Antarctic response to climate warming leads to large uncertainties around Antarctica's future contribution to sea-level rise.

The scientific community reduced the uncertainty associated with projections of Antarctica's contribution to sea-level rise for the period 2081–2100 and the year 2100 between the publication of the Intergovernmental Panel on Climate Change (IPCC) fourth assessment report (AR4) in 2007 (IPCC, 2007) and that of the IPCC Special Report on the Ocean and Cryosphere

in a Changing Climate (SROCC) in 2019 (Abram et al., 2019; Meredith et al., 2019). The uncertainty reduction achieved prior to the publication of the SROCC stemmed from increased modern and geological observational evidence for, and improved model representations of, a proposed mechanism known as the marine ice-sheet instability (MISI; e.g., Schoof et al., 2007). Through this process, an ice sheet that is grounded below sea level can experience runaway retreat if it encounters bedrock that slopes downward toward the ice-sheet interior. Much of the West Antarctic Ice Sheet (WAIS), which is driving most current Antarctic ice loss (Shepherd et al., 2018), is grounded below sea level, meaning it could be especially vulnerable to MISI. Some observational (Rignot et al., 2014) and modeling (Joughin et al., 2014) results suggest that MISI-like retreat is already occurring there.

Despite this progress in understanding and representing MISI, confidence in long-term sea-level projections is limited by remaining questions about the timescale and future pace of glacier retreat in some parts of Antarctica (Meredith et al., 2019). The SROCC and the IPCC AR6 (Fox-Kemper et al., 2021) reported that projections of Antarctic sea-level rise beyond 2100 and the probability that sea-level rise would exceed that within the "likely" (i.e., the 17–83% probability) range before 2100 are marked by "deep uncertainty" because of insufficient process knowledge and lack of consensus on the uncertainty probability distributions (Abram et al., 2019). Accurately predicting future sea-level change for community-level adaptation is already a complicated task without this uncertainty due to the unequal distribution of ice-sheet meltwater across the world's oceans (e.g., Mitrovica et al., 2011). Coastal communities must also consider the interaction of the regional long-term sea-level trend with more dynamic local factors, including tides, storm surge, waves, river discharge, and seasonal water-level fluctuations, which can render those communities even more vulnerable to inundation (Barnard et al., 2019).

Much of the outstanding uncertainty in sea-level projections is associated with another proposed mechanism for sustained retreat of marine ice sheets, the marine ice-cliff instability (MICI). This instability initiates when near-vertical ice cliffs at the interface with the ocean

collapse under their own weight (Bassis and Walker, 2012). The inclusion of MICI in an ice-sheet model (DeConto and Pollard, 2016) led to a prediction that Antarctica could contribute 1+ m of sea-level rise by 2100. There is only limited, indirect evidence that MICI occurred in Antarctica in the past (e.g., Wise et al., 2017) and could be presently underway in Antarctica and Greenland (Edwards et al., 2019). Nevertheless, the high sea-level rise projections associated with MICI highlight the importance of understanding processes at the interface between Antarctic ice and the Southern Ocean, as well as processes that could lead to the exposure of ice cliffs.

1.1.2 The role of ice shelves in Antarctic mass balance

The contribution of the Antarctic Ice Sheet to sea level is controlled by its mass balance over any given time interval. For the grounded portion of the ice sheet, this balance reflects mass gain through net snow accumulation on its surface and mass loss through meltwater runoff and discharge into the ocean. Ice flows under its own weight from the ice-sheet interior to its margins. When it reaches the ocean, the ice can start to float if topography and water temperature allow, forming the ice shelves (Figure 1.1) that border 75% of Antarctica's coastline (Rignot et al., 2013). Most Antarctic ice flows across the grounding line (the point at which the ice transitions from grounded to floating; Figure 1.2) and through the ice shelves before it eventually enters the Southern Ocean.

Ice shelves lose mass through ocean-driven melting of their bases and iceberg calving, with basal melting responsible for slightly more than half of continent-wide ice-shelf mass loss averaged over several decades (Rignot et al., 2013; Depoorter et al., 2013; Greene et al., 2022). Ice shelves are important structural elements of the Antarctic Ice Sheet, as they regulate the flow of grounded ice, and thus the ice sheet's contribution to global sea level, by generating back stresses from contact with sidewalls or bathymetric highs in the seafloor. They play a key role in the evolution of the ice sheet, and its susceptibility to MISI and MICI, through this "buttressing" effect (Thomas et al., 1979; Dupont and Alley, 2005). This effect disappears when ice shelves

disintegrate, leading to the retreat and speedup of upstream glaciers, as occurred following the collapses of Larsen A and B ice shelves (Rott et al., 2002; Scambos et al., 2004). The thinning and mass loss of an ice shelf due to excess basal melting (e.g., Paolo et al., 2015; Adusumilli et al., 2020) can also reduce its ability to buttress grounded ice, and drives loss of grounded ice (Pritchard et al., 2012; Smith, Fricker, Gardner, Medley, et al., 2020) effectively instantaneously (Gudmundsson et al., 2019). However, this buttressing capacity is not distributed equally across all floating ice. Fürst et al. (2016) identified areas of "passive shelf ice" near ice-shelf fronts that can be lost without significant impact to grounded ice, whereas Reese et al. (2018) found that thinning in some critical ice-shelf areas can cause the acceleration of upstream ice that is nearly 1,000 km away.

Grounded-ice mass loss due to ice-shelf thinning has been especially pronounced in the sectors of WAIS abutting the Amundsen and Bellingshausen seas (Figure 1.1), where ice shelves have little passive ice. In the Amundsen Sea, this trend has been attributed to increasing sub-shelf inflows of Circumpolar Deep Water (CDW) and modified CDW (mCDW), which, at 0.5–1.5°C, are ∼3–4°C warmer than the local freezing point, through glacial troughs on the continental shelf (e.g., Jenkins et al., 2010; Nakayama et al., 2019). This process ("mode-2" melting) is one of three major modes of ice-shelf basal melting, driven by the mostly thermohaline circulation of water masses in the ice-shelf cavity, identified by Jacobs et al. (1992) (Figure 1.2). "Mode-1" melting involves the intrusion of dense High-Salinity Shelf Water (HSSW), which forms near the surface from brine rejection during sea ice formation, along the seafloor toward the deep grounding line. The depression of the freezing temperature of seawater with depth (Fujino et al., 1974) allows the relatively warm HSSW to melt ice at the grounding line, generating plumes of meltwater that travel seaward along the ice-shelf base and potentially refreeze as marine ice. "Mode-3" melting occurs in the upper ice-shelf cavity, within about 100 km of the ice front and at the front face itself, due to the intrusion of seasonally warmed Antarctic Surface Water (AASW).

Ice-shelf thinning due to mode-2 melting may drive additional mass loss by facilitating

fracturing and ice-front retreat via frequent small iceberg calving events (Liu et al., 2015). This type of calving contrasts with the dominant calving mode on larger, more stable ice shelves: the shedding of tabular icebergs, typically from passive-ice regions (Fürst et al., 2016), every few decades (e.g., Greene et al., 2022). Across Antarctica, icebergs with surface areas >100 km^2 currently account for 89% of the total calved volume; those with surface areas between 0.1 and 10 km^2 and 10 and 100 km^2 account for 3–4% and 7–8%, respectively (Tournadre et al., 2016).

1.1.3 Study area: Ross Ice Shelf

Ross Ice Shelf (RIS; Figure 1.1) is the largest ice shelf in the world by area (∼480,000 km^2) and, in volume, is second only to Filchner-Ronne Ice Shelf (FRIS). Located in the southern portion of the Ross Embayment, RIS is fed by ice from both WAIS and the East Antarctic Ice Sheet (EAIS), with WAIS ice flowing across the grounding line via six broad ice streams and EAIS ice via outlet glaciers that cut through the Transantarctic Mountains (Tinto et al., 2019, their figures 1 and 2). Together, the two catchments (one from WAIS and one from EAIS) that RIS buttresses contain 11.6 m of sea-level equivalent (Tinto et al., 2019; Figure 1.1). Most of the ice shelf is between 200 and 500 m thick, but it is >500 m thick closer to the grounding lines of major ice streams and outlet glaciers and thins to <100 m near Ross Island and seaward of Roosevelt Island (Fretwell et al., 2013; Das et al., 2020). The WAIS side of RIS is generally thicker than the EAIS side (Tinto et al., 2019). Ice typically takes 1,000–2,000 years to travel from the RIS grounding line to the ice front (Tinto et al., 2019, their Supplementary Figure 2c).

Although RIS is currently near equilibrium (Rignot et al., 2013; Depoorter et al., 2013; Moholdt et al., 2014), the geologic record contains evidence of complex and often abrupt grounding-line change in the Ross Sea since the Last Glacial Maximum (e.g., Anderson et al., 2014; Yokoyama et al., 2016; Spector et al., 2017; Kingslake et al., 2018). Between 2003 and 2008, RIS gained 129 ± 6 Gt a^{-1} via flow of grounded ice across the grounding line and 65 ± 8 Gt a^{-1} via surface mass balance, and it lost 146 ± 9 Gt a^{-1} via iceberg calving and 48 ± 24 Gt

a^{-1} via basal melting (Rignot et al., 2013). The WAIS and EAIS sides of RIS exhibited distinct mass-loss patterns during this time period, with calving dominating the mass loss on the WAIS side and the two processes contributing roughly equally to mass loss on the EAIS side. Calving of large tabular icebergs every few decades due to rift propagation (e.g., Lazzara et al., 2008) accounts for most of the calving flux (and mass loss) on RIS. The ice shelf calved seven such icebergs in the early 2000s (Greene et al., 2022), including the 2,700 km^3 B-15 in March 2000 (Martin et al., 2007).

Like FRIS and Amery Ice Shelf (the third-largest ice shelf in Antarctica; Figure 1.1), RIS is a "cold-cavity" ice shelf, meaning it sits atop relatively cold sub-ice-shelf waters. Most basal melting on these three ice shelves occurs via mode-1 and mode-3 melting (Adusumilli et al., 2020). On RIS, mode-1 melting is driven by HSSW that is formed in the western Ross Sea, enters the ice-shelf cavity near Ross Island, and travels southward along the Transantarctic Mountains while melting ice at the grounding lines of EAIS outlet glaciers (Tinto et al., 2019). RIS experiences less basal refreezing ($\leq$2 cm a^{-1}; Zotikov et al., 1980; Holland et al., 2003) than FRIS and Amery (e.g., Adusumilli et al., 2020; Fricker et al., 2001). Horgan et al. (2011) attributed this to its shallow draft at the grounding line (typically 400–800 m, with a maximum of $\sim$1,400 m; Fretwell et al., 2013) relative to that of FRIS and Amery (up to $\sim$1,800 m and $\sim$2,300 m, respectively), which results in less thermal forcing and basal melting near the grounding line. Using ocean circulation modeling, Holland et al. (2003) showed that the thin water column in the southern and eastern parts of the cavity stalls inflowing HSSW, restricting heat transport to the deep grounding line, melting, and downstream refreezing. Tinto et al. (2019) also found that limited water column thickness on the WAIS side of the cavity forces the HSSW to turn northward and exit the cavity near the middle of the RIS front.

Mode-3 melting along the RIS front is responsible for as much as half of the total basal melt on the ice shelf (Horgan et al., 2011; Moholdt et al., 2014). Horgan et al. (2011) used repeat-track satellite laser altimetry from NASA's Ice, Cloud, and land Elevation Satellite (ICESat)

to show that melt rates increase exponentially toward the front, peaking at an average of 2.8 $\pm$ 1.0 m a^{-1} within the outermost kilometer. Recent studies employing radar observations of basal melting (Stewart et al., 2019; Tinto et al., 2019; Das et al., 2020) and satellite radar altimetry (Adusumilli et al., 2020) produced comparable melt-rate estimates and highlighted a specific intrusion of seasonally warmed AASW and subsequent higher melting below the thin ice east of Ross Island. This is a particularly important structural region of RIS, as it buttresses not only EAIS outlet glaciers but also some WAIS ice streams $\sim$1000 km away (Reese et al., 2018; Klein et al., 2020).

Cold-cavity and relatively stable ice shelves like RIS generally experience less mode-2 melting than their warm-cavity counterparts. Hydrographic and chlorofluorocarbon measurements in the Ross Sea (Smethie and Jacobs, 2005) and ocean circulation modeling (Tinto et al., 2019) showed that the outer portion of RIS experiences some mode-2 melting between 170°W and 180° ($\sim$–220 km to 0 km easting in the WGS84 Antarctic Polar Stereographic projection) due to local mCDW inflow. However, RIS has largely been protected from the CDW and mCDW incursions that have driven recent thinning of smaller ice shelves, owing to CDW mixing with surface waters in the Ross Sea, particularly where HSSW forms, and subsequent heat loss (Dinniman et al., 2011). Climate-driven changes in both near-front mode-2 melting and mode-3 melting will be a principal factor in near-term changes in RIS mass balance (Tinto et al., 2019). Studying an ice-shelf system like RIS that is in balance provides an opportunity to examine the mass-loss processes that act in all systems, without the distraction of the system being out of balance.

1.2 Scientific goals and questions of the dissertation

The goal of this dissertation is to shed light on understudied mass-balance processes, or understudied indicators of known mass-balance processes, on RIS. To achieve this goal, I rely on satellite and airborne remote sensing data, primarily satellite laser altimetry data from the second

iteration of the ICESat mission (ICESat-2; 2018–present). In the context of this dissertation, altimetry provides estimates of surface heights based on the two-way travel time of laser or radar pulses between a satellite or an aircraft and the Earth's surface. Laser altimetry is especially useful for measuring ice-sheet surface height because laser light penetrates minimally into the snowpack and produces reliable measurements over steep topography (Smith, Fricker, Gardner, Medley, et al., 2020). Over the past several decades, the dense spatial coverage and fairly high temporal resolution afforded by satellite altimeters have revolutionized our ability to monitor and interpret interannual changes in the floating and grounded portions of the Antarctic Ice Sheet (e.g., Adusumilli et al., 2020; Smith, Fricker, Gardner, Medley, et al., 2020). Airborne geophysical (or "aerogeophysical") campaigns like NASA's Operation IceBridge (MacGregor et al., 2021) have complemented these efforts by continuing the elevation record between satellite missions, acquiring additional high-resolution geophysical data sets over areas of interest, and offering opportunities to calibrate and validate satellite elevation data. Studies using satellite altimetry and airborne geophysics have provided the climate modeling community with observations of the current state and dynamics of the ice sheet that will be critical for testing ice-sheet tipping points (Armstrong McKay et al., 2022) and hypothesized mechanisms like MICI.

I will demonstrate that high-resolution satellite and aerogeophysical data can also resolve subtler ocean-driven changes in ice-shelf structure and topography. Specifically, I will focus on three ice–ocean interactions on RIS: marine-ice accretion associated with mode-1 melting; mode-3 melting; and buoyancy-driven flexure associated with ice-front melting at the waterline. These processes take place at key interfaces in the Antarctic system and may play a role in the stability of RIS and the Antarctic Ice Sheet more broadly as the climate warms. To assess the impacts of future changes in these processes on both RIS and other ice shelves, it is important to develop a baseline understanding of how they function on ice shelves in relative balance and incorporate this information into coupled models.

Toward the goal of understanding ocean-driven mass-loss processes on RIS, I structured

my PhD research around four sets of questions:

1. Can we confirm the presence and spatial distribution of basal marine ice on RIS?
2. Does the near-front shape of the RIS base reflect spatial variability in mode-3 melting?
3. Does the RIS front bend in response to the melting-driven development of a buoyant submerged bench? If so, where and by how much?
4. How has buoyancy-driven flexure along the RIS front changed in the early 21st century? How might RIS frontal topography change in the future?

1.3 Outline of the dissertation

The remainder of this dissertation is organized into four chapters. The three chapters that comprise the body of the dissertation (**chapters 2–4**) roughly correspond to, and are designed to (begin to) address, one or more of the sets of questions listed in subsection 1.2. Although all three chapters concern mass-balance processes on RIS and employ ICESat-2 data, they were developed as independent projects and so share some content.

Chapter 2 (questions 1 and 2 and part of Question 3) describes efforts to map and estimate the thickness of basal marine ice on RIS using radio-echo sounding data from the NSF-funded Ross Ocean and ice Shelf Environment, and Tectonic setting Through Aerogeophysical surveys and modeling (ROSETTA-Ice) aerogeophysical survey (2015–2017) and an ICESat-2 digital elevation model. This chapter also includes ROSETTA-Ice observations of near-front melting and of buoyancy-driven flexure at the RIS front that occurs in response to melting at the waterline.

Chapter 3 (Question 3) concentrates on the surface deformation associated with this buoyancy-driven flexure (referred to as a "rampart-moat structure" or "R-M structure"), as imaged by ICESat-2. It introduces an algorithm to detect and quantify the deformation in ICESat-2 profiles across the RIS front from October 2018 to July 2020 and discusses possible environmental drivers

of observed variability along the front. This chapter was published in *Geophysical Research Letters* in 2021.

Chapter 4 (questions 3 and 4) extends the spatial analysis of the R-M structures on the RIS front presented in **Chapter 3** to October 2022. It also incorporates R-M characteristics derived from ICESat. This extended record enables the analysis of temporal variability in buoyancy-driven flexure and the contextualization of the process in the larger RIS system. This chapter is currently in preparation for publication.

Chapter 5 summarizes the contributions and implications of the dissertation research, reiterates the value of the remote sensing data and methods used, and outlines several potential areas of future work.

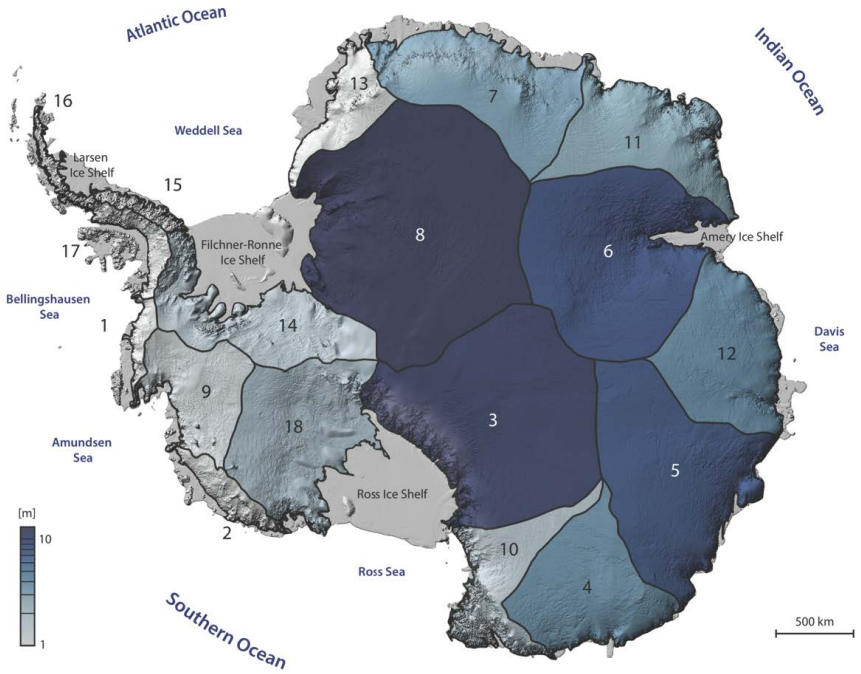

1) 0.1 m	7) 3.1 m	13) 0.7 m	Ross (basins 3 + 18): 11.6 m
2) 0.3 m	8) 12.0 m	14) 1.6 m	Filchner-Ronne (basins 8 + 14): 13.6 m
3) 9.6 m	9) 1.3 m	15) <0.1 m	Amery (basin 6): 7.7 m
4) 3.5 m	10) 1.6 m	16) <0.1 m	
5) 7.0 m	11) 2.7 m	17) 0.2 m	WAIS (basins 1, 2, 9, 14, 18): 5.6 m
6) 7.7 m	12) 3.7 m	18) 2.0 m	Total: 57.2 m

Figure 1.1: Reproduction of Supplementary Figure 1 from Tinto et al. (2019), which shows the estimated sea-level equivalent (SLE) of ice in each of the 18 Antarctic catchments identified by Rignot et al. (2011a). The table at the bottom also gives the total SLE values for the catchments buttressed by Ross, Filchner-Ronne, and Amery ice shelves (shown, along with other ice shelves, in gray); the entirety of the West Antarctic Ice Sheet (WAIS); and the entirety of the Antarctic Ice Sheet.

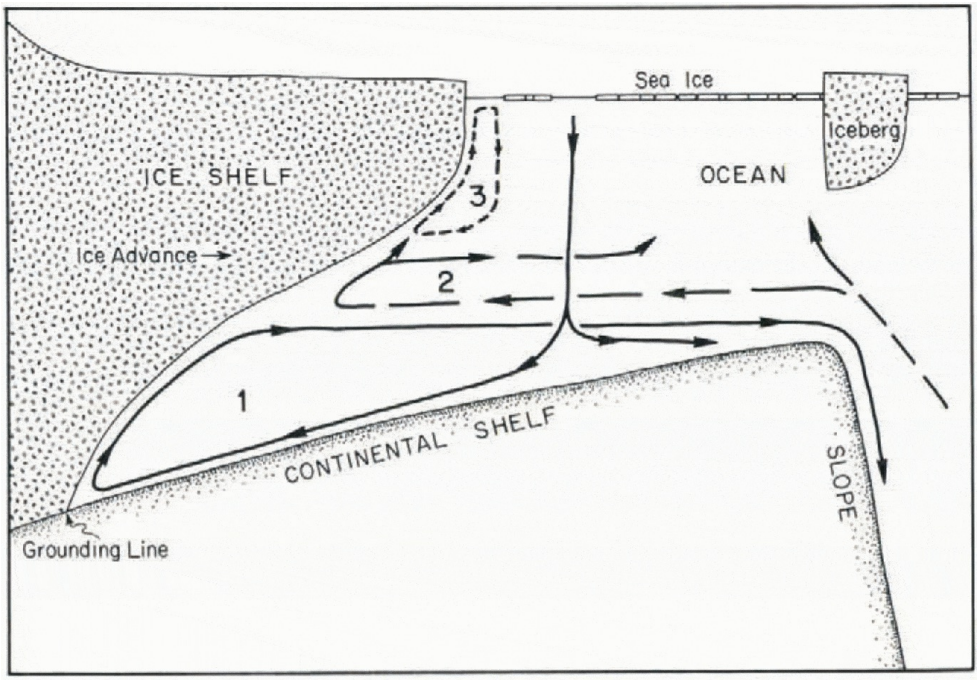

Figure 1.2: Reproduction of Figure 1 from Jacobs et al. (1992), which shows a schematic depiction of the three modes of ice-shelf basal melting. Mode-2 melting has been implicated in much of the thinning observed on West Antarctic ice shelves (e.g., Adusumilli et al., 2020). The dominant modes on Ross Ice Shelf are mode 1, whereby dense High-Salinity Shelf Water formed during sea ice production melts ice at the deep grounding line, and mode 3, whereby seasonally warmed surface waters melt the front face and the outer ice-shelf base.

Chapter 2

Insights into ice–ocean interactions on Antarctica's largest ice shelf from the ROSETTA-Ice airborne survey

2.1 Abstract

Ross Ice Shelf (RIS) is Antarctica's largest ice shelf by area, and it buttresses grounded ice from both East and West Antarctica with 11.6 m of combined sea-level potential. It is currently near steady state, in contrast to many ice shelves in West Antarctica that have thinned due to ocean melting. However, the sea-level potential and relative stability of RIS make it an ideal site on which to develop a benchmark understanding of ice-shelf mass balance processes against which to measure future changes. Here, we used ice-penetrating radar and lidar data from the ROSETTA-Ice aerogeophysical (airborne) survey (2015–2017), augmented with data from NASA's ICESat-2 satellite laser altimetry mission (2018–present) and simple ice-shelf modeling, to investigate several processes by which the ocean changes the mass of RIS. The difference between ice thicknesses derived from ICESat-2 and airborne radar suggests that melting at the deep grounding

line leads to the downstream accretion of basal marine ice in its interior southwest of Crary Ice Rise; however, our confidence in this estimate is limited by the measurement uncertainties, which are similar in magnitude to the signal. Farther north, ROSETTA-Ice radar thickness data confirm that RIS thins—often exponentially—as it approaches the front. We interpret this topography on the outer tens of kilometers of the ice shelf as a signature of basal melting and compare its spatial variability to established patterns of near-front melting. We also present observations of, and efforts to model, near-front surface deformation that arises from ice-shelf flexure due to a buoyant, submerged bench of ice, which forms in response to waterline erosion. Previous work has identified this flexure on icebergs and implicated it in small-scale, edge-parallel calving, so it may be indicative of an overlooked mass-loss process on RIS.

2.2 Introduction

The major terms of the mass balance of the Antarctic Ice Sheet are net snow accumulation (mass gain), discharge into the Southern Ocean via its floating ice shelves (mass loss), and meltwater runoff (mass loss) (Shepherd et al., 2018). For each basin of the ice sheet (Figure 1.1), the difference between mass gain and mass loss determines its mass balance. Antarctica's ice shelves control the rate of ice discharge by imparting back stresses due to contact with sidewalls and bathymetric highs, a process commonly referred to as "buttressing" (e.g., Thomas, 1979). Ross Ice Shelf (RIS; Figure 2.1), the continent's largest ice shelf by area, buttresses grounded ice that would contribute 11.6 m to global sea level—9.6 m from East Antarctica and 2.0 m from West Antarctica (Tinto et al., 2019; Figure 1.1)—if it melted completely. Reduction of an ice shelf's mass weakens its buttressing ability, increasing ice flux across the grounding line (Gudmundsson et al., 2019), which contributes to sea-level rise.

Basal melting accounts for just over half of Antarctic ice-shelf mass loss on multidecadal timescales, with the remainder occurring via iceberg calving (Rignot et al., 2013; Depoorter et al.,

2013; Greene et al., 2022). However, this partitioning varies between individual drainage systems. In the Amundsen and Bellingshausen seas, basal melting dominates, and increased melting has shifted these systems out of balance and led to thinning of ice shelves (e.g., Paolo et al., 2015) and a threefold increase in mass loss from West Antarctica between the periods 1992–1997 and 2012–2017 (Shepherd et al., 2018). In contrast, RIS and the other two large ice shelves, Filchner-Ronne (FRIS) and Amery, lose most of their mass through calving. However, their mean melt rates are low compared to those of ice shelves in the Amundsen and Bellingshausen seas, and their mass losses are balanced by mass gains elsewhere (Section 2.3).

Balanced systems such as RIS, FRIS, and Amery provide an opportunity to study the same mass-balance processes that act in other systems and establish a baseline against which to monitor future changes. In this study, we present airborne observations collected during the November–December 2015, 2016, and 2017 field seasons of the Ross Ocean and ice Shelf Environment, and Tectonic setting Through Aerogeophysical surveys and modeling (ROSETTA-Ice) project (Tinto et al., 2019) that resolve or otherwise inform our understanding of processes related to distinct modes of basal melting on RIS.

This chapter begins with background information on melting and freezing in the cavities of cold-water ice shelves (Section 2.3) and a description of the airborne and satellite data sets we used (Section 2.4). Sections 2.5 and 2.6 are motivated by three research questions:

1. Can we confirm the presence and spatial distribution of basal marine ice on RIS?
2. Does the near-front shape of the RIS base reflect spatial variability in mode-3 melting?
3. Does the RIS front bend in response to the melting-driven development of a buoyant submerged bench?

To address the first research question, we used ROSETTA-Ice radio-echo sounding (RES) data, in combination with data from NASA's Ice, Cloud, and land Elevation Satellite-2 (ICESat-2) mission, to investigate the presence of marine ice on the base of RIS (Section 2.5). To address the

second research question, we used the ROSETTA-Ice RES data, as well as data from the project's second, higher-frequency radar system, to explore the variability of basal topography along the RIS front and compare these observations with known patterns of "mode-3" melting (subsection 2.6.1). To address the third research question, we introduce radar- and lidar-based evidence for buoyancy-driven flexure at the RIS front, which we suspect is caused by ocean melting at the waterline. We describe efforts to model this flexure with a one-dimensional elastic-beam model (subsection 2.6.2).

2.3 Basal melting and freezing under cold-water ice shelves

Jacobs et al. (1992) identified three modes of ice-shelf basal melting driven by ocean circulation in and near sub-ice-shelf cavities (Figure 1.2). "Mode-1" melting occurs when cold and dense High-Salinity Shelf Water (HSSW), which is a by-product of sea-ice formation on the continental shelf, melts ice at the deep grounding lines due to the depression of the *in situ* freezing point with depth. This produces buoyant plumes of Ice Shelf Water (ISW), which is colder than the surface freezing point for its salinity. These plumes can become supercooled as they ascend along the ice-shelf base, leading to the development of buoyant frazil crystals. Accretion of these crystals to the base forms a layer of relatively dense (at a reference density of 920 kg m^{-3}; Craven et al., 2009) marine ice characterized by a platelet crystal structure and pockets or channels of brine that develop from seawater trapped during the supercooling process (e.g., Zotikov et al., 1980; Craven et al., 2009). In this way, mode-1 melting can create an "ice pump" (e.g., Robin, 1979; Lewis and Perkin, 1986) that redistributes ice from an ice shelf's deeper grounding line to its shallower interior. "Mode-2" melting, the prevailing melt mechanism on "warm-water" ice shelves that are currently experiencing thinning, is caused by inflows of warm Circumpolar Deep Water (CDW) or modified CDW (mCDW) at intermediate depths. Finally, "mode-3" melting occurs below the relatively shallow outer portions of ice shelves and on the front face itself due to

the intrusion of seasonally warmed Antarctic Surface Water (AASW).

Most of the basal melting on RIS, FRIS, and Amery (the major "cold-water" ice shelves) occurs via modes 1 and 2 (Adusumilli et al., 2020). Basal marine ice can be an important structural element of cold-water Antarctic ice shelves, as it can arrest or heal rifts and change the viscosity profile and stress response of the ice column (e.g., Holland et al., 2009; Kulessa et al., 2014). On FRIS and Amery, the basal marine-ice layer is sufficiently thick to be detected with existing satellite altimetry and airborne and ground-based geophysical data sets. For certain areas of FRIS, marine-ice thickness can exceed 350 m (Joughin and Vaughan, 2004; Lambrecht et al., 2007), and basal freeze-on rates approach 5 m a^{-1} near locations of observed marine-ice accretion (Joughin and Padman, 2003). The Amery marine-ice layer, which is thickest in two bands in the along-flow direction, has a maximum thickness of 190–200 m (Fricker et al., 2001; Craven et al., 2009). The marine-ice layer on RIS is at least an order of magnitude thinner, owing to its relatively shallow grounding line (Horgan et al., 2011), weak ice pump, and uniform draft (Moholdt et al., 2014). Neal (1979) used the received power from RES data to delineate two along-flow zones of RIS with at least 10 m of basal marine ice. Farther east, at Camp J9 (Figure 2.2), a 1978 borehole drilled during the Ross Ice Shelf Project revealed a $\sim$6 m debris-free marine-ice layer and a local freeze-on rate of 2 cm a^{-1} (Zotikov et al., 1980). In 2017, a second borehole (HWD2; Figure 2.2) 335 km northwest of J9 only showed evidence of ephemeral accretion (Stevens et al., 2020).

Melting of the outermost 100 km (i.e., mode-3 melting) accounts for up to 50% of the basal melt on RIS (Moholdt et al., 2014), with melt rates increasing exponentially closer to the front (Horgan et al., 2011). In contrast to mode-1 melting, this process generally melts ice that does not contribute significantly to buttressing (Fürst et al., 2016), but a notable exception to this is AASW-driven melting below the area east of Ross Island (Figure 2.1; Stewart et al., 2019; Tinto et al., 2019; Das et al., 2020), which can "tele-buttress" grounded ice >900 km away (Reese et al., 2018). Despite the large role of AASW inflow in basal melting on RIS, the mechanism by which this water mass enters the cavity remains subject to debate (e.g., Malyarenko et al., 2019).

2.4 Airborne and satellite data over RIS

2.4.1 ROSETTA-Ice aerogeophysical survey (2015–2017)

The objective of the ROSETTA-Ice project (Tinto et al., 2019) was to combine airborne (or air-enabled) glaciological, geological, and oceanographic observations to elucidate the history and dynamics of the RIS system. This project was the second to systematically survey RIS; the first was the ground-based Ross Ice Shelf Geophysical and Glaciological Survey (RIGGS; 1973–1978), which measured various glaciological characteristics and water column thickness at stations spaced by ∼55 km (Bentley, 1990). The primary component of ROSETTA-Ice was an aerogeophysical survey using the IcePod ice-imaging system and multiple gravimeters, all of which were installed on New York Air National Guard LC-130 aircraft based at McMurdo Station on Ross Island (Figure 2.1). The ROSETTA-Ice survey grid was designed to sample as many of the RIGGS station locations as possible and included 94 east–west lateral survey lines (denoted hereafter with an "L" before the line number) spaced by 10 km and 15 north–south tie lines (denoted hereafter with a "T" or the words "tie line" before the line number) spaced by 55 km (Figure 2.1). The total flight distance was 61,000 km. We used data from three instruments housed within the IcePod: the two ice-penetrating radar systems, which provided information about the internal structure and thickness of RIS (Das et al., 2020), and the scanning laser altimeter, which used the two-way travel time of emitted laser pulses to map the RIS surface (Boghosian et al., 2019).

Ice-penetrating radar

The ROSETTA-Ice shallow-ice radar (SIR), which has a center frequency of 2 GHz and a bandwidth of 600 MHz, imaged the internal stratigraphy of the upper 300–400 m of RIS at a depth resolution of 0.25 m. In contrast, the deep-ice radar (DICE) onboard the IcePod has a center frequency of 188 MHz and a bandwidth of 60 MHz; these specifications were intended

to enable penetration to the base of the ice shelf at a depth resolution of $<$2 m. The recorded two-way travel times were converted to depths using the speed of electromagnetic waves in solid ice, 1.68 x 108 m s^{-1}, with no correction for increased speed in firn (Das et al., 2020). For each radar and survey line, the ROSETTA-Ice project produced georeferenced radargram images and measurements of the depth of an internal reflector (SIR only) and/or the ice-shelf base (SIR and DICE). Here, we used the radargram images and ice-shelf thickness estimates from both radars.

Laser altimetry

The lidar instrument onboard the IcePod, a RIEGL VQ-580 airborne laser scanner, provided snapshots of RIS surface elevation along the ROSETTA-Ice survey lines. From an average flight elevation of 750 m above ground level, the near-infrared (1064 nm; Briese et al., 2012) laser illuminated $\sim$15 cm footprints on the ice-shelf surface, with minimal penetration into the snowpack (e.g., Deems et al., 2013). Given this average flight elevation, an average flight speed of 180 knots, and a laser pulse repetition rate of 150 kHz, the ROSETTA-Ice lidar typically provided elevation measurements at a density of 1.2 points m^{-2} along parallel scan lines. In clear conditions, the scanning swath was 0.75–1.5 km wide.

The raw lidar range measurements were combined with trajectory and attitude data from a Global Navigation Satellite System inertial navigation system using the RIEGL RiPROCESS software to yield georeferenced point clouds (with heights reported relative to the WGS84 ellipsoid) for the full swath. For each flight, the ROSETTA-Ice project also produced a narrow-swath point cloud, generated using a 10° angle filter, and a nadir surface (with elevations relative to the WGS84 ellipsoid), generated from the narrow-swath point cloud and partly edited for clouds. In our analysis, we examined the nadir surface for three tie-line ROSETTA-Ice lidar profiles across the RIS front.

2.4.2 ICESat-2 satellite laser altimetry (2018–present)

Launched in September 2018, ICESat-2 carries a single instrument, the Advanced Topographic Laser Altimeter System (ATLAS) (Markus et al., 2017). During nominal operations, ATLAS acquires a full cycle of elevation measurements along each of its 1,387 reference ground tracks (RGTs) every 91 days. It is a photon-counting laser that transmits pulses of green (532 nm) light and then detects, time tags, and geolocates individual photons reflected by the Earth's surface. Each outgoing pulse is split into three beam pairs separated by ∼3.3 km on the ground. Within each pair, the beams are separated by ∼90 m, and one has about four times as much energy as the other ("strong" vs. "weak"). This configuration and ATLAS's 10 kHz pulse repetition frequency mean that, for each RGT, ATLAS acquires elevation data for ∼10.6–12 m footprints (Magruder et al., 2020) spaced by ∼0.7 m on the surface along six distinct ground tracks. The 92° inclination of ICESat-2's orbit provides coverage between 88°S and 88°N. Thus, ICESat-2 data are particularly favorable for investigations of ice-shelf processes on RIS, which extends as far south as ∼85.3°S, or ∼–438 km northing in the WGS84 Antarctic Polar Stereographic projection (Figure 2.1), where the ICESat-2 tracks are closely spaced.

We used the RIS subset of Version 2 of the ICESat-2 L3B Gridded Antarctic and Arctic Land Ice Height product (ATL14; Smith et al., 2022), which provides a 100 m gridded digital elevation model (DEM) of Antarctic Ice Sheet surface height. The ICESat-2 Science Project Office at NASA's Goddard Space Flight Center generated this DEM by fitting surface-height estimates to high-quality data from Version 5 of the L3B Slope-Corrected Land Ice Height Time Series product (ATL11) using an algorithm based on regularized least squares. The DEM consists of repeat-track data from cycles 3 to 14 (March 29, 2019, to March 23, 2022) but is referenced to January 1, 2020.

2.5 Toward an improved map of basal marine ice on RIS

In this section, we address the first research question: (1) Can we confirm the presence and spatial distribution of basal marine ice on RIS?

2.5.1 Methods

To determine the presence of marine ice on the base of RIS, we followed the Fricker et al. (2001) method of differencing thicknesses derived from altimetry using buoyancy and thicknesses measured directly via airborne RES. This method relies on the assumption that airborne RES cannot measure the thickness of the full ice column when it includes basal marine ice. While it can typically discern the boundary between meteoric and marine ice, which is marked by a relatively weak reflection coefficient and a jump in conductivity (Blindow, 1994), attenuation by the saline marine ice limits the ability of the radar signal to penetrate to the marine-ice–ocean boundary. Thus, where there is marine ice (due to local freezing, advection of upstream marine ice, or a combination of both), thicknesses inverted from altimetry measurements should be greater than coincident thicknesses from RES; the difference should yield the approximate thickness of the marine ice. In our analysis, we applied this method using surface elevations from the ICESat-2 ATL14 DEM and thicknesses from ROSETTA-Ice DICE RES data.

Data preparation

The ATL14 data have already been corrected for the effects of ocean, load, solid Earth, and pole tides using the pyTMD software (Sutterley et al., 2017), with the ocean tide correction values computed from the CATS2008 circum-Antarctic ocean tide model (Howard et al. (2019), an update to the model described by Padman et al. (2002)), and for height changes due to atmospheric forcings with the MOG2D dynamic atmosphere correction (DAC) values inherited from lower-level ICESat-2 products. For each DICE measurement location on floating ice, as

determined using the Depoorter et al. (2013) RIS mask, we assigned a mean ATL14 elevation value by calculating the block mean of all ATL14 elevations for floating ice within a 500 m radius.

ATL14 elevations are relative to the WGS84 ellipsoid, whereas the conversion to thickness through the buoyancy equation requires heights relative to the instantaneous sea surface (h_{ss}). We transformed the block-mean elevation values to h_{ss} values using the 2.5-arc-minute EGM2008 geoid model (Pavlis et al., 2012) and by applying a uniform correction (–1.4 m) for mean dynamic topography (MDT), which gives the difference between the mean sea surface and the geoid. We note that Griggs and Bamber (2011) chose not to correct for MDT when converting surface elevation data from satellite radar altimetry over RIS, FRIS, and Amery to thicknesses, citing the absence of MDT estimates for ice-shelf cavities, distinct sub-shelf circulation patterns beneath, and errors associated with extrapolating values from the open ocean. However, they did correct for MDT for smaller ice shelves, using mean values at their fronts that range from –2.0 to –1.1 m. Our MDT value of –1.4 m is consistent with the values in the vicinity of the RIS front in the DTU13MDT (Andersen et al., 2015).

Hydrostatic calculation

For all ATL14-derived h_{ss} values, we calculated thickness H using a variation of the hydrostatic equation:

$$H = \frac{\rho_w}{\rho_w - \rho_i}(h_{ss} - H_a), \tag{2.1}$$

where ρ_w and ρ_i are the column-averaged densities of seawater (1028 $\pm$ 1 kg m^{-3}) and ice (917 $\pm$ 5 kg m^{-3}), respectively, and H_a is the firn air content (FAC), or the thickness change that would result from the removal of all air in the firn column. We accounted for the RIS firn column using the average FAC for the ATL14 time period from Version 1.2.1 (Release 2) of the NASA Goddard Space Flight Center Firn Densification Model (GSFC-FDMv1.2.1, with simulations run from 1980 to 2022; Medley et al., 2022a; Medley et al., 2022b) (Figure 2.2). We also used a rearranged version of Equation (2.1) with ROSETTA-era FAC values to convert the DICE thicknesses to

h_{ss} values. Following Fricker et al. (2001), we computed the hydrostatic height anomaly, or the difference between the ATL14 and DICE h_{ss} values (Figure 2.3). The absolute value of this quantity should be large over parts of the ice shelf where there are inaccuracies in thickness and/or column-averaged ice density (e.g., areas where marine ice could be present or the modeled FAC correction is wrong). The derived difference between the ICESat-2 and DICE thicknesses (Figure 2.4) may be interpreted as the thickness of a potential layer of basal marine ice, assuming all other error sources are small.

Uncertainty estimation

We estimated the uncertainties (95% confidence intervals) in the thickness anomaly by combining the uncertainties associated with each term in the three component calculations: the conversion of ATL14 surface elevations to h_{ss}; Equation (2.1); and the differencing of the two thickness maps. We incorporated the uncertainty in the DICE thicknesses in the uncertainty analysis for the third calculation. For the first calculation, we obtained the 1σ uncertainties for the ATL14 elevations from the ATL14 product and assumed conservative uncertainties of 0.5 m for both the EGM2008 geoid heights (Gilardoni et al., 2016) and MDT (Griesel et al., 2012). We assumed that these uncertainties were uncorrelated and added them in quadrature. We propagated the resulting uncertainties to h_{ss} in Equation (2.1) and combined them with the uncertainties in ρ_w, ρ_i, and H_a. The GSFC-FDMv1.2.1 did not include gridded uncertainties in H_a, so we substituted them with 2σ uncertainties from the Institute for Marine and Atmospheric research Utrecht Firn Densification Model (with simulations run from 1979 to 2016; Ligtenberg et al., 2011). Finally, we assumed a single uncertainty value of $\sqrt{2}$ m for all DICE thicknesses; this is the crossover difference precision (2 m; Das et al., 2020) scaled by a factor of $1/\sqrt{2}$, to reflect that the calculation of crossover differences involved two independent measurements (Schröder et al., 2019). We added the uncertainties in the DICE and ATL14 thicknesses in quadrature to produce the final set of uncertainties at 95% confidence intervals, which range from $\sim$28 m to

$\sim$100 m (Figure 2.5a).

2.5.2 Results

The most striking signal on the hydrostatic height anomaly (Figure 2.3) and thickness-difference (Figure 2.4) maps is the area of positive height anomaly ($>$5 m) and thickness difference ($>$50 m) (i.e., blue areas) along the RIS front, especially near Nascent Iceberg (location in Figure 2.1). We do not suspect that this signal reflects the presence of marine ice, as the anomalies are spatially coincident with low ($<$10 m) FAC values simulated by GSFC-FDMv1.2.1 (Figure 2.2). Focusing on the thickness-difference analysis, Figure 2.4 shows several other areas that may indicate basal freeze-on, including between Roosevelt Island and Marie Byrd Land, in the vicinity of Siple Dome, and south of Minna Bluff (locations in Figure 2.1). We also report a band of positive thickness difference, where ATL14 values can be more than 50 m greater than DICE values, originating just southwest of Crary Ice Rise. Many of these values exceed the corresponding 95% confidence interval (Figure 2.5b). West of (i.e., to the right of) this band, there are several less prominent bands, roughly following ice flow originating in the Transantarctic Mountains, where the ATL14 thickness is greater than the DICE thickness.

Despite these areas of positive thickness difference, the ATL14 thicknesses are less than the DICE thicknesses for most of RIS, with a mean difference value of –14.2 m. The largest negative biases, many of which are beyond the 95% confidence interval, are along the Transantarctic Mountains and between Minna Bluff and Ross Island (possibly due to DICE acquisition issues along flight-line segments in these areas) and near large rifts towards the front of the ice shelf. The negative thickness differences near rifts can be explained by the fact that our analysis does not account for ice advection between the ROSETTA-Ice era and the ATL14 reference date (January 1, 2020), which can create the impression of large vertical offsets (both negative and positive, depending on the location of the ROSETTA-Ice flight line relative to the rift). Difference in coverage near rifts also plays a role. Whereas DICE can only resolve some

of the basal topography near rifts, perhaps due to the presence of mélange, ATL14 offers fairly dense elevation coverage in rifts, although the conversion to thickness does not always produce physically reasonable values. We also observe broad regions of negative hydrostatic height anomalies and thickness differences for ice flowing between Crary Ice Rise and Siple Dome. This area includes J9, where drilling revealed a $\sim$6 m marine-ice layer (Zotikov et al., 1980), but the thickness difference near J9 does not exceed the local uncertainty.

2.5.3 Discussion

Identification of areas with marine ice using basal return character and strength from DICE

Where our analysis shows a positive thickness difference, we can use the character and strength of the basal return within coincident DICE radargrams to help confirm the presence of marine ice. Neal (1979) argued that the melt/freeze-on dynamics at the ice-shelf base can affect the amount of dielectric loss, and thus the reflection coefficient and strength of the basal return. Basal melting promotes the downward advection of cold ice and thus the lowering of the average temperature of the ice column, which in turn leads to decreased dielectric loss (e.g., Carter et al., 2009) and a relatively strong basal reflection. The accretion of relatively warm marine ice, on the other hand, reduces this downward advection, increases the average ice-column temperature, and leads to increased attenuation and a relatively weak basal reflection. To this end, we inspected portions of five DICE radargrams (Figures 2.6–2.10) for evidence of weak or imperceptible basal returns near where the positive thickness differences originating southwest of Crary Ice Rise exceed the 95% confidence interval.

The strength of the basal reflector is lower in regions where we propose there is marine ice, and this is consistent across all five survey lines. All five of the radargrams feature kilometers-long sections where the base-picking algorithm could not detect the base (and thus do not appear in Figures 2.4 and 2.5b). In some cases (survey lines L410, L470, and T1090; Figures 2.7, 2.9,

and 2.10), these missing basal returns interrupt areas where the thickness difference is above the confidence interval. These patterns provide additional support for the attribution of the observed large thickness differences to the presence of basal marine ice. The two thickness estimates seem to agree best where returns are strongest (see, e.g., between –790 and –785 km northing in Figure 2.10), which, by the above logic, may be areas of melting. However, these interpretations of local freezing and melting patterns would be strengthened by a formal calculation of the power loss across the picked basal reflector.

There is support in the literature for our hypothesis that the band of positive thickness-difference values east of Crary Ice Rise is due to marine ice:

(i) The band is close to the zones of the ice shelf (a and b in Figure 2.11) where Neal (1979) had inferred the presence of a marine-ice layer with a minimum thickness of 10 m. He arrived at this thickness estimate by calculating the associated per-meter dielectric loss from the permittivity of saline ice and relating it to the reflection coefficient of the RIS–water interface. He observed that the reflection coefficient in these zones increased toward the front (see the outer ∼50–100 km of the ice shelf north of zone b in Figure 2.11), which he attributed to melting of the accreted basal marine ice. Similarly, our proposed marine-ice band does not persist all the way to the RIS front (Figure 2.5b).

(ii) The inferred marine-ice band is consistent with recent modeling results that demonstrated that the HSSW–ISW mixture largely remains on the EAIS side of the RIS cavity as it travels northward (Tinto et al., 2019). The HWD2 borehole, drilled through ice in the central RIS that originated from the southern Transantarctic Mountains, is on the southwestern edge or outside of our proposed marine-ice band; therefore, we do not consider its "ephemeral" ∼10 cm basal crystal layer (Stevens et al., 2020) necessarily inconsistent with our results.

(iii) The band corresponds to a location where Adusumilli et al. (2020) and Das et al. (2020) reported modest basal freezing rates ($<$1 m a^{-1}). Adusumilli et al. (2020) also found that

basal freezing on RIS occurs at drafts of 300–350 m; by this standard, the DICE and ATL14 data sets both show drafts conducive to freezing in our proposed marine-ice band.

(iv) The surface streaklines (Fahnestock et al., 2000; LeDoux et al., 2017) near the proposed band, which depict the paths of parcels of ice from Mercer or Whillans ice streams onto the ice shelf, match the local streamlines reasonably well. This suggests that the flow of ice across the grounding line has been relatively steady in recent decades to centuries, which may have contributed to the local accretion and downstream advection of basal marine ice.

We conclude that multiple lines of evidence point to the existence of a marine-ice band on RIS, but there are several outstanding issues related to our thickness-difference analysis.

Limitations and uncertainties

With the data and model outputs used here, it is difficult to identify a viable scientific explanation for the broad regions of negative hydrostatic height anomaly and thickness difference for ice flowing between Crary Ice Rise and Siple Dome, including near J9, and along the Transantarctic Mountains. Indeed, most of the RIS-wide hydrostatic height and thickness anomaly values are negative (insets in Figures 2.3 and 2.4), that is, the DICE heights and thicknesses are generally larger than those estimated from ATL14. While the thickness-difference value at J9 is within the range of the local uncertainty, many of the other negative values exceed the corresponding uncertainties, which also draws the validity of our proposed marine-ice band into question. We suspect that this negative bias is related to the GSFC-FDMv1.2.1 FAC values and our choice of column-averaged density (which are inherently linked). In their analysis, Griggs and Bamber (2011) also found that thicknesses derived from RES generally exceeded those derived from satellite radar altimetry near where the Bindschadler Ice Stream feeds into RIS. They proposed that this mismatch existed because they used a value for the column-averaged ice density that was too low (possibly due to the presence of a basal marine-ice layer, which

Craven et al., 2009, estimated has a density of 920 kg m^{-3}) in the altimetry thickness calculation. Moreover, our results may not capture the full extent of the negative bias, as the ROSETTA-Ice radar data were processed without allowing for increased velocities in firn, which could bias the DICE thicknesses low (Griggs and Bamber, 2011).

That the uncertainties associated with our thickness-difference calculation are comparable to, and often larger than, the differences themselves is consistent with the results of Moholdt et al. (2014). They reported a low signal-to-noise ratio in their assessment of basal melt and freeze-on rates derived from satellite laser altimetry for most of RIS. Most of the uncertainty in our method emerged during the conversion of ATL14 heights into thicknesses, reflecting the uncertainties associated with our simplistic treatment of ice density and in the FAC outputs. By contrast, the $\sim$30 m total uncertainty reported by Fricker et al. (2001), which is on the low end of the values of total uncertainty in our analysis, comes mostly from errors in the RES data.

Future work

Further improvements to our understanding of the distribution of basal marine ice on RIS will require reductions in uncertainties arising from several different factors. In particular, we need to reexamine our selected FAC correction to address the general mismatch between DICE- and ATL14-estimated thicknesses. This will involve both additional FAC modeling and validation using existing and new field measurements of vertical and horizontal variations in ice density. We also need to reprocess the DICE data to tailor them to this application. We propose two improvements. First, we should incorporate a correction into the range calculation for the increased speed of electromagnetic waves in firn; this would increase the accuracy of the thickness estimates. Second, we should use a different reflection power or brightness threshold to allow for more accurate calculation of the reflection coefficient and the power loss across the interface. This could reveal more relevant information about the ice–ocean (or meteoric-ice–marine-ice) interface, the character and material composition of the interface, and the ability of DICE to

penetrate any thickness of marine ice. Our argument that there is an area of active freeze-on on RIS would also be strengthened by a correlation with freezing-favorable thickness gradients, as Neal (1979) demonstrated for his zones a and b.

2.6 ROSETTA-Ice observations and modeling of RIS ice-front processes

In this section, we present indirect observations of mass-balance processes closer to the RIS front, specifically mode-3 melting on the outer ice-shelf base and targeted melting at the waterline. We address the second and third research questions: (2) Does the near-front shape of the RIS base reflect spatial variability in mode-3 melting? (3) Does the RIS front bend in response to the melting-driven development of a buoyant submerged bench?

2.6.1 Spatial variability in mode-3 melting from ROSETTA-Ice radar

Horgan et al. (2011) considered the relationship between roughly along-flow thickness changes, derived from repeat-track ICESat altimetry, and basal melting on the outer 60 km of RIS. (ICESat preceded ICESat-2 and was in operation between 2003 and 2009.) They found that surface elevations decreased exponentially, and inferred from this that basal melt rates also increased exponentially, toward the front; they attributed the spatial changes in surface elevation to basal melting. Horgan et al. (2011) reproduced the exponential increase in melt rates using a buoyant plume model, finding that steeper basal slopes cause the plume to accelerate, with the increased velocities increasing turbulent mixing and melting, in turn leading to even steeper basal slopes (a positive feedback).

We hypothesized that spatial differences in the topography of the RIS base, as imaged by the two ROSETTA-Ice radars (see example SIR radargram segment in inset in Figure 2.12a),

might provide further insights into the patterns of near-front melting identified by Horgan et al. (2011), Adusumilli et al. (2020), and other researchers. We examined nine DICE (Figure 2.12a) and 15 SIR (Figure 2.13a) thickness profiles that sampled the outer ∼60 km and front of RIS. Following Horgan et al. (2011), we divided the RIS front into five smaller regions, loosely based on tabular calving history, and sorted the profiles by the region of the front crossing. However, we also considered data from ROSETTA-Ice lines that crossed the front between Marie Byrd Land and Roosevelt Island (our Region 1; Figure 2.12a). To isolate the underlying topography of the base, we applied a ∼1 km Gaussian filter to each thickness profile and manually removed rifts and large-scale crevasses with thickness differences >∼15 m. Following Horgan et al. (2011), we fit exponential functions of the form $ae^{bx} - c$ (with the minus representing the fact that the thickness values decrease towards the front) to the outer 60 km and 10 km of the filtered and edited profiles. In some cases, we allowed the best-fitting exponential to extend farther back from the front than the thickness profile itself (see, e.g., the DICE thickness plots and associated exponentials for the two front crossings of L780 in Figure 2.12b). We assessed the fit of the exponentials to the thickness profiles using the reduced chi-squared ($\tilde{X}^2$) statistic, which is given by

$$\tilde{X}^2 = \frac{1}{\nu} \sum_i \frac{(O_i - E_i)^2}{\sigma_i^2}, \tag{2.2}$$

where ν is the number of degrees of freedom (here taken to be the number of observations minus the number of parameters in the model, or three), O_i the observations, E_i the expected (modeled) values, and σ_i the errors on the observations. As described in Section 2.5, we estimated that the DICE thicknesses have errors of $\sqrt{2}$ m; for simplicity, we used these errors for the SIR thicknesses as well. Generally, a $\tilde{X}^2$ value near 1 is considered indicative of a well-fitting model. A $\tilde{X}^2$ value above 1 suggests that the model does not describe the data well or the error variance is underestimated; a $\tilde{X}^2$ value below 1 suggests overfitting to accommodate noise or overestimated error.

Considered alone, the best-fitting exponentials for the 60 km thickness profiles from both radars confirm that the base slopes upward toward the front with varying degrees of exponential behavior (Figures 2.12b–2.12d and Table 2.1 for the DICE profiles and Figures 2.13b–2.13c and Table 2.2 for the SIR profiles). Indeed, some of the exponentials are near linear. However, the high $\tilde{X}^2$ values for all of the 60 km exponentials indicate a poor fit, with the two lowest (for the DICE profile with the two L780 front crossings) registering values of 3.60 and 2.48 (Table 2.1). The best-fitting exponentials for the outer 10 km of the thickness profiles exhibit steeper basal gradients and generally fit the observations better. For both radars, the exponential fit to the outer 10 km of the T1040 thickness profile (which crossed the front in Region 3) had the $\tilde{X}^2$ value closest to 1. Three of the DICE 10 km exponentials and four of the SIR 10 km exponentials have $\tilde{X}^2$ values below 1, which indicates overfitting. In any case, the wide range of $\tilde{X}^2$ values suggests that we should reconsider our smoothing technique and error assumptions, especially for SIR.

Despite its limitations, this preliminary analysis offers several broad takeaways related to the performance of the two radars and spatial melting patterns. First, for the four survey lines across the front where both DICE and SIR mapped the ice base, we report good agreement between the exponential fits for the two sets of radar profiles but some divergence in the $\tilde{X}^2$ values. Also, both radar data sets show that the near-front portion of RIS is thicker on the eastern side than on the western side, but we note that our analysis includes fewer profiles on the western side. Finally, considering only the exponentials for the outer 10 km, the thickness profiles with the highest values of the fitted rate parameter ($b \geq 38$) cross the front in regions 3, 5, and 6. (The first front crossing of L780 is an exception.) The $\tilde{X}^2$ values are typically low for those profiles whose best-fitting exponentials have these high b values (except for T1110), which implies that the exponentials describe the data relatively well. We propose that these profiles (L810, T1040, T1050, T1060, L860, L900, and T1120) developed in response to elevated mode-3 melting. The front crossings of L810, T1040, T1050, and T1060 are close to where a layer of modified Circumpolar Deep Water (mCDW) enters the RIS cavity (Smethie and Jacobs, 2005), driving

melting (especially) in summer of the outer 100 km of the ice shelf (Tinto et al., 2019). Das et al. (2020) identified basal melting "hotspots" near where L860 and L900 cross the RIS front. L860 samples the front in Region 4 (Nascent Iceberg), where Horgan et al. (2011) recorded shallower melt rate gradients, possibly due to prolonged exposure to melting from lack of calving, than the rest of the front. Finally, T1120 crosses the front ∼30 km east of Ross Island, which is a known entry point of AASW and site of basal melting exceeding 2 m a^{-1} (Stewart et al., 2019; Tinto et al., 2019; Das et al., 2020; Adusumilli et al., 2020).

2.6.2 Ice-front shape from ROSETTA-Ice radar and lidar and elastic-beam modeling

Motivated by observations of near-front deviations in buoyancy that we found in the ROSETTA-Ice radargrams, we combined ROSETTA-Ice SIR and laser altimetry data with elastic-beam modeling to consider a potential mechanism for the development of these features.

ROSETTA-Ice shallow-ice radar

ROSETTA-Ice SIR radargrams showed a recurring ice-surface feature within ∼1 km of the ice front. This feature is characterized by a raised edge and an inboard surface depression, with a height difference on the order of a few meters, that is morphologically similar to the uplifted rift flank topography previously documented on RIS (Fricker et al., 2005; Walker and Gardner, 2019) and on the edges of icebergs (e.g., Scambos et al., 2005). It represents a deviation from the expected "roll-off" in surface elevation towards the front documented by Horgan et al. (2011), which they attributed to the mode-3 melting discussed in subsection 2.6.1. In Figure 2.14, we present three examples of this feature, as resolved by the SIR, from survey lines T1000, T1090, and T1110. As these tie lines are oriented roughly parallel to the local direction of ice flow and normal to the local front, we can compare the features without having to reproject the

along-flight-line coordinates. The existence of this feature in radargrams that show relatively smooth upstream topography (e.g., those for T1090 and T1110; Figures 2.14c–2.14d) suggests that the feature is formed, or at least modified, locally near the front. In the radargram for T1000, the subsurface layers in the firn column exhibit deformation that mirrors that of the surface (see inset in Figure 2.14b). The basal topography in all three radargrams does not show evidence of thickening coincident with the surface feature. Thus, from the SIR data alone, we interpret the feature as a deviation from local hydrostatic equilibrium and hypothesize that it results from stresses that deform the outer edge of the ice shelf.

ROSETTA-Ice laser altimetry

To investigate the surface feature identified in the radargrams, we inspected the near-front portions of the coincident ROSETTA-Ice lidar nadir profiles for survey lines T1000, T1090, and T1110. As for the ATL14 elevations used in Section 2.5, we referenced the lidar nadir ellipsoidal elevations to the EGM2008 geoid model. We then converted the heights relative to the geoid to heights relative to the instantaneous sea surface by correcting for ocean tides using values from CATS2008, for ocean load tides using values from the TPXO7.2 tide model (Egbert and Erofeeva, 2002), for DAC using values from MOG2D (produced by CLS using the model from LEGOS and distributed by AVISO+, with support from CNES), and for MDT using a uniform value of –1.4 m. The lidar nadir profiles (Figure 2.15) confirm and provide a higher-resolution view of the near-front surface deformation that we observed in the radargrams. In all three cases, the depression is $\sim$0.3–0.5 km upstream of the raised edge. The smallest of the three features, that along T1090, spans $\sim$4 m from the bottom of the depression to the top of the raised edge (Figure 2.15b); this relative height difference is $\sim$7.5 m for the largest of the three features, that along T1110 (Figure 2.15c).

Horgan et al. (2011) noted an "elastic plate-bending phenomenon that occurs within a few ice thicknesses ($<$1 km) of the front" in their ICESat-based analysis of surface elevations and

basal melting near the RIS front. This refers to ice-shelf flexure in response to the presence of a buoyant submerged bench of ice. The bench itself develops when wavecut formation and growth, driven by thermal and physical erosion at the waterline, causes the collapse of the overhanging ice. Such flexure has been observed and described as producing "rampart-moat" profiles on iceberg margins (e.g., Scambos et al., 2005; Wagner et al., 2014), with "moats" 2–5 m lower than and several ice thicknesses inboard of "ramparts" (Scambos et al., 2005). Scambos et al. (2005) and Wagner et al. (2014) also hypothesized that bench growth and progressive flexure could eventually result in a small calving event along a basal crevasse. Buoyancy-driven flexure has been theorized to occur (Reeh, 1968) or indirectly observed (Hughes, 2002) on ice shelves. As the surface features in the lidar nadir profiles are qualitatively and dimensionally similar to the rampart-moat profiles, we conclude that they formed due to buoyancy-driven flexure, and we hereafter refer to them as rampart-moat or R-M structures.

Elastic-beam modeling

The ROSETTA-Ice lidar profiles can be compared with models of ice-shelf flexure and calving in response to a buoyant bench of a certain length. Recent studies determined that viscous behavior should dominate in ice-sheet bending processes with timescales longer than 1–2 months, and elastic behavior should dominate in processes with shorter timescales (i.e., days to weeks) (Sayag and Worster, 2013; Wagner et al., 2016; Mosbeux et al., 2023). Efforts to model buoyancy-driven flexure have considered it as both a viscous and an elastic process. For example, Scambos et al. (2005) used a finite element model that included Glen's flow law and a mean temperature of –12°C to simulate R-M structures observed on icebergs that calved from Ronne Ice Shelf, and Wagner et al. (2014, 2016) developed one-dimensional analytical elastic-beam models to describe buoyant flexure on iceberg and glacier margins, respectively. Mosbeux et al. (2020) developed two-dimensional elastic and viscous frameworks to model the ice-shelf response to a submerged bench (including calving); they noted that the phenomenon likely reflects

the viscoelastic behavior of ice. For the sake of simplicity, we compared the three lidar-resolved R-M structures in Figure 2.15 with the surface deformation predicted by a modified version of the one-dimensional analytical elastic-beam model applied by Wagner et al. (2014, 2016) and Mosbeux et al. (2020). We did not reproject the tie-line profiles because they were close to normal to the front.

Following Wagner et al. (2014, 2016) and Mosbeux et al. (2020), we considered the ice shelf as an elastic beam that is pinned (grounded) on one end and freely floating on the other end. With the additional loading of a submerged bench $Q(x)$, the floating-beam equation is

$$B\frac{\partial^4 w(x)}{\partial x^4} = -\rho_i g H + \rho_w g \left[\frac{H}{2} - w(x)\right] + Q(x), \tag{2.3}$$

where $B \equiv EH^3/12(1-\nu^2)$ is the bending stiffness of the ice-shelf beam, with E representing the Young's modulus of ice, H the thickness of the ice-shelf beam, and ν the value of Poisson's ratio for ice; $w(x)$ is the vertical deflection of the ice-shelf beam from its hydrostatic floating depth; ρ_i is again the column-averaged ice-shelf-beam density; g is the acceleration due to gravity; and ρ_w is again the density of seawater. In this setup, x is the horizontal distance along the ice-shelf beam, valued at 0 at the front and increasing with distance upstream. We take $Q(x)$ as a point force that acts at the edge of the ice-shelf beam (i.e., at x = 0) and is equal to $F\delta(x)$. Here, $F = F_{buoyancy} - F_{gravity} = l_{bench} g \rho_i d$, where l_{bench} is the length of the bench and $d \equiv H(\rho_w - \rho_i)/\rho_w$ is the freeboard of the ice-shelf beam in isostatic equilibrium, and $\delta(x)$ is the Dirac delta function. The solution to Equation (2.3) is

$$w_{Q(x)}(x) = \sqrt{2} H_s l_{bench} \exp(-\frac{x}{\sqrt{2} l_w}) \cos(-\frac{x}{\sqrt{2} l_w}), \tag{2.4}$$

where $H_s \equiv H\rho_i(\rho_w - \rho_i)/(\rho_w^2 l_w)$ is a scaled, dimensionless thickness of the ice-shelf beam and $l_w \equiv (B/g\rho_w)^{1/4}$ is the "buoyancy length," which results from the balance between the beam stiffness and the hydrostatic pressure loading.

Wagner et al. (2016) and Mosbeux et al. (2020) demonstrated that, when a bench is present, the shape of a given section of an ice-shelf front results from a combination of two bending moments: (1) the bench-driven upward bending moment; and (2) the downward bending moment resulting from the fact that the horizontal pressures from the ice and water are only balanced below the waterline, leaving the pressure from the ice-shelf freeboard unbalanced. We accounted for both effects by modeling the total vertical deflection as the sum of the deflections caused by each bending moment. We computed the pressure-gradient effect on the surface profile using a version of Equation (2.3) with an additional term on the right-hand side that accounts for the in-plane stress induced by the freeboard pressure imbalance (Reeh, 1968; Sergienko, 2010; Wagner et al., 2016). We refer the reader to Section 2 of Wagner et al. (2016) for a more detailed description of this formulation and solution.

For each of the three lidar nadir profiles, we estimated near-front H using the coincident SIR radargrams (Figures 2.14b–2.14d) and combined this estimate with near-surface density and firn depth values from van den Broeke (2008) to obtain ρ_i. We took the value of ν to be 0.3 and the value of ρ_w to be 1028 kg m^{-3}. We then tuned the values of E and l_{bench} to maximize the visual fit between each lidar nadir profile and the corresponding modeled surface profile. We report the best fit when we allow for values of E ranging from 5 to 50 MPa and values of l_{bench} ranging from 18 to 52 m (Figure 2.16). These values are comparable in magnitude to those modeled by Scambos et al. (2005), Wagner et al. (2014, 2016), and Mosbeux et al. (2020). Our results indicate that the choice of ρ_i, which is complicated by uncertainties in near-front firn properties, has a large effect on the shape of each modeled profile, and especially on the relative height (i.e., height difference between the rampart and the moat) of each R-M structure. The shaded regions around the modeled profiles in Figure 2.16 demonstrate that a lower value of ρ_i increases the relative buoyancy of the submerged bench and thus the R-M height; the opposite is true for a higher value of ρ_i. Our "optimal" values of ρ_i, which are crude estimates unconstrained by in situ density profiles, are significantly lower than that typically assigned to solid ice, 917 kg m^{-3}, but

they reflect our attempt to allow for the presence and spatial variability of the surface firn layer. We acknowledge that this attempt is complicated by our estimation of near-front H from the SIR radargrams for use in the calculation of ρ_i when the SIR data do not include a firn correction.

The values of E invoked here are two to three orders of magnitude smaller than the $\sim$1 GPa typically assigned to ice experiencing tidal deformation (Vaughan, 1995). The low values of E could also reflect the presence of crevasses that weaken the ice-shelf beam and lower its effective thickness h_{eff}. This, in turn, has a large effect on the effective bending stiffness $B_{eff} \equiv EH_{eff}^3/12(1-\nu^2)$ without requiring a large change in (or value of) E (Mosbeux et al., 2020). Brine infiltration (Cook et al., 2018) may have also contributed to increased ice fluidity and a lower effective E near the portions of the RIS front sampled by survey lines T1000, T1090, and T1110. However, Mosbeux et al. (2020) argued that this process is insufficient to explain the full difference between modeled and generally accepted values of E. In any case, the fact that such low values of Young's modulus are required to match the observed profiles suggests that R-M development is not a purely elastic process and also incorporates the viscoplastic behavior of ice (Mosbeux et al., 2020). It is important to move towards more accurate descriptions of near-front rheology because modeling the process as purely elastic has been shown to produce larger and more frequent calving events than a purely viscous model (Mosbeux et al., 2020).

2.7 Summary and outlook

We used RES and lidar data from the 2015–2017 ROSETTA-Ice aerogeophysical survey to explore mass-balance processes occurring on the base and at the front of RIS. Thicknesses derived from an ICESat-2 DEM exceed those measured by the ROSETTA-Ice deep-ice radar in a flow-parallel band beginning southwest of Crary Ice Rise. The radargrams show weak basal returns in these areas of positive thickness difference. We interpret this reduced return strength as evidence of the presence of basal marine ice, which leads to a different dielectric

contrast than that at a meteoric-ice–ocean boundary. However, our confidence in the overall thickness-difference map, including the thickness of our potential marine-ice layer, is limited by the high uncertainties associated with our method. These uncertainties are largely driven by inaccuracies in and assumptions about the ice-shelf density profile (i.e., the density of solid ice and the correction for FAC); they may also be too low because the radar thicknesses did not include a correction for the increased speed of electromagnetic waves in firn (and we did not include the error associated with this change in speed in our uncertainty analysis).

We used the ROSETTA-Ice RES data to investigate the basal topography of the outer 10s of km of RIS. For the outer 10 km, some of the steepest basal gradients occur near known entry points (and melting sites) of mCDW and AASW. Finally, coincident ROSETTA-Ice shallow-ice radar and lidar observations reveal deviations from hydrostatic equilibrium $<$1 km from the RIS front, which we attribute to flexure associated with a buoyant bench of ice protruding from the front face. We reproduced the deflection with an elastic-beam model but had to invoke Young's moduli that are several orders of magnitude less than published values for pure ice. As is the case for the marine-ice analysis, this exercise would benefit from additional constraints on RIS firn properties and density profiles.

We have demonstrated that R-M structures can be resolved in the ROSETTA-Ice lidar nadir surface profiles, which provide elevation measurements every $\sim$100 m along the flight track. In Chapters 3 and 4, we extend the study of R-M structures using satellite laser altimetry, taking advantage of the knowledge that ROSETTA-Ice has provided through the coincident acquisition of radar observations of ice thickness and surface elevations.

Future work might seek to determine whether bench development leads to the calving of small icebergs and, if yes, to identify where such calving occurs on the RIS front and quantify the resultant mass loss. The relationship between R-M development and mode-3 melting is also of interest. The results of Mosbeux et al. (2020) and our elastic-beam modeling indicate that ice-shelf thickness, which we have shown varies spatially with exposure to mode-3 melting,

is a critical factor in the bending stiffness and deflection of the front. Warm surface waters appear to be responsible for both bench formation and mode-3 melting, but the latter requires an additional mechanism that facilitates the entry of these warm waters into the cavity. This mechanism, whether driven by tides or eddies (e.g., Arzeno et al., 2014; Li et al., 2017) or local frontal ablation (Malyarenko et al., 2019), may also affect or be affected by bench development.

2.8 Data availability and acknowledgments

Nearly all of the ROSETTA-Ice data are available at https://pgg.ldeo.columbia.edu/data/rosetta-ice; the SIR-derived ice-shelf-base picks can be requested from the ROSETTA-Ice team. Version 2 ATL14 data are available via the portal at https://nsidc.org/data/atl14/versions/2. The GSFC-FDMv1.2.1 model outputs can be accessed via Zenodo: https://doi.org/10.5281/zenodo.7221954. We also acknowledge the use of imagery from the NASA Worldview application (https://worldview.earthdata.nasa.gov), which is part of the NASA Earth Observing System Data and Information System, and elevation data from the Reference Elevation Model of Antarctica (http://data.pgc.umn.edu/elev/dem/setsm/REMA/mosaic/). The Depoorter et al. (2013) mask is available at https://doi.pangaea.de/10.1594/PANGAEA.819150. The gridded MOG2D DAC values applied to the lidar nadir elevations can be accessed at https://www.aviso.altimetry.fr/.

We are grateful to the ROSETTA-Ice field team, the 109th Airlift Wing of the New York Air National Guard, the United States Antarctic Program, and the McMurdo Station staff during the 2015–2017 ROSETTA-Ice field seasons. We thank Caitlin D. Locke, Chris Bertinato, and Tejendra Dhakal for their efforts in processing the ROSETTA-Ice lidar and radar data; Brooke Medley for sharing earlier iterations of GSFC-FDM during the development of this project; and Matthew R. Siegfried for helpful discussions and insights. This bulk of this work was carried out as part of the National Science Foundation project ROSETTA-Ice (grants 1443498, 1443677, 0958658, and 1443534), with additional support from the Gordon and Betty Moore Foundation.

Chapter 2 is coauthored with Fricker, H. A., Padman, L., Cordero, S. I., Das., I., Tinto, K. J., Bell, R. E., Mosbeux, C., & Wagner, T. J. W. The dissertation author was the primary investigator and author of this material.

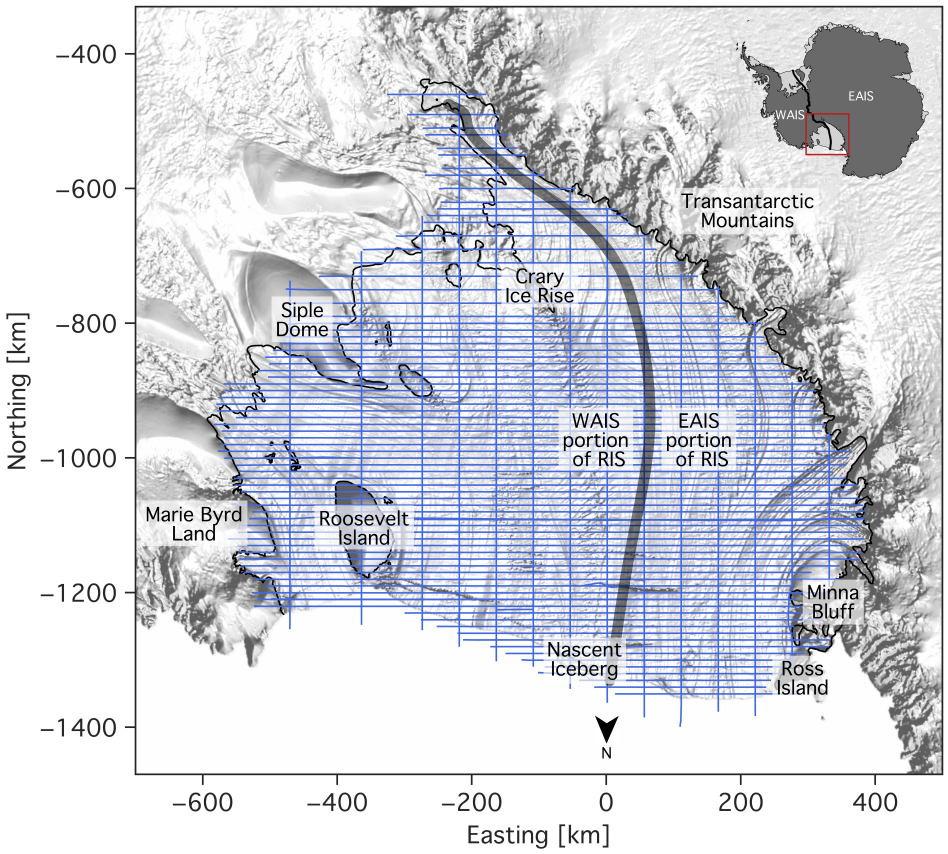

Figure 2.1: ROSETTA-Ice survey lines (blue) over Ross Ice Shelf (RIS) during the 2015–2017 field seasons, overlaid on a hill-shaded version of the Reference Elevation Model of Antarctica (REMA) mosaic (Howat et al., 2019). Labels show key features and geographic places mentioned in the text. The thin black line indicates the Depoorter et al. (2013) RIS mask and the thick gray line the streamline marking the approximate boundary between shelf ice from the West and East Antarctic ice sheets (WAIS and EAIS, respectively). The projection is Antarctic Polar Stereographic with a standard latitude of 71°S and a standard longitude of 0°. Inset map (created using Antarctic Mapping Tools data; Greene et al., 2017) features the Mouginot et al. (2017) WAIS–EAIS boundary in black.

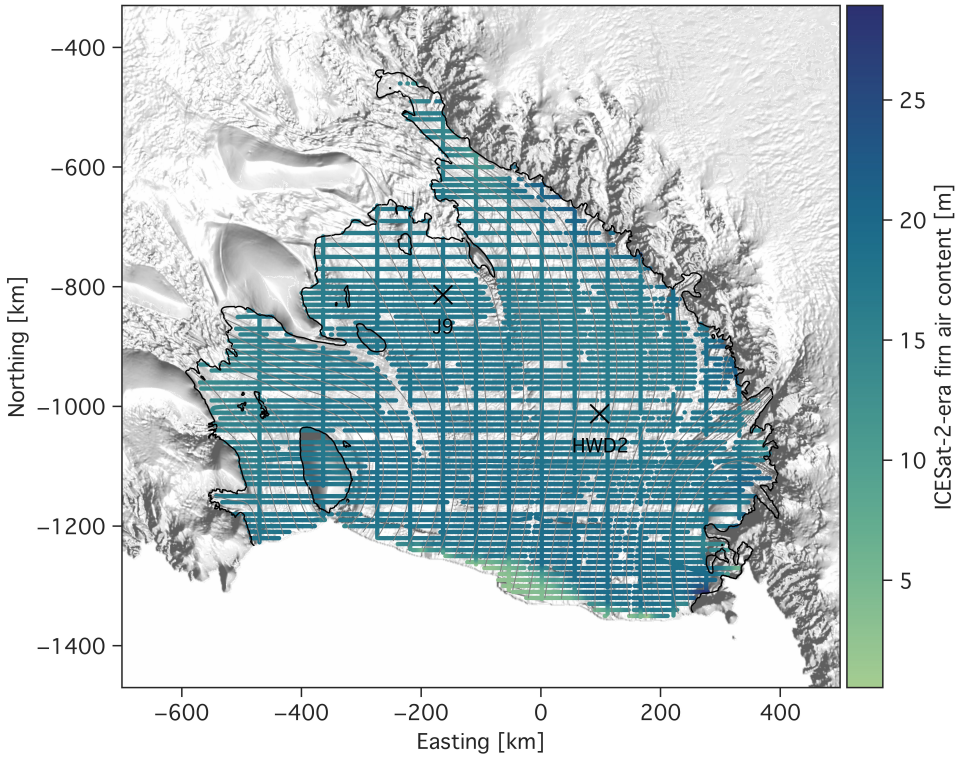

Figure 2.2: Average firn air content from GSFC-FDMv1.2.1 (Medley et al., 2022a; Medley et al., 2022b) for March 2019–March 2022, when data incorporated into the ICESat-2 ATL14 digital elevation model were collected, overlaid on the hill-shaded version of the REMA mosaic. The thin black line indicates the Depoorter et al. (2013) RIS mask, the black crosses the locations of the J9 and HWD2 boreholes, and the gray lines streamlines derived from Rignot et al. (2017) velocity fields. The projection is Antarctic Polar Stereographic with a standard latitude of 71°S and a standard longitude of 0°.

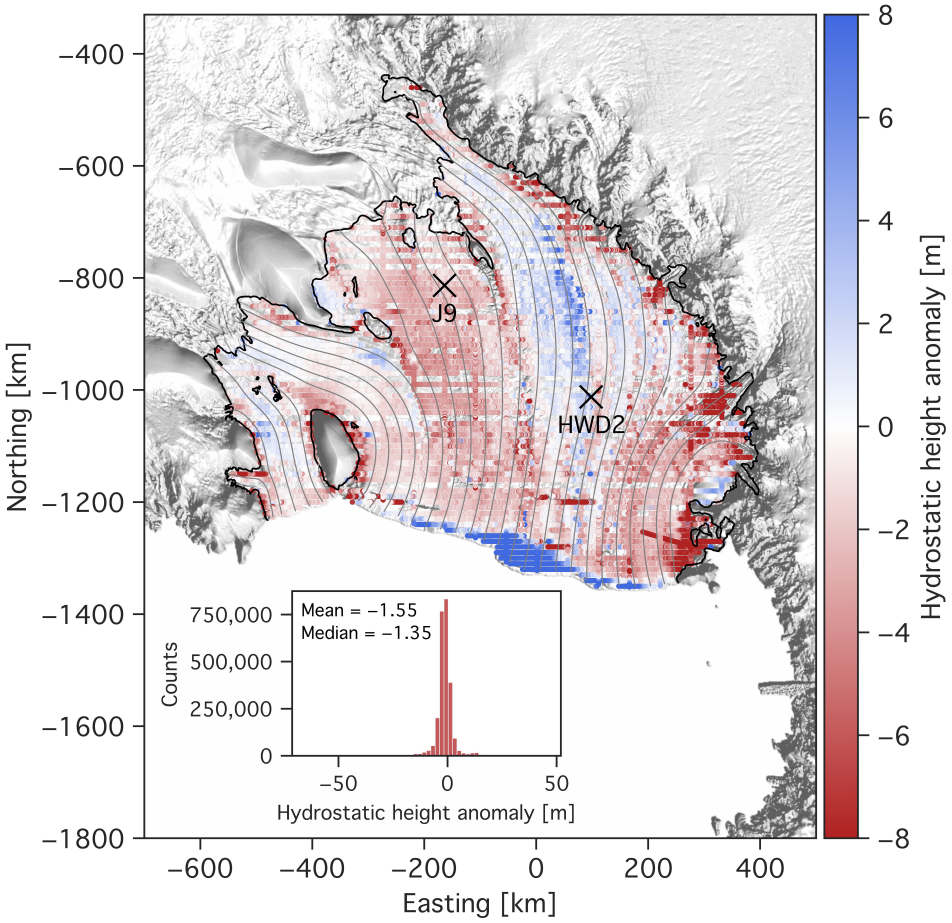

Figure 2.3: Hydrostatic height anomaly, or the difference between ATL14- and ROSETTA-Ice DICE-derived height, overlaid on the hill-shaded version of the REMA mosaic. Negative anomaly values are in red and positive anomaly values are in blue. Thin black line, black crosses, gray lines, and projection information are as in Figure 2.2. Inset shows the histogram of hydrostatic height anomaly values.

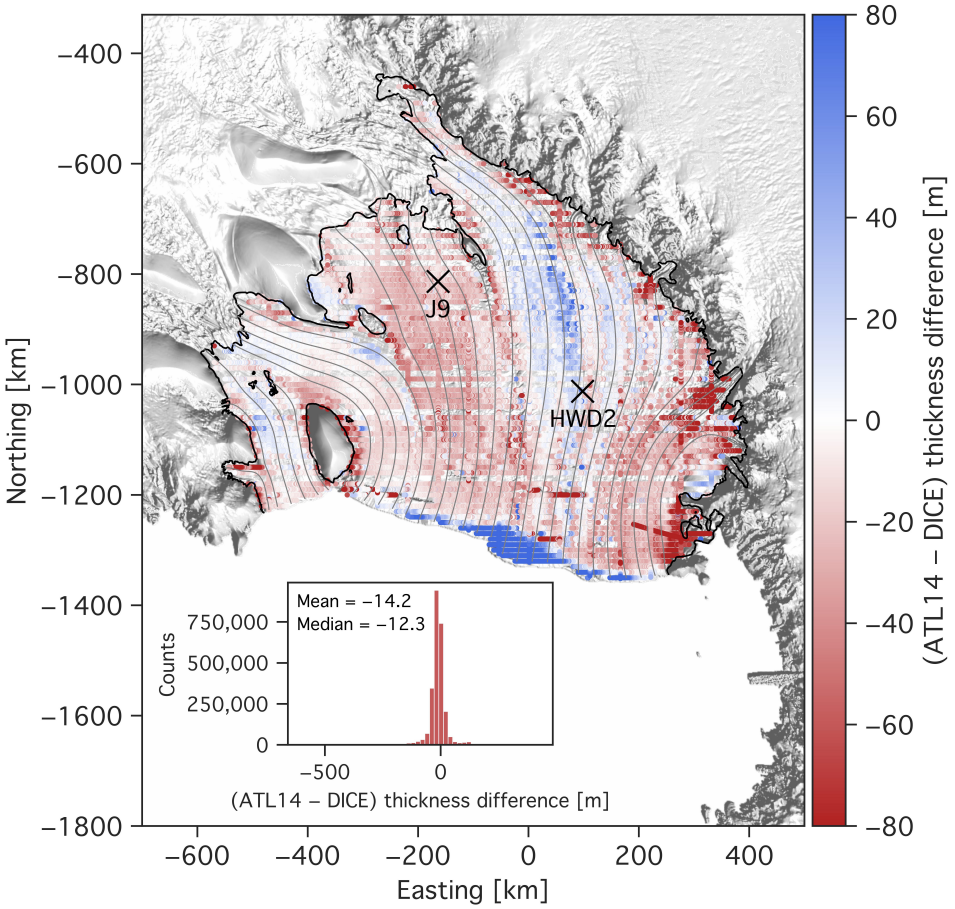

Figure 2.4: Difference between ATL14- and DICE-derived thickness, overlaid on the hill-shaded version of the REMA mosaic. Negative thickness differences are in red and positive thickness differences (i.e., potential locations where there is basal marine ice) are in blue. Thin black line, black crosses, gray lines, and projection information are as in Figure 2.2. Inset shows the histogram of thickness-difference values.

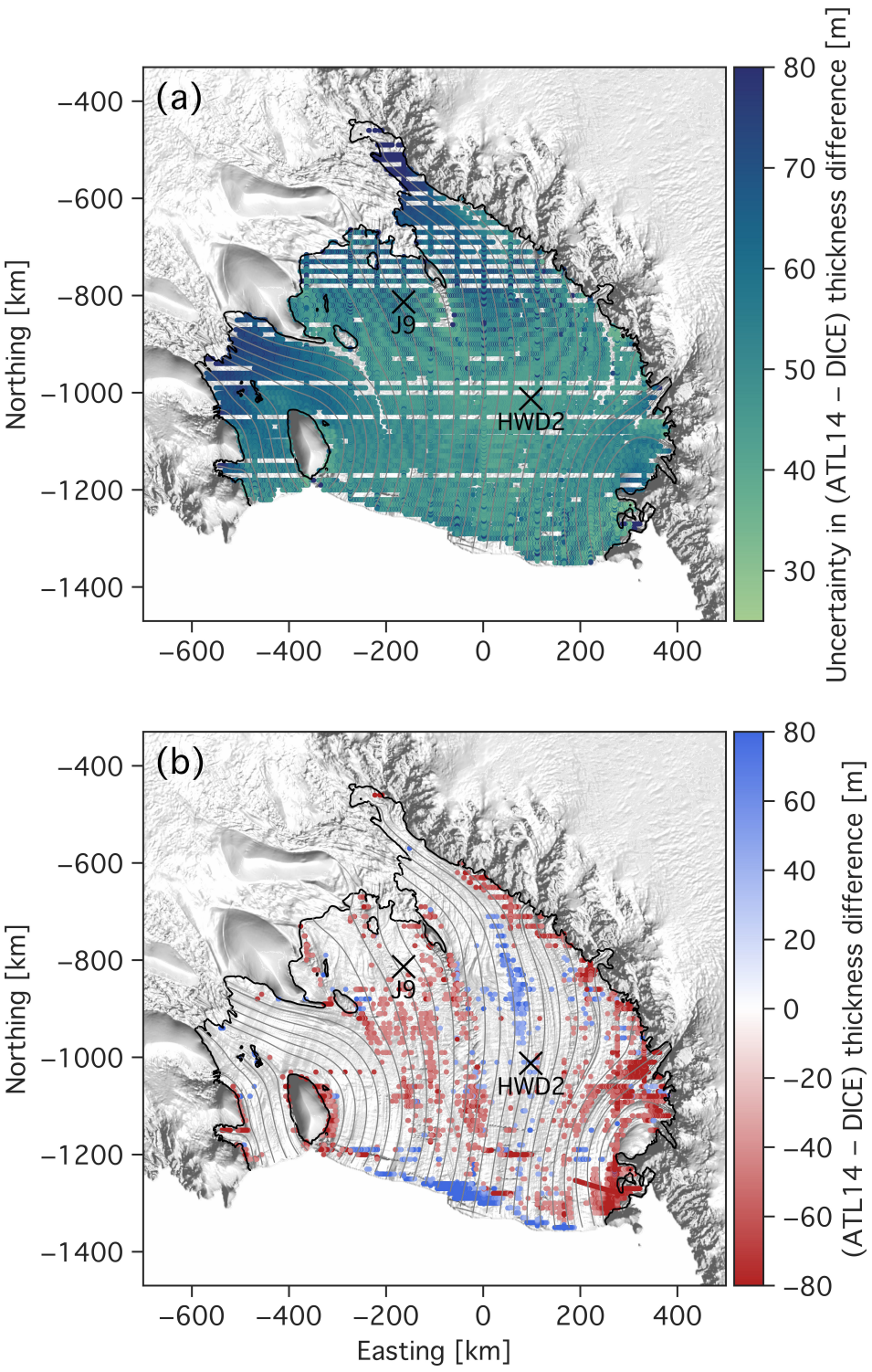

Figure 2.5: (a) Uncertainty (95% confidence intervals) in the difference between ATL14- and DICE-derived thickness and (b) thickness-difference values that exceed the corresponding uncertainties, each overlaid on the hill-shaded version of the REMA mosaic. In both panels, the thin black line, black crosses, gray lines, and projection information are as in Figure 2.2. In (b), the red–blue coloring is as in Figure 2.4.

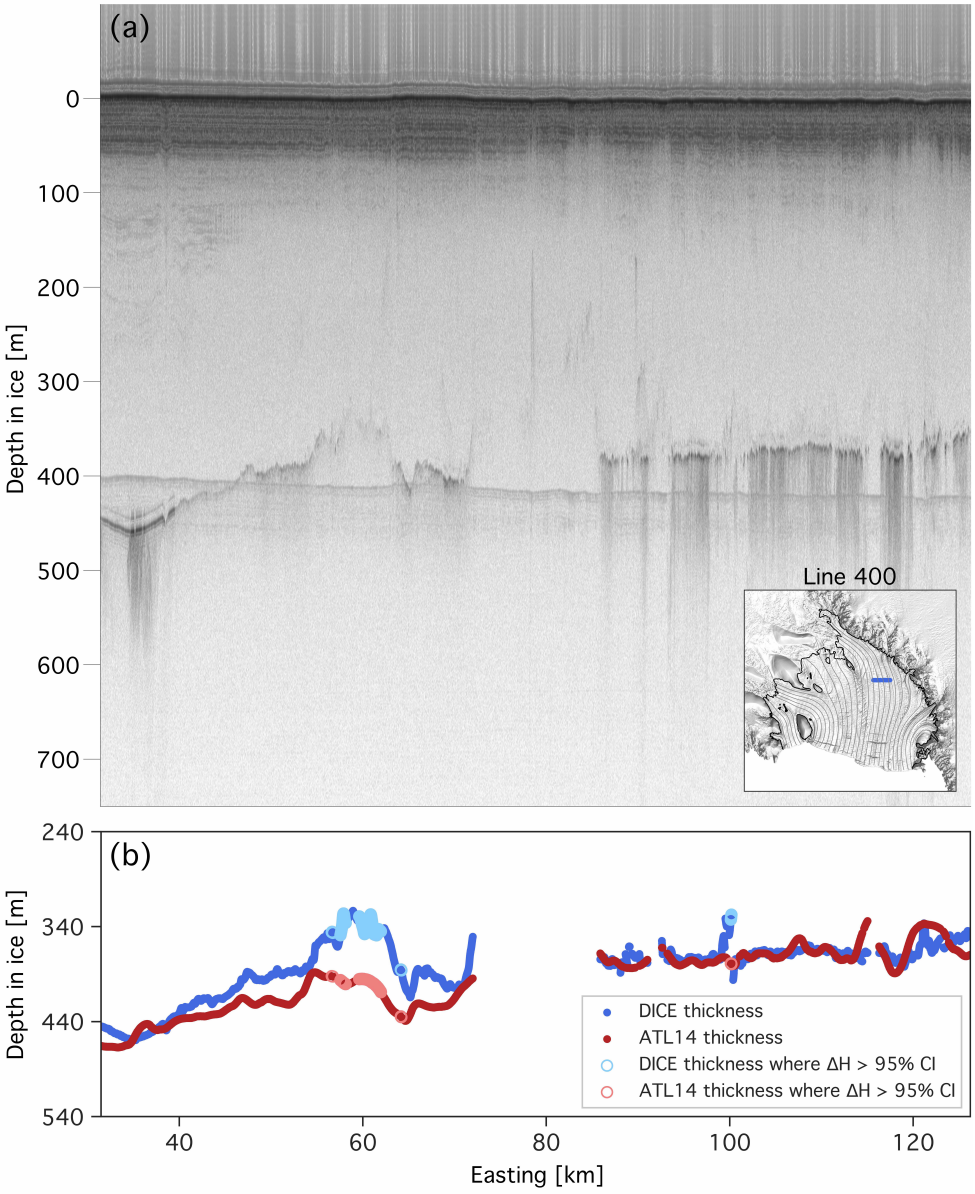

Figure 2.6: (a) DICE radargram segment for ROSETTA-Ice survey line L400, with the RIS surface at approximately 0 m depth and the basal reflector the other major feature (apart from the surface multiple). Inset map shows the approximate location of the radargram segment on the hill-shaded version of the REMA mosaic, with the gray lines indicating streamlines derived from Rignot et al. (2017) velocity fields. (b) Coincident DICE- and ATL14-derived thicknesses (filled blue and red circles, respectively) and DICE- and ATL14-derived thicknesses in locations where the difference exceeds the local uncertainty (open light blue and light red circles, respectively). The projection in both panels is Antarctic Polar Stereographic with a standard latitude of 71°S and a standard longitude of 0°.

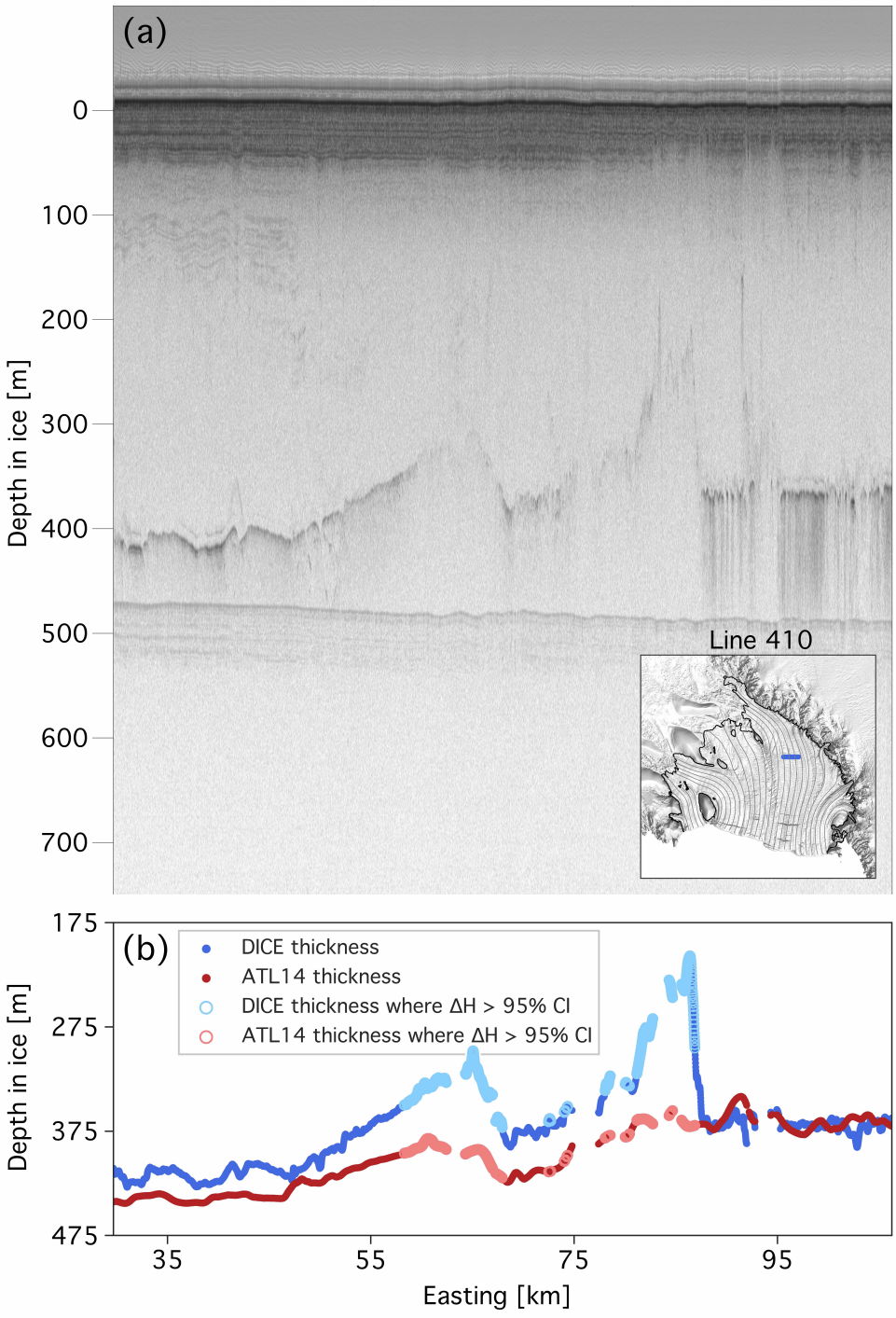

Figure 2.7: Same as Figure 2.6, but for ROSETTA-Ice survey line L410.

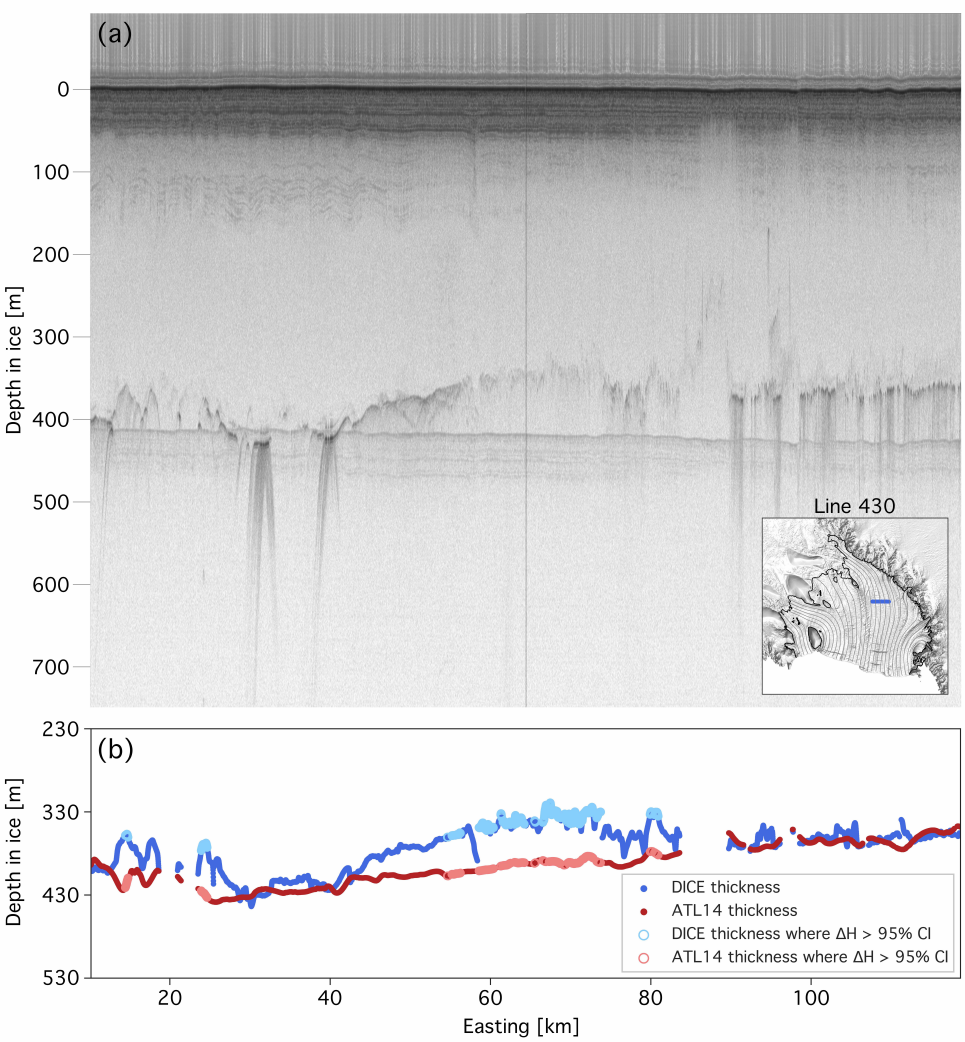

Figure 2.8: Same as Figure 2.6, but for ROSETTA-Ice survey line L430. Black vertical line in radargram in (a) indicates the stitch point between two component radargram images.

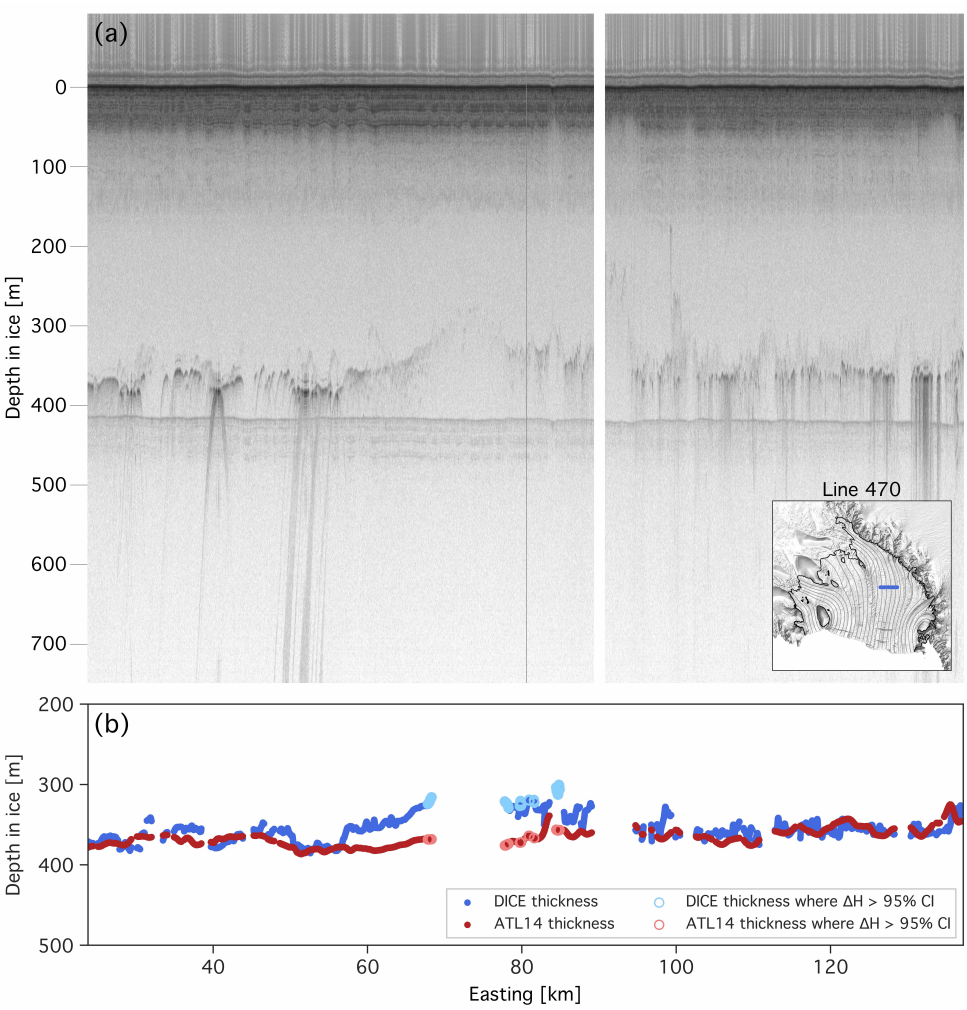

Figure 2.9: Same as Figure 2.6, but for ROSETTA-Ice survey line L470. Black vertical line in radargram in (a) indicates the stitch point between two component radargram images.

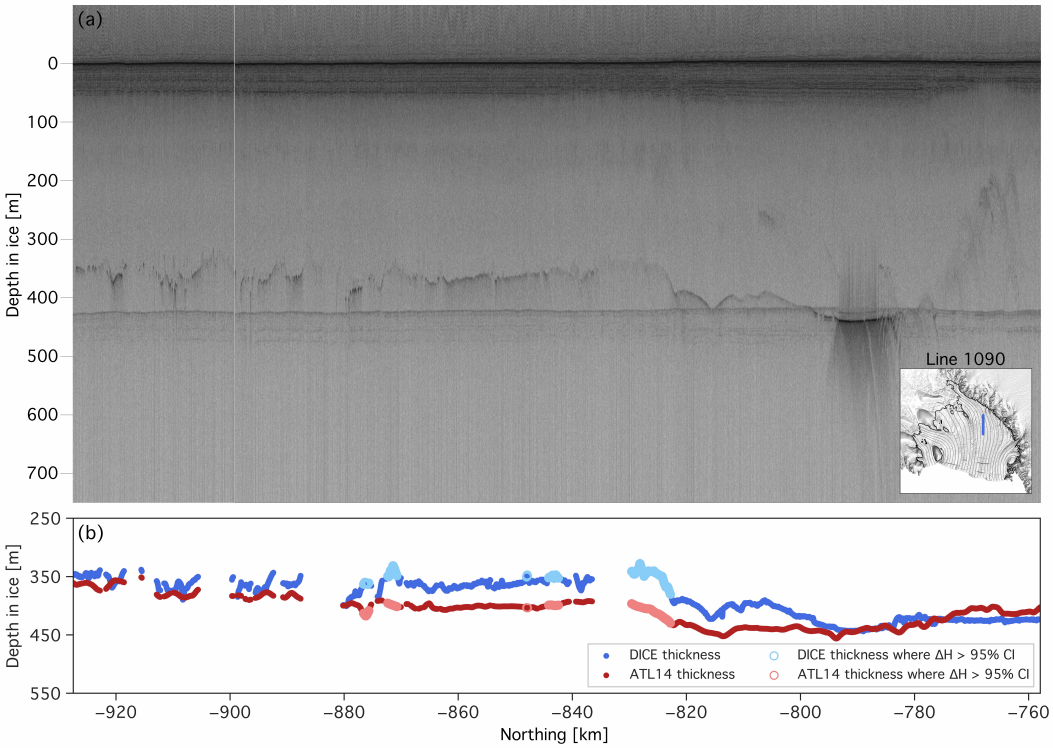

Figure 2.10: Same as Figure 2.6, but for ROSETTA-Ice survey line T1090. White vertical line in radargram in (a) indicates the stitch point between two component radargram images.

Table 2.1: Coefficients of and $\tilde{X}^2$ values for the best-fitting exponentials for the outer 60 and 10 km of the nine DICE thickness profiles used in the near-front melting analysis.

	Outer 60 km				Outer 10 km			
DICE survey line (region)	a	b	c	$\tilde{X}^2$	a	b	c	$\tilde{X}^2$
T1000 (1)	353	0.01	560	6.89	77.3	0.15	272	5.76
L780 crossing 1 (1)	73.9	0.26	311	3.60	71.5	0.38	303	3.27
L780 crossing 2 (2)	58.7	0.14	329	2.48	45.4	0.28	312	4.02
T1040 (3)	162	0.01	424	23.6	70.5	0.48	287	1.20
L830 (3)	119	0.13	275	5.37	122	0.13	277	3.04
L850 (3)	75.6	0.14	282	7.81	78.0	0.11	288	3.66
L890 (4)	126	0.07	231	20.8	122	0.23	188	0.60
L900 (5)	121	0.05	267	21.4	85.5	0.38	196	0.40
T1120 (6)	105	0.02	257	5.58	50.3	0.38	176	0.16

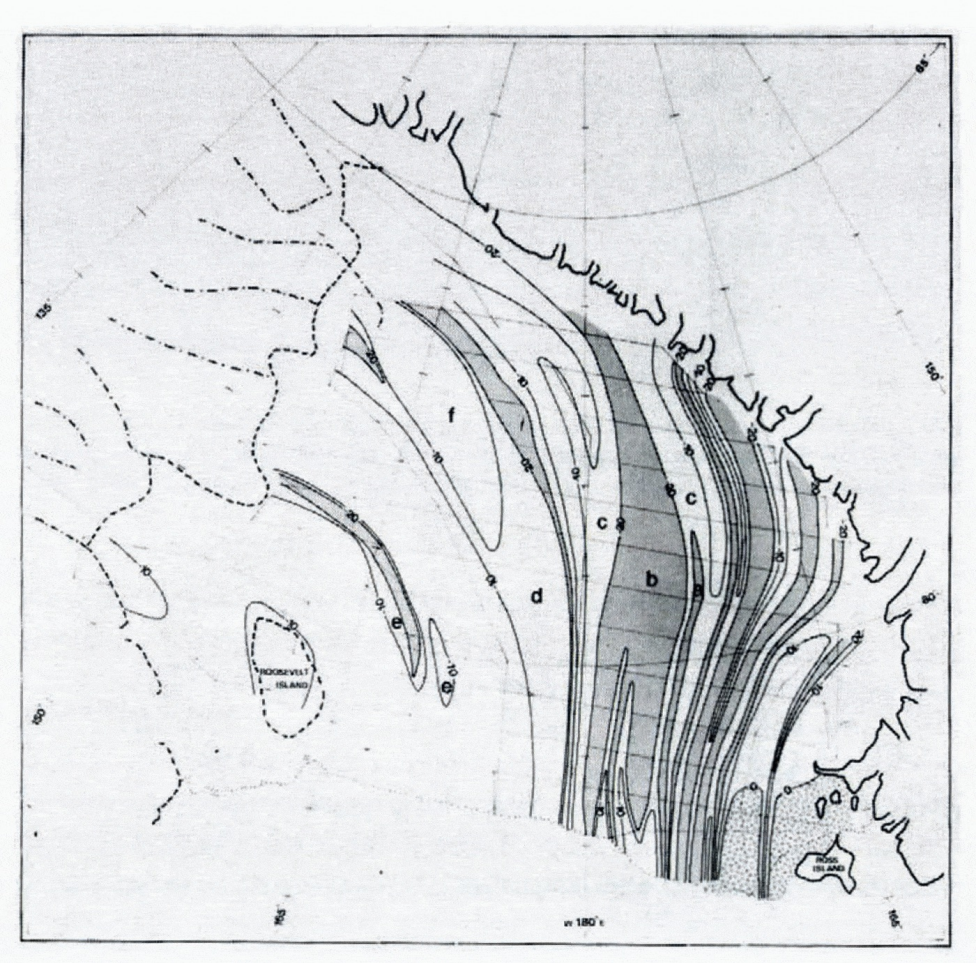

Figure 2.11: Reproduction of Figure 4 from Neal (1979), which shows the reflection coefficient of the ice–water interface, calculated from the mean of the peak received power during an airborne radio-echo sounding campaign in 1974–1975. The contour interval is 10 dB. Open shading indicates areas where the reflection coefficient exceeds 0 dB and heavy shading areas where it is less than –20 dB. Neal (1979) attributed the low reflection coefficients in zones a and b to the presence of basal marine ice. (Zone a is west, or to the right, of the northern portion of zone b.)

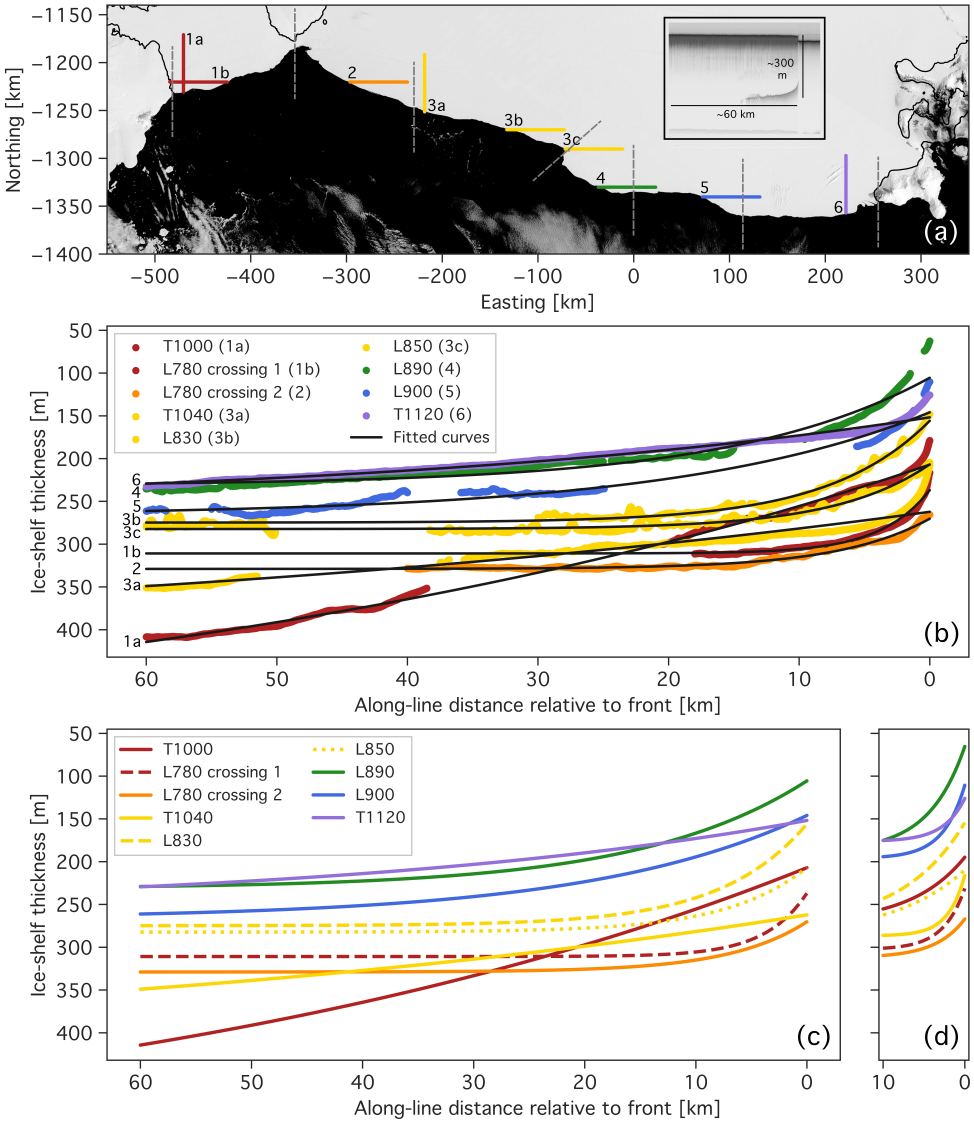

Figure 2.12: (a) Locations of the outer 60 km of nine DICE thickness profiles used in the near-front melting analysis, with profile annotations indicating region and/or profile identifier for regions with multiple profiles. Profiles are color-coded by along-front region, with region boundaries shown with dashed gray lines. Background is a February 4, 2016, Moderate Resolution Imaging Spectroradiometer image downloaded from NASA Worldview; the thin black line indicates the Depoorter et al. (2013) RIS mask. Inset shows the near-front segment of the SIR radargram for the roughly front-normal survey line T1110 as a reference for near-front basal topography. (b) Stacked DICE thickness profiles (color-coded by region) with profile identifiers indicating the locations shown in (a). Black lines show the corresponding best-fitting exponentials for the outer 60 km. Best-fitting exponentials for the outer (c) 60 and (d) 10 km of the thickness profiles in (b). The horizontal axis label below and legend in (c) also apply to (d).

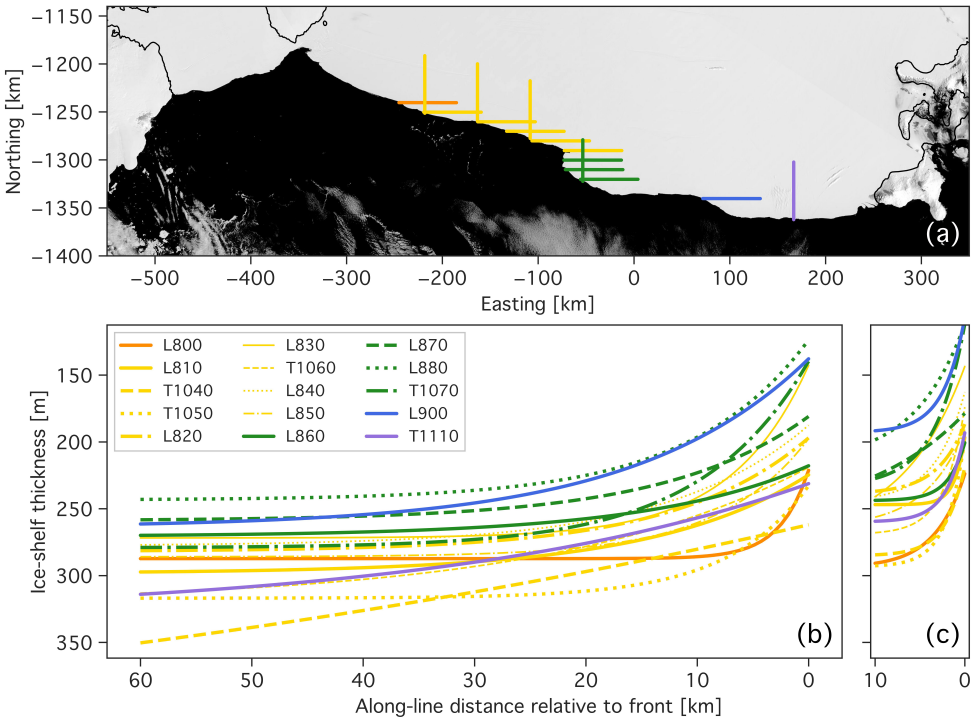

Figure 2.13: (a) Locations of the outer 60 km of 15 SIR thickness profiles used in the near-front melting analysis. Profiles are color-coded by along-front region, with colors and region boundaries shown in Figure 2.12a. Background and thin black line are as in Figure 2.12a. Best-fitting exponentials for the outer (b) 60 and (c) 10 km of the SIR thickness profiles whose locations are given in (a). The horizontal axis label below and legend in (b) also apply to (c).

Table 2.2: Coefficients of and $\tilde{X}^2$ values for the best-fitting exponentials for the outer 60 and 10 km of the 15 SIR thickness profiles used in the near-front melting analysis.

	Outer 60 km				Outer 10 km			
SIR survey line (region)	a	b	c	$\tilde{X}^2$	a	b	c	$\tilde{X}^2$
L800 (2)	66.0	0.38	287	6.05	70.4	0.30	294	11.2
L810 (3)	73.6	0.07	298	6.23	50.2	0.88	247	0.27
T1040 (3)	209	0.01	471	22.0	66.2	0.46	285	0.88
T1050 (3)	84.1	0.14	317	22.6	95.4	0.49	293	2.63
L820 (3)	84.9	0.08	282	4.63	52.2	0.33	239	10.4
L830 (3)	129	0.15	272	8.49	129	0.14	272	5.13
T1060 (3)	101	0.04	320	28.4	95.1	0.44	269	2.84
L840 (3)	90.2	0.08	278	21.0	82.0	0.31	245	2.08
L850 (3)	88.3	0.12	286	5.10	73.1	0.23	264	6.36
L860 (4)	52.9	0.07	271	7.94	43.2	0.53	244	4.22
L870 (4)	78.0	0.08	259	4.60	80.9	0.09	260	3.24
L880 (4)	120	0.09	243	6.51	104	0.18	216	0.55
T1070 (4)	140	0.10	279	25.4	121	0.30	233	2.95
L900 (5)	126	0.06	264	20.3	85.9	0.42	193	0.60
T1110 (6)	99.4	0.03	331	28.9	66.6	0.49	260	5.83

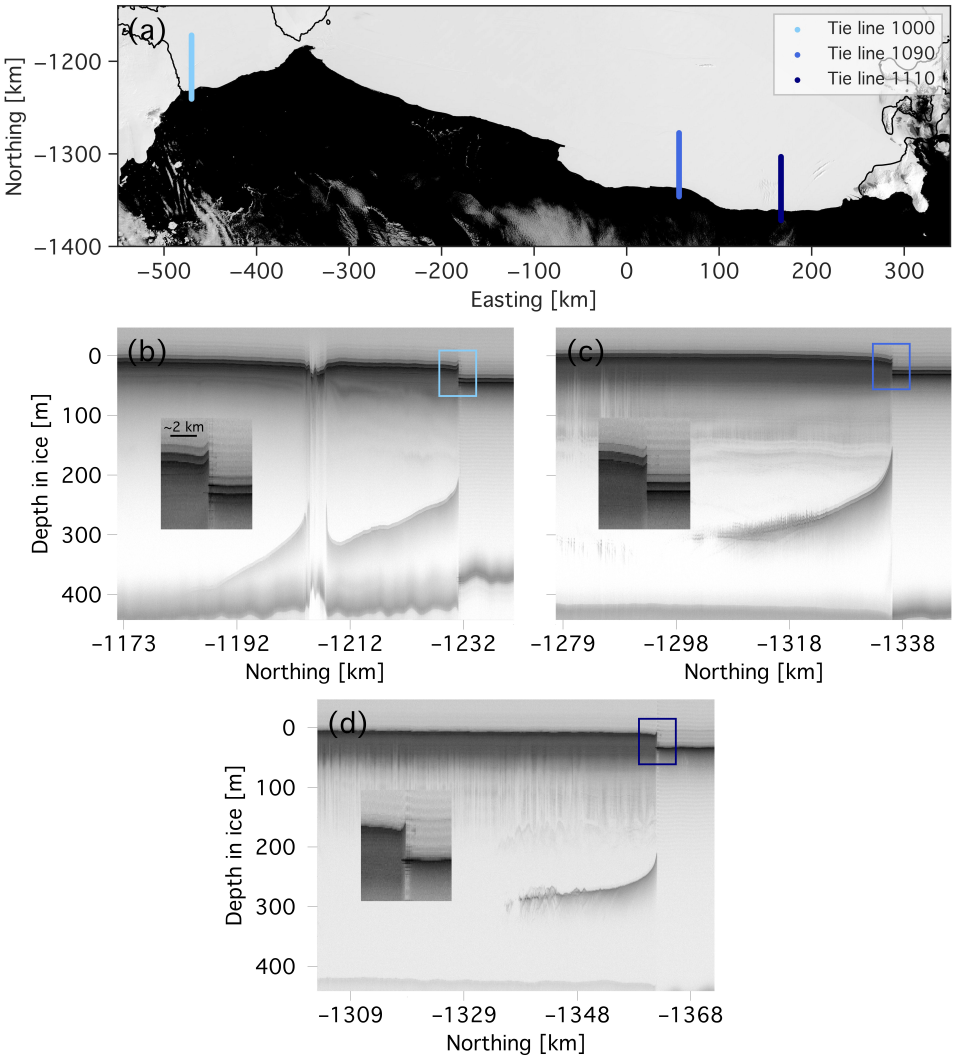

Figure 2.14: (a) Approximate locations of the near-front segments of the SIR radargrams for the roughly front-normal survey lines T1000, T1090, and T1110, which are shown in panels (b), (c), and (d), respectively. The background in (a) is a February 4, 2016, Moderate Resolution Imaging Spectroradiometer image downloaded from NASA Worldview; the thin black line indicates the Depoorter et al. (2013) RIS mask. The insets in (b), (c), and (d) provide a closer look at the surface feature discussed in the main text; the scale bar in the inset in (b) also applies to the insets in (c) and (d). The northing values in panels (b), (c), and (d) are approximate.

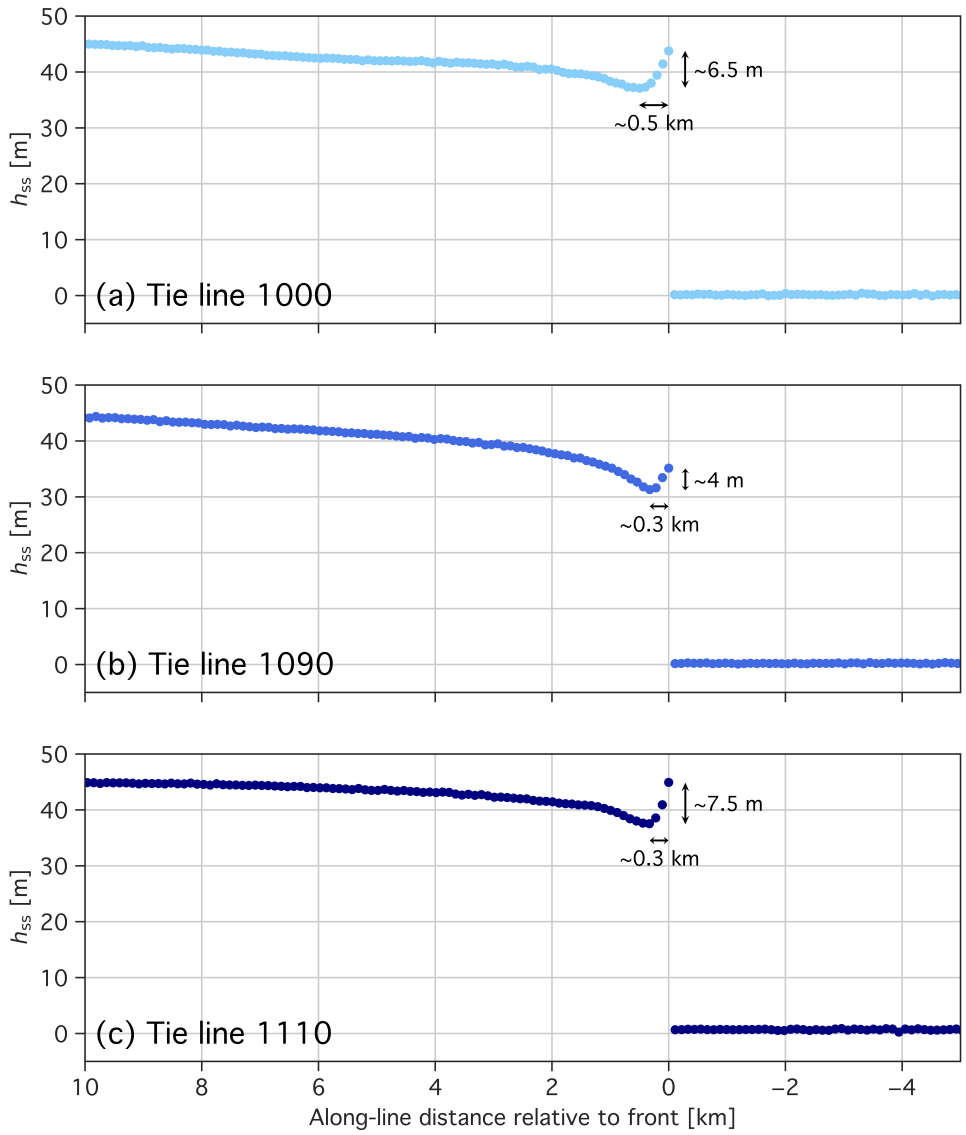

Figure 2.15: Observed rampart-moat (R-M) structures in near-front lidar nadir profiles of height above instantaneous sea surface (h_{ss}) for survey lines (a) T1000, (b) T1090, and (c) T1110. Arrows and annotations in each panel indicate the approximate along-line distance and difference in height between the "rampart" and "moat" of the corresponding R-M structure. Lidar nadir profile locations are the same as those of the SIR radargram segments in Figure 2.14a.

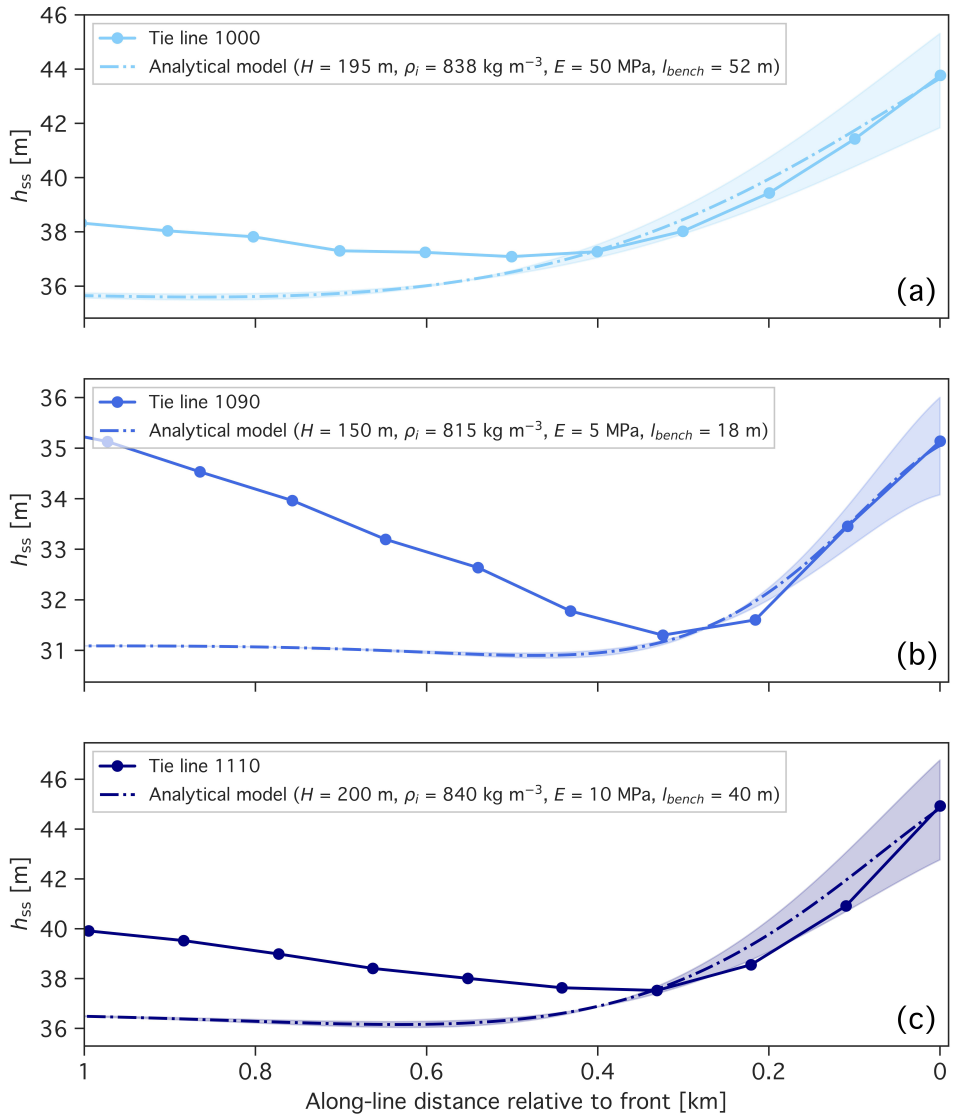

Figure 2.16: Comparison of observed R-M structures in near-front lidar nadir profiles of height above instantaneous sea surface (h_{ss}; solid lines with filled circles) for survey lines (a) T1000, (b) T1090, and (c) T1110 with the deflections predicted by the analytical elastic-beam model (dash-dotted lines). The model combines the effects of the upward (bench-driven) and downward (pressure-driven) bending moments at the ice front. The key model parameter values (thickness, H; column-averaged density, ρ_i; Young's modulus, E; and bench length, l_{bench}) for each predicted deflection are shown in the corresponding legend; the shading indicates the range of modeled deflections that would result from varying ρ_i by up to ±50 kg m^{-3}. The mismatch between the observed and modeled profiles upstream of the depression occurs because the model assumes a constant ice-shelf-beam thickness. Lidar nadir profile locations are the same as those of the SIR radargram segments in Figure 2.14a.

Chapter 3

Buoyancy-driven flexure at the front of Ross Ice Shelf, Antarctica, observed with ICESat-2 laser altimetry

3.1 Abstract

Mass loss from Antarctica's three largest ice shelves is dominated by calving, primarily of large tabular icebergs every few decades. Smaller, more frequent calving events also occur, but it is more difficult to detect them and quantify their contribution to total ice-shelf mass loss. We used surface elevation data from NASA's ICESat-2 laser altimeter to examine the structure of the Ross Ice Shelf front between October 2018 and July 2020. Profiles frequently show a depression a few meters deep about 200–800 m upstream of the front, with higher values on the eastern portion of the ice shelf. This structure results from bending due to buoyancy of a submerged ice bench generated by ice-front melting near the waterline when warm water is present in summer. These bending stresses may cause small-scale calving events whose frequency would change as summer sea ice and atmosphere–ocean heat exchanges vary over time.

3.2 Introduction

Antarctica's floating ice shelves have a substantial effect on the rate of dynamic ice loss from the grounded Antarctic Ice Sheet (e.g., Thomas, 1979). For most ice shelves, a decrease in their mass reduces back stresses acting on the upstream glaciers and ice streams, resulting in acceleration of grounded ice into the ocean (e.g., Gudmundsson et al., 2019; Scambos et al., 2004; Smith, Fricker, Gardner, Medley, et al., 2020) and global sea-level rise (Nerem et al., 2018; Shepherd et al., 2018). In steady state, mass loss from an ice shelf, through basal melting and iceberg calving, balances inflow of grounded ice across the grounding line and net precipitation onto the ice shelf. In recent decades, however, ice-shelf mass losses integrated around Antarctica have exceeded gains (e.g., Adusumilli et al., 2020; Depoorter et al., 2013; Rignot et al., 2013).

For the largest ice shelves (Ross (Figure 3.1a), Filchner-Ronne, and Amery), which are underlain by cold water and currently near steady state, multidecadal mean mass loss through iceberg production is estimated to exceed loss through basal melting (Depoorter et al., 2013; Rignot et al., 2013). The calving flux for these ice shelves is dominated by intermittent production of large (tens of kilometers long) tabular icebergs every few decades (e.g., Fricker et al., 2002; Lazzara et al., 1999; Walker et al., 2021). The extent and timing of these calving events are controlled by the lateral extension of full-thickness rifts to the ice front. This process is usually treated as essentially glaciological, governed by ice-shelf stress balances (e.g., Joughin and MacAyeal, 2005), with the ocean making only an indirect contribution through ice-shelf thinning by melting (Liu et al., 2015) and possible contributions from tides, swell, and tsunamis (e.g., Bromirski et al., 2010; Brunt et al., 2011; MacAyeal et al., 2006). However, some mass loss can be driven directly by ice–ocean interactions at the front, including the more frequent production of relatively small "sliver-shaped" icebergs (described by Kristensen (1983) as $<$2 km long and having at least one horizontal dimension on the order of the ice thickness).

One potential small-scale calving mechanism involves the development of a buoyant

subsurface ice "bench" (hatched area in Figure 3.1b) as warm near-surface water and surface-wave action cause the aerial portion of the ice front to collapse (e.g., Hughes, 2002; Orheim, 1987). The additional buoyancy bends the seaward ice edge upward, generating a surface "rampart" at the front and a depression (or "moat") upstream (Mosbeux et al., 2020; Scambos et al., 2005). The elevation difference (dh_{RM}) and horizontal distance (dx_{RM}) between the rampart and the center of the moat are, typically, a few meters and a few times the ice thickness (H), respectively (Scambos et al., 2005). Rampart-moat (R-M) structures have been observed at the edges of tabular icebergs as they drift into warmer upper-ocean water (Scambos et al., 2005, 2008; Wagner et al., 2014) and along the Ross Ice Shelf (RIS) front (Horgan et al., 2011; Mosbeux et al., 2020) where near-surface water warms in summer (Porter et al., 2019).

Mosbeux et al. (2020) applied an ice-shelf model to an idealized, constant-thickness ice shelf to quantify its flexural response to the buoyancy of the bench. An increase in buoyancy increases the associated internal ice stresses, which can lead to propagation of basal crevasses. If the stresses reach a critical value, the ice shelf will calve a relatively small, but full-thickness, iceberg along the crevasse. After the calving event, the new ice front will again be roughly vertical, with no bench. In that state, the dominant bending moment results from the difference in pressure between the ice shelf and the ocean along the ice front, which bends the upper edge seaward and downward (Reeh, 1968) by several meters to create a "berm" shape (Scambos et al., 2005). Berm structures are frequently found along ice fronts (e.g., Robin, 1979), where they can be reinforced by elevated rates of "mode-3" basal melting near the front (Horgan et al., 2011; Jacobs et al., 1992).

Until recently, we have lacked the ability to map surface elevation of Antarctica's extensive ice fronts at sufficiently high spatial resolution to fully resolve R-M structures. The 2018 launch of NASA's Ice, Cloud, and land Elevation Satellite-2 (ICESat-2) provides the first opportunity to overcome this observational limitation. Here, we demonstrate that ICESat-2 resolves R-M structures, map their presence along most of the RIS front, and examine along-front variability

of R-M spatial scales. We then discuss potential environmental drivers and implications of this process as ocean conditions change.

3.3 ICESat-2 over the RIS front

3.3.1 ICESat-2 mission

ICESat-2 was launched in September 2018 and began collecting scientific data in October 2018. The satellite carries the Advanced Topographic Laser Altimeter System (ATLAS), a photon-counting laser altimeter that transmits green (532 nm wavelength) light split into three pairs of beams (Markus et al., 2017). Each pair consists of a strong beam and a weak beam separated by 90 m; pairs are separated by 3.3 km on the ground during nominal performance. ATLAS pulses at 10 kHz, illuminating $\sim$10.6–12 m footprints (Magruder et al., 2020) every $\sim$0.7 m along each of the six ground tracks (GTs). GTs are nominally centered on 1,387 reference ground tracks (RGTs), which extend to a latitude of 88° and are repeated once per 91-day cycle. ICESat-2 was off-pointed 1–4 km from its RGTs for the first two cycles (Smith, Fricker, Gardner, Medley, et al., 2020) but has been exactly following its RGTs over the polar regions since April 1, 2019.

3.3.2 Height data

We used the ICESat-2 ATL06 Land Ice Height product (Smith et al., 2019), which provides estimated heights (relative to the WGS84 ellipsoid) derived from 40 m along-track data segments that overlap by 50%, yielding 20 m spacing. Over flat parts of the Antarctic Ice Sheet, ATL06 data have accuracy and precision of $<$3 cm and $<$9 cm, respectively (Brunt et al., 2019). We used data from all six GTs per RGT. We examined Release 003 ATL06 data (Smith, Fricker, Gardner, Siegfried, et al., 2020) across the RIS front region from Cycle 1 to midway through Cycle 8

(July 16, 2020). We used the Python icepyx library (Scheick et al., 2019) to download a spatially subsetted data set of ATL06 files from the National Snow and Ice Data Center (NSIDC). The bounding box we applied, which spanned 77°S to 78.9°S and 163.5°E to 157.5°W, encompasses the entire RIS front.

For specific GTs, we also retrieved ATL03 Global Geolocated Photon Data files (Neumann et al., 2019) that provide estimates for latitude, longitude, and height relative to the WGS84 ellipsoid for all photons detected by ATLAS. We downloaded these profiles from NSIDC (Neumann et al., 2020) and used them to assess how well the ATL06 product resolves R-M structures (Section 3.4.1).

3.3.3 Ice-front and R-M detection

We automated detection of the ice front, R-M structures, and measurements of R-M spatial scales from ATL06 data using the following analysis steps:

1. *GT selection:* We used an ice-shelf mask (Depoorter et al., 2013) to select GTs that crossed the RIS front between Marie Byrd Land and the eastern tip of Ross Island (Figure 3.1a).

2. *GT filtering:* We removed GT segments with known data-quality issues, keeping only data for which the *atl06_quality_summary* flag equals 0.

3. *Height referencing and correction:* We converted all ellipsoidal height data (*h_li*) to height relative to the instantaneous sea surface by referencing them to the EGM2008 geoid (*geoid_h*, provided in the ATL06 product) and correcting for ocean tides ($tide\_ocean$), inverted barometer effects (*dac*), and mean dynamic topography (*mdt*), using $h_{ss} = h\_li - geoid\_h - tide\_ocean - dac - mdt$. We obtained the values for $tide\_ocean$ and *dac* from the GOT4.8 model and MOG2D dynamic atmosphere correction values provided in the ATL06 product; we applied a constant value of –1.4 m for *mdt* (Andersen et al., 2015). We then removed outliers ($h_{ss} < -5$ m or $h_{ss} > 100$ m).

4. *Front detection:* Our front-detection algorithm scans GT profiles from the ocean to the ice shelf. We interpreted segments with $h_{ss} < 2$ as the ocean surface; we selected this threshold to allow for the presence of snow-covered sea ice and uncertainties in the geophysical corrections. For each GT, the algorithm steps landward from the most seaward ocean point until it detects a height increase of 10–100 m over less than 80 m distance along track, where the starting point of the jump is an ocean point. The algorithm identifies the ice front as the location of the first point on the high side of the jump. It occasionally located the ice front at the northern edges of small icebergs in the Ross Sea, in regions of near-front rifting (e.g., seaward of Roosevelt Island), and on the ice shelf when ATL06 data are missing over the true ice front and the surface within a rift has $h_{ss} < 2$ m. We manually removed tracks where the detected ice front was clearly inconsistent with the full data set and nearly contemporaneous MODIS imagery.

5. *R-M detection:* For all ice-front segments, we defined the rampart surface height (h_R) as the highest point within 100 m of the front. This was usually the first ATL06 value on the ice shelf; however, sometimes the ice front in the ATL06 profile included one or more lower points resulting from the overlapping averaged segments or true structure on the aerial portion of the ice face. Moving landward, we then searched in the GT profile for elevations lower than h_R that were less than 2 km (along track) from the front; this threshold is based on the expected location of moats within a few ice thicknesses of the front (Mosbeux et al., 2020; Scambos et al., 2005) and the orientation of RGTs being roughly orthogonal to the front for RIS (Figure 3.1a). If successful, we recorded the lowest point of the first detected depression as the moat with height h_M.

6. *R-M quantification:* For each GT profile that showed an R-M structure, we computed two parameters to define its geometry: dh_{RM} (= $h_R - h_M$) and dx_{RM} as the difference in height and along-track distance, respectively, between the rampart and the center of the moat

(Figures 3.1b–3.1c).

3.3.4 Estimation of ice thickness

We estimated ice thickness (H) from ATL06-derived values of h_{ss} ∼3 km upstream (along track) of the rampart, which for almost all RGTs used in this study (Figure 3.1a) is upstream of the expected zone of R-M flexure (Mosbeux et al., 2020; Figures 3.1b–3.1d). We converted h_{ss} to ice-equivalent thickness (H_{eq}) by assuming hydrostatic equilibrium, ice density of 917 kg m^{-3}, seawater density of 1028 kg m^{-3}, and firn air content (H_{fac}) derived from GSFC-FDM v1 simulations (updated from those performed in Smith, Fricker, Gardner, Medley, et al., 2020). We then computed H as the sum of H_{eq} and H_{fac}.

3.4 Results

In our region of interest, there were 8,191 GTs that crossed the RIS front. We were unable to identify the ice front for 3,953 of these. Clouds (identified with the ATL06 *cloud_flg_atm* parameter) were responsible for most (3,726) of the failed front detections, whereas our algorithm could not detect the front in 227 GT profiles. Of the 4,238 GT profiles with detected fronts, 348 occurred seaward of Roosevelt Island or on icebergs in the Ross Sea. We detected R-M structures (step 5 above) along 2,893 of the remaining 3,890 profiles (∼74%). Thus, 997 (∼26%) of these GT profiles exhibit a monotonically increasing surface profile, or berm structure, within 2 km of the detected front; this arises from a combination of pressure imbalance at the ice front, mode-3 basal melting, and ice spreading. We report only the results of step 5 for the GT profiles for which we could compute a physical H, that is, that also contained high-quality data outside of rifts ∼3 km upstream of the detected rampart. There were 2,826 GT profiles (∼73% of the 3,890 profiles described above) for 221 RGTs that satisfied this criterion.

3.4.1 ICESat-2 resolution of rampart-moat structures

The profiles of ATL03 signal photons (see example in Figure 3.1c) reveal the ice front and R-M structures; however, quantifying surface heights and rampart and moat locations requires assumptions about the near-surface photon distribution and consideration of uncertainties in geolocation of individual photons. The ATL06 algorithm applies additional photon filters, instrumental corrections, and photon scattering statistics to retrieve ice-surface height from geolocated photons (Smith et al., 2019). This allows us to identify the along-track locations of the rampart and moat to an accuracy of 20 m and quantify the vertical and horizontal scales of the R-M structure, with minimal reduction in dh_{RM} relative to the value we would obtain from ATL03 signal photons. We conclude that ATL06 is well suited to our application of analyzing R-M structures.

3.4.2 Along-front variability of rampart-moat characteristics

The multi-beam sampling and RGT spacing of ICESat-2 over RIS provide along-front sampling of $\sim$1–3 km during a single cycle (Figure 3.1d). Derived R-M parameters are consistent between the weak and strong beam GT profiles that are 90 m apart; however, we sometimes observed large variability between beam pairs (3.3 km apart) for the same RGT and between RGTs. For example, for the Cycle 7 repeat of RGT 0487, beams gt3l (weak) and gt3r (strong) showed an R-M structure with $dh_{\mathrm{RM}} \approx 9.5$ m, whereas the other two beam pairs ($\sim$3.3 and $\sim$6.6 km away) showed R-M structures with $dh_{\mathrm{RM}} \approx$ 1–2 m.

We evaluated the statistics of dh_{RM} and dx_{RM} for all available ICESat-2 cycles for seven regions along the ice front (Figure 3.2a), chosen to approximate the regions used by Horgan et al. (2011) in their estimation of mode-3 basal melt rates but adjusted to match pronounced streaklines representing major suture zones between distinct ice flow units. Broadly speaking, the values of both dh_{RM} and dx_{RM} (Figures 3.2b–3.2e) are larger on the eastern portion of the front (regions

1–4) than on the western portion (regions 5–7). On the eastern portion, regional histograms of dh_{RM} mostly have peaks and average values greater than 5 m; on the western portion of the front, peaks and averages are typically at values of dh_{RM} below 5 m. There is a similar divide in the distribution of dx_{RM}. Whereas most of the GT profiles that cross the eastern RIS front have dx_{RM} values between 300 and 500 m, GT profiles across the western RIS front mostly have values between 100 and 300 m, resulting in lower regional averages.

We found no evidence of significant changes in R-M statistical characteristics over the October 2018–July 2020 ICESat-2 record. Instead, we interpret the variability of R-M characteristics on scales of a few km along the front (Figure 3.1d) as evidence that the buoyancy of the bench varies on similar length scales. If so, the spread of dh_{RM} values within a region probably represents the different stages in the life cycles of the R-M structures. Although R-M structures are typically larger in both dh_{RM} and dx_{RM} on the eastern portion of the front, there are R-M structures with small dh_{RM} in all seven regions. Berm structures also occur along the RIS front, but our results suggest that they are more prevalent on the eastern portion of the front ($\sim$30% of all GTs) than on the western portion ($\sim$22%) (Figure 3.2b).

3.5 Discussion

3.5.1 Drivers of spatial patterns in ice-front shape

Prior modeling studies of R-M structures suggest that their spatial scales are determined by ice thickness and ocean properties, and we discuss each of these below.

(i) *Ice thickness (*H*):* We expect from modeling (Mosbeux et al., 2020) that the characteristics of R-M structures depend on H near the ice front (Figures 3.2c–3.2d and 3.3). The observed values of dh_{RM} and dx_{RM} along the RIS front suggest that the distribution of both parameters is at least partially related to H. Near-front H is influenced by mode-3

basal melting (Horgan et al., 2011) and by ice advection, with ice on the eastern portion of RIS (fed by the West Antarctic Ice Sheet) being generally thicker than ice on the western portion of RIS (fed by the East Antarctic Ice Sheet).

We hypothesize that the relationship between R-M spatial scales and H occurs because a submerged bench of a specified length along the thicker eastern portion of the RIS front will occupy a greater volume than a bench of the same length along the thinner western portion of the RIS front. Assuming ice and ocean density do not vary significantly, this greater volume increases the upward bending moment imparted by the buoyant bench (Figure 3.1b), which in turn increases dh_{RM}. We expect that dx_{RM} will also be greater for thicker benches, as the bending stiffness of the ice shelf increases with H (e.g., Mosbeux et al., 2020; Wagner et al., 2014). However, the volume of the buoyant bench also has a second-order control on dx_{RM}. The positions of the maximum tensile stress and the moat migrate seaward as the bench grows, converging to a value fixed by the mechanical stiffness of the ice shelf (Mosbeux et al., 2020). Thus, we require additional information about the geometry of the bench to fully characterize the relationship between H and dx_{RM}. The evolution of both dh_{RM} and dx_{RM} may also be related to local rheology and the profile of ice and firn density, as well as preexisting topography associated with rifts (Walker et al., 2021).

(ii) *Ocean properties:* The principal ocean drivers of bench development are near-surface ocean temperature and surface waves (Kristensen et al., 1982; Scambos et al., 2008). For the southern Ross Sea, measured upper-ocean temperatures are significantly above the freezing point only in summer when sea ice has disappeared (Porter et al., 2019). No direct measurements of surface waves are available along the RIS front, but we expect them to be generally small because sea ice effectively dampens surface waves propagating southward (Horvat et al., 2020), and near-front waves generated by the prevailing northward wind stress across the ice front (Tinto et al., 2019) will be small.

The southern Ross Sea is typically free of sea ice in summer, as the Ross Sea Polynya (Figure 3.3) expands northward from the ice front beginning in December. The observed mean summertime (December–February) 15% sea ice concentration contour for 1999–2019 (Figure 3.3), derived from monthly passive microwave data (Meier et al., 2017; Peng et al., 2013), is about 100 km north of the eastern ice front and extends several hundred km farther north in the western Ross Sea. The mean summertime sea surface temperature (SST) from monthly averaged outputs from the fifth generation of the European Centre for Medium-Range Weather Forecasts (ECMWF) Re-Analysis (ERA5; Hersbach et al., 2019) for the same period shows warmer surface water in the western Ross Sea $\sim$100 km north of the RIS front (Figure 3.3), but it does not show the relatively warm SSTs close to the front reported by Porter et al. (2019).

These sea ice concentration and SST products suggest that, contrary to our observations (Figure 3.2), near-front summer ocean and sea ice conditions in the western Ross Sea are more conducive to development of a buoyant bench and R-M growth than in the eastern Ross Sea. We speculate that small-scale ocean processes near the ice front in the eastern Ross Sea lead to development of a more appropriate temperature profile for bench formation (with most ocean heat remaining very close to the ocean surface) than in the western portion, where downwelling of ocean heat, strong mode-3 basal melting (Stewart et al., 2019; Tinto et al., 2019), and mode-3-associated production of cold and fresh meltwater (Malyarenko et al., 2019) might impede the growth of a buoyant bench.

3.5.2 Implications for calving

The tensile stress associated with bench-driven bending of the ice shelf, although generally much smaller than the yield stress of pure ice ($\sim$1 MPa; Mosbeux et al., 2020), could widen preexisting basal crevasses and ultimately lead to calving, as has been observed at outlet glaciers in Greenland (e.g., James et al., 2014). The environmental conditions, near-surface ocean warming

and surface waves, that drive increases in bench buoyancy only occur in austral summer. We speculate that projected changes in summer sea ice (e.g., Bracegirdle et al., 2008; Lenaerts et al., 2016; Massom and Stammerjohn, 2010) could alter both surface warming (Porter et al., 2019) and wave action (Horvat et al., 2020) necessary for bench formation, which in turn would change the relative contribution of R-M-style calving to ice-shelf mass loss. We note, however, that conditions favorable for increased bench formation may also drive mode-3 basal melting (Jacobs et al., 1992; Stewart et al., 2019), such that the interplay of both processes is likely to determine the total rate of mass loss along the ice front.

3.6 Summary and outlook

We have used surface elevation data from NASA's ICESat-2 laser altimeter to map rampart-moat (R-M) structures along the front of RIS. These structures are driven by ice flexure due to excess buoyancy from submerged benches of ice that form along the front as warm near-surface water and surface waves create notches in the ice face near the waterline, leading to collapse of the overhanging aerial ice front. We propose that bending stresses acting on preexisting crevasses can lead to calving of small-scale sliver icebergs, contributing to net mass loss from Antarctic ice shelves. Climate-forced changes in this mechanism of mass loss would alter the distribution of freshwater input to the upper ocean in the Ross Sea, and may influence the rate of grounded-ice loss in the Ross Sea sector if the changes occur in regions of high buttressing, such as the area east of Ross Island (Fürst et al., 2016; Reese et al., 2018). Ice-shelf fronts, which advance at rates of order 1 km a^{-1}, also provide a relatively stationary environment for repeat observations of the R-M formation process, which appears to be critical to the destruction of large drifting icebergs, affecting the distribution of glacial meltwater input into the Southern Ocean (England et al., 2020).

Although we focused here on the RIS front, R-M structures exist on other large Antarctic

ice shelves, such as the Filchner-Ronne and Amery, where summer environmental conditions are conducive to bench development. Ultimately, improved understanding and quantification of R-M-driven calving will involve a combination of new observations of subsurface ice-front shape (Fried et al., 2015; Orheim, 1987) and time-varying upper-ocean temperature profiles, additional high-resolution elevation and ice-thickness data from the ongoing ICESat-2 mission and CryoSat-2 (Wuite et al., 2019), and observation-based improvements to ice-shelf models that incorporate the reduced yield stress associated with preexisting crevasses.

As the ICESat-2 mission progresses, its data will provide insight into the temporal evolution of R-M structures, including the timescale of development, potential calving, and redevelopment, across all ice shelves. This information will be critical for quantifying the relative contribution of the R-M mechanism to the overall calving flux and for predicting how this contribution might change in a warming Southern Ocean.

3.7 Data availability statement

ICESat-2 Version 3 ATL03 (https://nsidc.org/data/atl03) and ATL06 (https://nsidc.org/data/atl06) data are available at NSIDC. The Python code for data download and the MATLAB code for front and R-M structure detection are available via Zenodo: http://doi.org/10.5281/zenodo.4697517. The authors acknowledge the use of imagery from the NASA Worldview application (https://worldview.earthdata.nasa.gov), part of the NASA Earth Observing System Data and Information System, and elevation data from the Reference Elevation Model of Antarctica (http://data.pgc.umn.edu/elev/dem/setsm/REMA/mosaic/). Sea ice concentration data are from the NOAA/NSIDC Climate Data Record of Passive Microwave Sea Ice Concentration, Version 3 (https://nsidc.org/data/g02202/versions/3). The authors obtained ERA5 monthly averaged reanalysis outputs of SST, for the years 1999–2019, from modified Copernicus Climate Change Service information (2020; https://cds.climate.copernicus.eu/cdsapp#!/dataset/reanalysis-era5-

single-levels-monthly-means); neither the European Commission nor ECMWF is responsible for this use of the Copernicus information and component data.

3.8 Acknowledgments

The authors thank the OpenAltimetry team for their assistance in accessing data and the ICESat-2 Science Team, particularly the Land Ice group, for their input on the interpretation of ICESat-2 data near ice fronts. The authors are grateful to Brooke Medley for sharing the updated values of H_{fac} from the GSFC-FDM v1 simulations. The authors also thank the editor and two anonymous reviewers for their constructive comments on earlier versions of this manuscript. This study was funded by NASA grants 80NSSC20K0977, NNX17AG63G, and NNX17AI03G and by NSF grants 1443677 and 1443498.

Chapter 3, in full, is a reprint of the material as it appears in the journal *Geophysical Research Letters*. Becker, M. K., Howard, S. L., Fricker, H. A., Padman, L., Mosbeux, C., & Siegfried, M. R. (2021). Buoyancy-driven flexure at the front of Ross Ice Shelf, Antarctica, observed with ICESat-2 laser altimetry. *Geophysical Research Letters*, *48*(12), e2020GL091207. doi: 10.1029/2020GL091207. The dissertation author was the primary investigator and author of this paper.

Figure 3.1: (a) Map showing the distribution of Ice, Cloud, and land Elevation Satellite-2 (ICESat-2) reference ground tracks (RGTs) near the Ross Ice Shelf (RIS) front (ascending in red and descending in blue) overlaid on a December 2, 2018, Moderate Resolution Imaging Spectroradiometer (MODIS) image downloaded from NASA Worldview. The Depoorter et al. (2013) ice-shelf mask is shown with a black line. Gray lines on the ice shelf show modern ice streamlines derived from Rignot et al. (2017) velocity fields, with the streamline delineating the boundary between ice originating from the West and East Antarctic ice sheets (WAIS and EAIS, respectively) in thicker black. Inset map (created using Antarctic Mapping Tools data; Greene et al., 2017) features the Mouginot et al. (2017) WAIS–EAIS boundary. (b) Schematic of ice-shelf bench (hatched area), R-M structure, and the conditions under which the bench forms. Three relevant R-M parameters, relative height (dh_{RM}), relative along-track distance (dx_{RM}), and near-front thickness (H), are indicated. (c) Height above instantaneous sea surface for Cycle 7 ICESat-2 ATL03 signal (light blue dots) and background (gray dots) photons, and ATL06 segments (dark blue dots) for gt3r (strong beam) for RGT 0487, which is labeled in (a). ATL06-derived rampart and moat locations are marked as red crosses. (d) ATL06 height above instantaneous sea surface for all beams for Cycle 7 repeats of, from east to west along the front, RGTs 1371 (June 24, 2020), 0724 (May 12, 2020), 0487 (April 27, 2020), and 0785 (May 16, 2020). Dashed lines connect the ice-shelf (left) side of the profiles to the ocean (right) side but do not represent real ATL06 data. The four RGTs shown in (d) are indicated in (a) by thicker lines compared to the other RGTs.

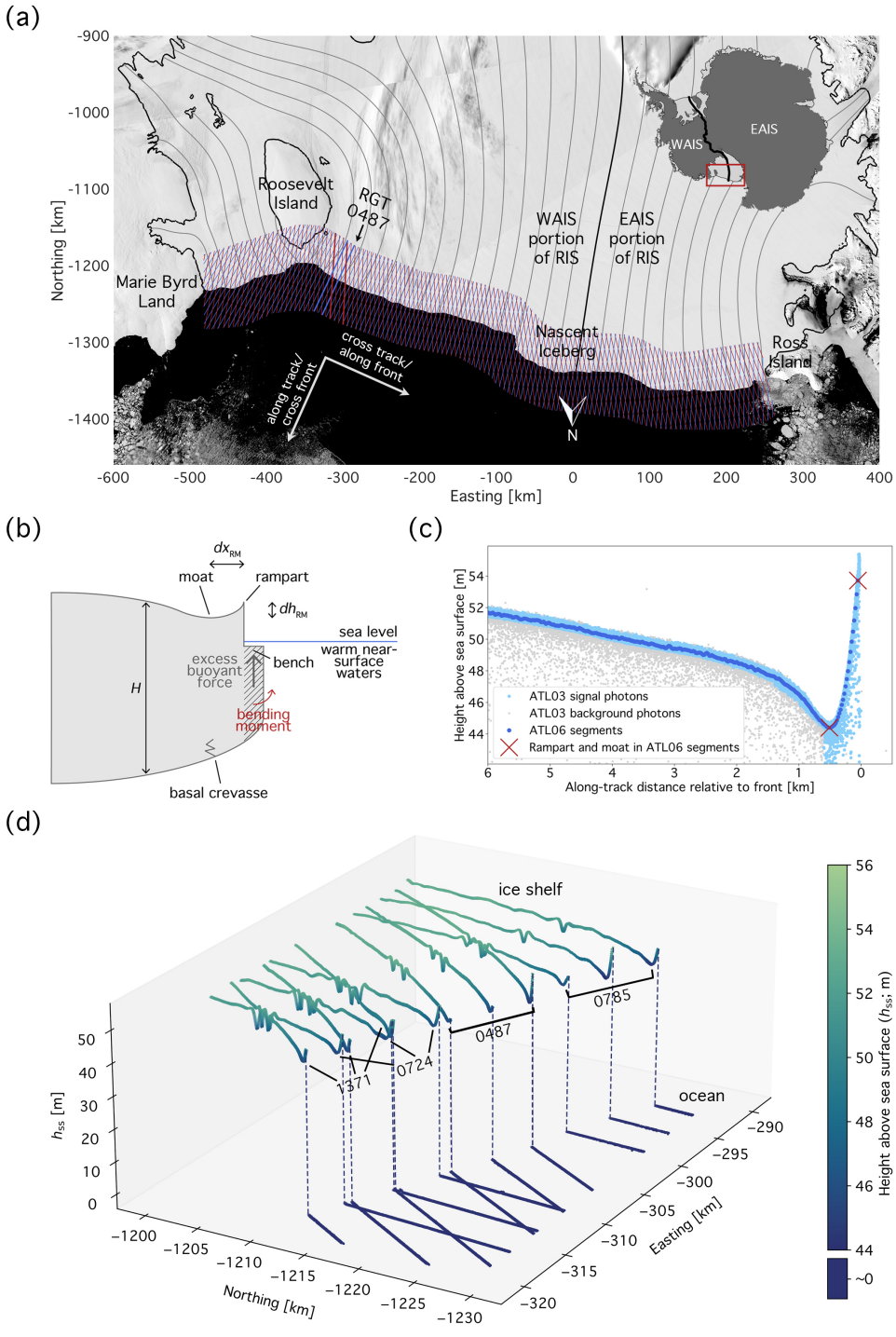
(a)
Northing [km]
Easting [km]
Roosevelt Island
RGT 0487
Marie Byrd Land
WAIS portion of RIS
EAIS portion of RIS
Nascent iceberg
Ross Island
WAIS
EAIS
cross track/ along front
along track/ cross front
N
(b)
moat
rampart
sea level
warm near-surface waters
bench
excess buoyant force
bending moment
basal crevasse
H
(c)
Height above sea surface [m]
Along-track distance relative to front [km]
ATL03 signal photons
ATL03 background photons
ATL06 segments
Rampart and moat in ATL06 segments
(d)
ice shelf
ocean
0785
0487
0724
0371
Northing [km]
Easting [km]
Height above sea surface (hss; m)

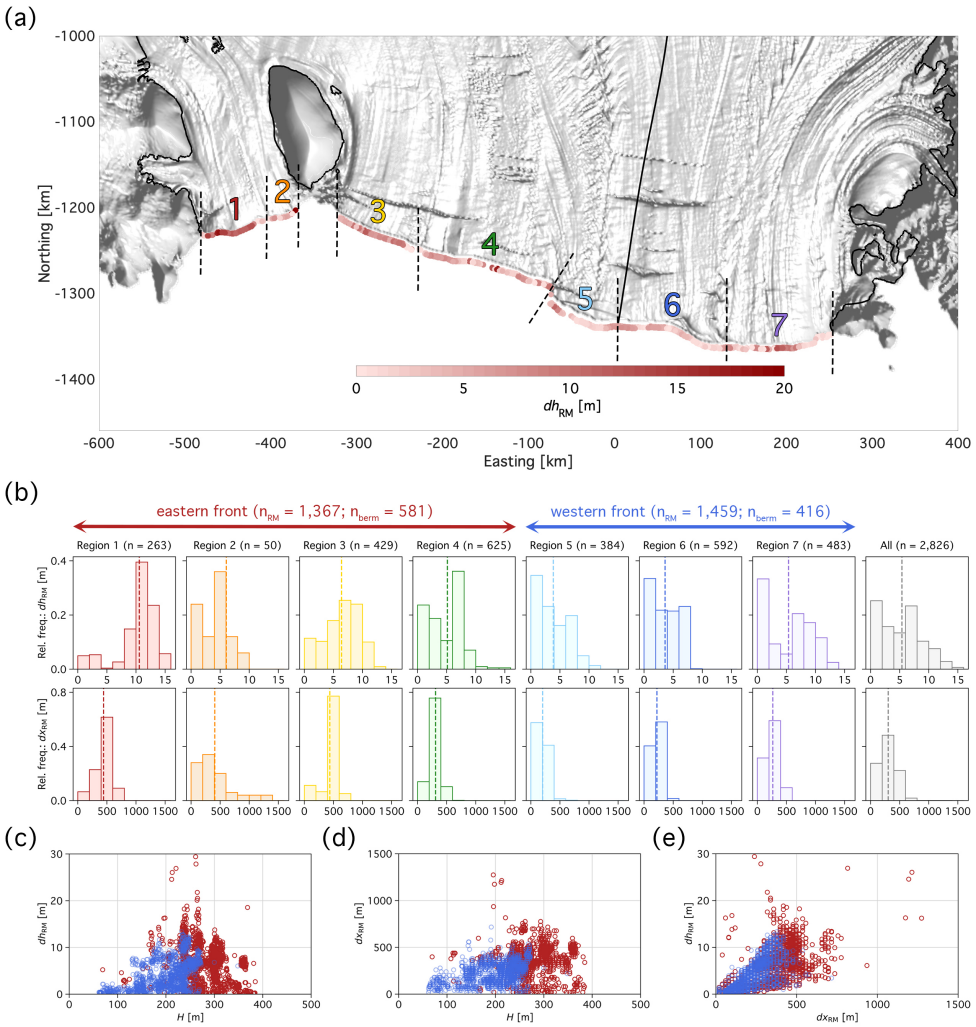

Figure 3.2: (a) Colored dots show along-front distribution of dh_{RM} (see Figure 3.1b for definition) from the 2,826 ICESat-2 ATL06 ground track (GT) profiles for which we could identify an R-M structure on the RIS front and compute ice thickness (H), overlaid on a hill-shaded version of the Reference Elevation Model of Antarctica (REMA) mosaic (Howat et al., 2019). GT profiles are for all ICESat-2 cycles (October 2018 to July 2020) available at the time of writing. Dashed black lines across the front indicate boundaries of seven regions used in regional statistical analysis of R-M parameters. Ice-shelf mask and streamline dividing WAIS from EAIS shelf ice are as in Figure 3.1a. (b) Relative frequency histograms of dh_{RM} (top row) and dx_{RM} (bottom row) for each region defined in (a) and for the entire front ("All"; rightmost column). Dashed vertical lines indicate mean values for each region. Region numbers and numbers of profiles with R-M structures per region (n) are above each column. Arrows at top of (b) specify the eastern (regions 1–4) and western (regions 5–7) portions of the front; numbers of R-M structures and berm-type profiles observed in each portion are indicated. Lower panels provide scatterplots of (c) dh_{RM} versus H, (d) dx_{RM} versus H, and (e) dh_{RM} versus dx_{RM} for all 2,826 GT profiles, color coded red (blue) if they occurred on the eastern (western) portion of the front.

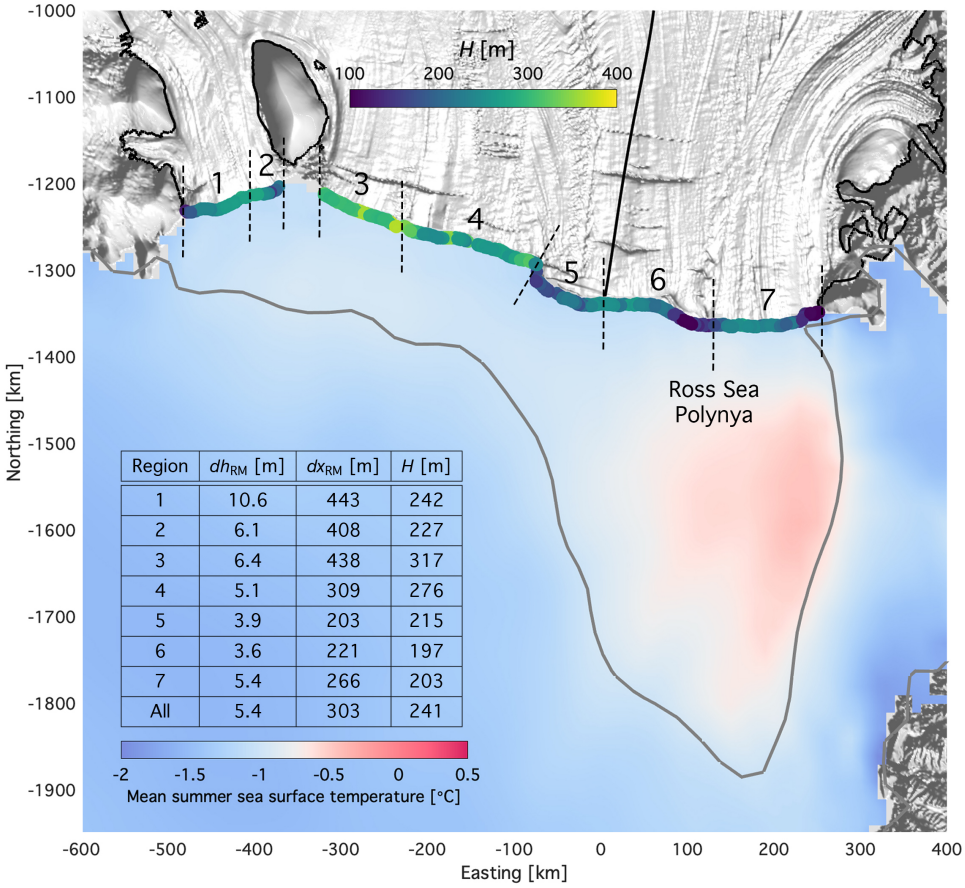

Figure 3.3: Potential drivers of observed patterns in R-M geometry. Background (hill-shaded REMA mosaic from Howat et al., 2019) shows streaklines delineating ice flow of different glacial units on RIS. The mean summertime SST for the period 1999/2000 to 2018/2019 from Hersbach et al. (2019), extrapolated to meet the RIS front, is shown by blue–red shading. Thick gray line shows the mean summertime 15% sea ice concentration contour (Meier et al., 2017; Peng et al., 2013) for the same period. Ice-shelf thickness (H) 3 km upstream (along track) from the ice front is indicated by the colored dots. Region boundaries are as in Figure 3.2; ice-shelf mask and streamline dividing WAIS from EAIS shelf ice are as in Figure 3.1a. The inset table shows mean values of dh_{RM}, dx_{RM}, and H for each region and for the full front ("All").

Chapter 4

Evolution of frontal topography on Ross Ice Shelf, Antarctica, due to changes in buoyancy-driven flexure

4.1 Abstract

Antarctic ice fronts represent a dynamic interface between ice, ocean, and atmosphere. To project the future of the Antarctic Ice Sheet, coupled models must represent processes at this interface. One process is the development of a submerged bench of ice through waterline erosion; the associated torque from buoyancy can deform the ice front and induce bending stresses that may lead to small-scale calving. We examined "rampart-moat" (R-M) surface structures associated with this flexure along the front of Antarctica's Ross Ice Shelf (RIS) in ICESat (2003–2009) and ICESat-2 (2018–2022) satellite altimetry data. R-M structures during both periods are larger on the eastern side of the RIS front. Overall, heights of R-M structures increased during the ICESat-2 period, with growth being largest along the eastern front. Downsampling the ICESat-2 data to ICESat resolution allowed us to compare R-M characteristics from both

missions, revealing longer-term growth along parts of the front that calved large icebergs in 2000 and 2002. R-M structures appear to develop in response to local ocean conditions, ice thickness, and calving history. Their evolution can, therefore, be an indicator of environmental change along the boundary between RIS, the Ross Sea, and the atmosphere, and of modes of frontal mass loss.

4.2 Introduction

The Antarctic Ice Sheet is losing net mass to the ocean. Between 1992 and 2017, the loss of ice from Antarctica contributed 7.6 $\pm$ 3.9 mm to global sea level (Shepherd et al., 2018), and the rate of this sea-level contribution accelerated from 2002 to 2017 (Nerem et al., 2018). This acceleration is largely controlled by the continent's floating ice shelves that, through contact with sidewalls and elevated seabed features, "buttress" the flow of upstream grounded glaciers and ice streams into the Southern Ocean (Thomas, 1979; Dupont and Alley, 2005). Antarctic ice shelves have experienced a net mass loss and thinning over the course of the satellite era due to excess basal melting (Pritchard et al., 2012; Paolo et al., 2015; Adusumilli et al., 2020), with the most rapid thinning occurring in the Amundsen Sea and Bellingshausen Sea sectors. Ice shelves have also lost volume through areal retreat or collapse, as on the Antarctic Peninsula (e.g., Scambos et al., 2004), and large calving events on other ice shelves (Greene et al., 2022). Both types of ice-shelf mass loss have resulted in reduced buttressing capacity, grounding-line retreat, and acceleration and thinning of the inland glaciers. Recent modeling work has shown that ice-shelf thinning can trigger observed grounded-ice discharge virtually instantaneously (Gudmundsson et al., 2019) and hundreds of kilometers away from the location of ice-shelf mass loss (Reese et al., 2018).

Averaged around the entire continent and over decades, ice-shelf mass loss is partitioned fairly evenly between iceberg production and basal melting (e.g., Rignot et al., 2013; Depoorter et al., 2013). About 90% of calving-driven mass loss occurs in the form of icebergs $>$100

km^2 in area (Tournadre et al., 2016; Greene et al., 2022). On the larger ice shelves that are currently close to being in steady state (Ross, Filchner-Ronne, and Amery), tabular calving events that occur every few decades due to rift propagation account for most mass loss (e.g., Lazzara et al., 2008; Greene et al., 2022; Walker et al., 2021). However, for specific ice shelves (e.g., Larsen B, Thwaites), production of numerous small icebergs of order 1 km^2 can still be dynamically significant and provide insights into the role of climate variability in significant mass-loss processes such as hydrofracture (Scambos et al., 2003) and changes in the strength of shear margins (e.g., MacGregor et al., 2012).

Our study area is Ross Ice Shelf (RIS), Antarctica's largest ice shelf by area ($\sim$480,000 km^2), which buttresses $\sim$11.6 m of potential globally averaged sea-level rise (Tinto et al., 2019). RIS experienced calving of seven large tabular icebergs in 2000 and 2002 (Figure 4.1a; Greene et al., 2022, their Figure 3). The massive B-15 contained about 2,700 km^3 of ice (Martin et al., 2007) and is the largest iceberg in the satellite record. Only a small ($\sim$40 km along front) portion of the RIS front, termed "Nascent Iceberg" by MacAyeal et al. (2006), has not calved in the 21st century, but it is expected to eventually do so along the same rift from which B-15 calved. These RIS calving events mostly removed "passive shelf ice" (Fürst et al., 2016; Greene et al., 2022), whose loss does not lead to significant speed-up of the upstream grounded ice.

The near-front cross-section of an ice shelf is typically depicted as roughly rectangular in shape, perhaps with some thinning toward the front attributed to "mode-3" basal melting (Jacobs et al., 1992) and strain rates. Becker et al. (2021) showed that this is an oversimplification for much of the RIS front. They observed pervasive "rampart-moat" (R-M; term from Scambos et al., 2005) structures (Figure 4.1b) in surface height profiles across the front using laser altimetry from NASA's Ice, Cloud, and land Elevation Satellite-2 (ICESat-2; 2018–present). The R-M morphology, marked by a depression (moat) inboard of a raised edge (rampart), forms in response to the development of an underwater bench of ice due to ocean-driven erosion of the ice front near the waterline and subsequent collapse of the aerial portion of the ice shelf. The internal

stress field associated with this flexure may induce calving of small icebergs along existing basal crevasses (Wagner et al., 2014; Mosbeux et al., 2020). Typical dimensions for R-M structures are height differences (dh_{RM}) between the rampart and moat of order 1–10 m and length scales (dx_{RM}) of hundreds of meters (Becker et al., 2021).

Although Becker et al. (2021) found R-M structures along most of the RIS front, they also reported a number of "berm" (also from Scambos et al., 2005) profiles (Figure 4.1c), whose monotonic lowering toward the front is more consistent with the classical depiction of an ice front. This shape arises from a downward bending moment generated by the difference in hydrostatic and ice lithostatic pressure gradients along the front face (Reeh, 1968; Mosbeux et al., 2020), increased strain rates, and near-front thinning by basal melting.

We expect that the small-scale structure of the ice front will evolve in time as environmental forcings change. For example, if the buoyancy of the submerged bench increases, the height difference between the rampart and moat will increase. If the rampart and part of the moat calve, the new front may lose its buoyant bench and R-M structure. Small-scale changes in the R-M characteristics observed by altimeters may, therefore, indicate variations in ocean state and provide information about the physical properties of the near-front ice shelf, including reduced strength due to crevasses. Information gained by studying R-M evolution on the slow-moving ice front could also provide critical insights into decay mechanisms for icebergs. Several studies have proposed (Scambos et al., 2005; Wagner et al., 2014) or modeled (England et al., 2020) R-M development as a mechanism for the breakup of tabular icebergs through repeated edge-parallel calving events, but rapid iceberg drift limits our ability to repeatedly observe R-M structures at iceberg margins.

In this work, we use satellite laser altimetry data (Section 4.3) from NASA's ICESat (2003–2009) and ICESat-2 (2018–present) missions to investigate the temporal variability of R-M structures along the RIS front. We first describe how we detect R-M structures in both data sets and the methods we apply to compare the two sets of R-M observations collected at

disparate resolutions (Section 4.4). We then report on the spatial distribution and evolution of R-M structures on RIS between 2003 and 2022 (Section 4.5). We discuss possible causes and implications of observed trends in buoyancy-driven flexure, how the phenomenon interacts with other ice-shelf processes, and how it might evolve under changing summertime sea ice and upper-ocean conditions (Section 4.6). These observations of buoyancy-driven flexure can inform ice-sheet models that rely on representations of mass-balance processes acting across a range of temporal and spatial scales to forecast ice-sheet and sea-level change.

4.3 Satellite data sets

We primarily used laser altimetry data from ICESat and ICESat-2 to assess R-M evolution along the RIS front. The long, continuous record of radar altimetry from the sequence of European Space Agency satellites (Abdalla et al., 2021) has insufficient horizontal resolution to resolve these R-M structures. We obtained additional glaciological context using satellite-derived ice-velocity products and visible and thermal imagery.

4.3.1 ICESat satellite laser altimetry (2003–2009)

ICESat (Schutz et al., 2005) operated between September 2003 and October 2009, completing 17 campaigns, each 33 days in duration, along approximately repeated ground tracks two or three times per year. Elevation data were acquired between 86°S and 86°N. The altimetry channel of the Geoscience Laser Altimeter System (GLAS) onboard ICESat transmitted pulses of near-infrared (1064 nm) light at 40 Hz. Each measurement provided the average elevation over a surface footprint with a diameter of $\sim$65 m, with successive footprints separated by $\sim$172 m in the along-track direction. The vertical precision of ICESat measurements over the entire Antarctic Ice Sheet, including those collected over areas with steep surface slopes, was about 0.15 m (Shuman et al., 2006). Ground tracks did not repeat precisely; typical track-to-track offsets were $\sim$150

m, and the horizontal locations of footprints were reported with ∼10 m accuracy (Smith et al., 2009). We used Version 34 of the L2 Global Antarctic and Greenland Ice Sheet Altimetry Data (GLAH12; Zwally et al., 2014), which have been corrected for the Gaussian–Centroid (or "G–C") offset identified by Borsa et al. (2014).

4.3.2 ICESat-2 satellite laser altimetry (2018–present)

ICESat-2 (Markus et al., 2017) was launched in September 2018, nearly a decade after the ICESat mission concluded. ICESat-2 collects data between 88°S and 88°N along each of 1,387 reference ground tracks (RGTs) every 91 days. At the time of writing, ICESat-2 had completed 18 full 91-day cycles and part of a 19th; over Antarctica, the altimeter pointed to its RGT for all but the first two cycles and three days of the third cycle. The Advanced Topographic Laser Altimeter System (ATLAS) onboard ICESat-2 transmits pulses of green (532 nm) light at 10 kHz. Each pulse is split into three pairs of beams separated by ∼3.3 km in the across-track direction; each beam pair comprises a strong and a weak beam nominally separated by ∼90 m. The high pulse repetition rate of ATLAS translates to an along-track spacing of ∼0.7 m on the surface for each of the six ground tracks (GTs). The footprints for each pulse are ∼10.6–12 m in diameter (Magruder et al., 2020).

We used Version 5 of the ICESat-2 L3A Land Ice Height product (ATL06; Smith et al., 2019; Smith et al., 2021), which provides estimated heights obtained from 50%-overlapping, 40-m-averaged along-track segments from the start of Cycle 1 (October 14, 2018) to partway through Cycle 17 (October 12, 2022). Brunt et al. (2019) determined that ATL06 data over flat parts of the Antarctic Ice Sheet have accuracies of 3 cm or better and precisions of 9 cm or better.

4.3.3 Ice-shelf velocities, imagery, and front positions

To assess ice-front change during the ICESat and ICESat-2 eras, we used a filled-in, extrapolated composite (Greene et al., 2022) of two ice-velocity products: Version 1 of the NASA Making Earth System data records for Use in Research Environments (MEaSUREs) ITS_LIVE mosaic (Gardner et al., 2022), and Version 2 of the MEaSUREs InSAR-Based Antarctica Ice Velocity Map (Rignot et al., 2011b, 2017; Mouginot et al., 2012, 2017). Our ICESat-2-based analyses required velocity data that extend to the maximum known RIS front positions in recent years. However, most available velocity products (including the time-averaged MEaSUREs InSAR-based map, which comprises data acquired between 1996 and 2016) are masked to earlier ice-front positions and coastlines (Greene et al., 2022). The extrapolation of such products beyond the associated mask can introduce bias in the velocities; Klein et al. (2020) reported that velocities derived from GPS stations near the 2015–2016 RIS front, which were located north of the MEaSUREs ice front, can be up to 90 m a^{-1} greater than the locally extrapolated time-averaged MEaSUREs values. Greene et al. (2022) mitigated the effects of this masking issue in the development of their composite by holding observed ice thickness and velocity values constant to extrapolate ice-flow direction beyond the ICESat-era ice extent, and then projecting ice speed along the extrapolated flow directions.

We used Moderate Resolution Imaging Spectroradiometer (MODIS) Corrected Reflectance and thermal imagery (downloaded from NASA Worldview and from Scambos et al. (2022), respectively) to locate the RIS front at various epochs during the ICESat and ICESat-2 eras and trace the approximate locations of tabular calving events from RIS in the early 2000s. The Corrected Reflectance images are only available during daylight hours and without significant cloud cover, and they are posted on NASA Worldview at 250 m spatial resolution. Scambos et al. (2022) processed the 1 km MODIS channel-32 thermal images during austral winter to preserve an accurate approximate skin temperature; they also selected scenes that showed minimal cloud cover.

We also employed two published RIS front positions to guide the location of the front in individual ICESat and ICESat-2 profiles. For the ICESat era, we used the front position from Depoorter et al. (2013), which is similar to the Mosaic of Antarctica front based on MODIS imagery from summer 2003–2004 (Haran et al., 2005; Scambos et al., 2007). For the ICESat-2 era, we used the 2018 front position from Baumhoer et al. (2021).

4.4 Methods

We first describe the selection and correction of elevation profiles, and characterization of ice front shape, for ground tracks from ICESat (subsection 4.4.1) and ICESat-2 (subsection 4.4.2). We then describe evaluation of trends in R-M characteristics from four years of ICESat-2 data, and between the ICESat and ICESat-2 data collection periods (subsection 4.4.3). Finally, we explain how we used ice velocities and imagery-derived front positions to search for evidence of small-scale calving during the ICESat and ICESat-2 eras (subsection 4.4.4).

4.4.1 ICESat front-shape analysis

Profile selection

We downloaded all available ICESat Version 34 GLAH12 elevation data from the National Snow and Ice Data Center. We applied the built-in value for the elevation correction due to waveform saturation and converted to the WGS84 elevation (h_{WGS84}) using the built-in value of the offset between the TOPEX/Poseidon and the WGS84 reference ellipsoids. To assess cloud cover at the time of acquisition, which is known to attenuate laser return energy, we extracted the corresponding gain values for the received pulses (given by the parameter '*i_gval_rcv*').

We identified 1,009 profiles along 118 distinct ICESat ground tracks that showed a transition between ocean and ice shelf within 10 km of the Depoorter et al. (2013) RIS front position. We then applied geophysical corrections to calculate the height relative to the instantaneous sea

surface (h_{ss}), as follows:

$$h_{ss} = h_{WGS84} - h_{geoid} - h_{ot} - h_{lt} - h_{dac} - h_{mdt}, \tag{4.1}$$

where h_{geoid} is the height of the EGM2008 geoid above the reference ellipsoid; h_{ot} is the ocean tide elevation; h_{lt} is the ocean load tide elevation; h_{dac} is the MOG2D Dynamic Atmospheric Correction for height changes due to atmospheric forcings (produced by CLS using the model from LEGOS and distributed by AVISO+, with support from CNES); and h_{mdt} is the mean dynamic topography, or the height of the time-averaged sea surface relative to the geoid.

We removed the values of h_{ot} and h_{lt} that had already been applied to the data and replaced them with outputs from the CATS2008 circum-Antarctic ocean tide model (Howard et al., 2019; an update to the model described by Padman et al., 2002) and the TPXO7.2 tide model (Egbert and Erofeeva, 2002), respectively. For h_{mdt}, we applied a constant value of –1.4 m (Andersen et al., 2015). We also removed outliers ($h_{ss} < -5$ m or $h_{ss} > 100$ m, as used by Becker et al. (2021)) and converted the footprint locations into along-track coordinates.

In each of the 1,009 profiles, we searched for the ice front using a front-jump detection algorithm similar to that described by Becker et al. (2021) for finding the front in ICESat-2 data. We used the front position from Depoorter et al. (2013) to guide the algorithm. Given the much coarser spatial resolution of ICESat measurements relative to ICESat-2, we changed the maximum along-track distance over which a front jump could occur from 80 m to 400 m. We maintained all other thresholds from Becker et al. (2021).

We excluded one profile (the L3K repeat along Track 0044) near Nascent Iceberg for which there were no data across the true front. Three times, the algorithm located the front north of the true ice front, presumably on iceberg margins; in these cases, we re-ran the front detection algorithm or manually updated the true front location. Including these three examples, our algorithm detected the front in 807 of the 1,009 ICESat profiles crossing the RIS front. We

suspect that cloud cover played a role in the algorithm's inability to detect the front in the 202 remaining front crossings, as all profiles showed received-pulse gain values above GLAS' preset lowest value of 13 (Fricker and Padman, 2006). For 164 of the front crossings, the gain exceeded 13 for more than half of the shots within the profile.

The angle at which a height profile crosses the ice front can affect the interpretation of the front shape. Submerged benches that generate R-M structures form in response to elevated melting along the ice front, and we assume that the resulting bending occurs normal to the portion of the front experiencing melting. Under this assumption, profiles that crossed the front at steep angles may identify ramparts and moats that arise due to melting from different sections of the front. To account for this offset, we computed the angle between each ICESat profile in which the true ice front was detected and the local ice front, which we approximated from the Depoorter et al. (2013) front. We limited our front-shape analysis to profiles that sampled the front at angles less than or equal to $\pm 30^{\circ}$ from normal. Of the 807 front crossings in which our algorithm successfully detected the front, 619 intersected the front at angles less than or equal to $\pm 30^{\circ}$ from normal. About 30% (56) of the 188 profiles that did not meet this requirement sampled the front north or east of Roosevelt Island (i.e., east of –321 km easting on Figure 4.1a). The front was sufficiently smooth east of $\sim$–409 km easting for our algorithm to discern the front shape along well-aligned tracks. However, the oblique track orientation and extensive crevassing between $\sim$–409 km and –321 km easting led us to exclude from the front-shape analysis the 85 profiles (54 of which met the $\pm 30^{\circ}$ criterion) that crossed that portion of the front. For each of the remaining 565 well-aligned ICESat profiles (along 89 distinct tracks) in which we detected a RIS front crossing, we used the detected front position and the angle between the profile and the local front to reproject the height data along a line normal to the ice front, thereby converting the along-track distances to distances with respect to the front.

Characterization of front shape

We followed Becker et al. (2021) in searching for the moat, or the minimum height value (h_M) in the first detected depression within 2 km (in reprojected coordinates) of the detected front. Once the algorithm detected a moat, we instructed it to search for the maximum height between the detected front and the deepest point within the moat; we identified this point as the rampart, with associated height h_R. This is a modification from how Becker et al. (2021) identified h_R in the higher-resolution ICESat-2 GT profiles, as the highest ATL06 value within 100 m of the front. We then computed the difference in height, dh_{RM}, and the Euclidean distance, dx_{RM}, between the rampart and the deepest point within the moat (Figure 4.1b) for all profiles with detected moats. This is the same definition of dh_{RM} as applied by Becker et al. (2021) for ICESat-2 data. For the ICESat dx_{RM} calculation, however, we used the Euclidean distance between the rampart and moat positions within the rotated profiles instead of the along-track distance (as Becker et al., 2021, used for the ICESat-2 data), because ICESat tracks generally crossed the RIS front at more oblique angles than ICESat-2 tracks.

We sorted the ICESat-derived values of dh_{RM} and dx_{RM} into six regions along the RIS front (Figure 4.2a), delineated to roughly match the boundaries of recent large calving events (Figure 4.1a; Horgan et al., 2011) and major streakline locations. These regions approximately correspond to regions 1 and 3–7 from Becker et al. (2021); we eliminated their Region 2 in this study because of the generally oblique orientation of ICESat tracks and topographic complexity near this section of the front.

4.4.2 ICESat-2 front-shape analysis

We followed the methods outlined in Becker et al. (2021) for detecting the RIS front and R-M structures in ICESat-2 ATL06 strong-beam data, with three key modifications to the front detection portion:

(i) We required that all possible front detections be within 10 km of the 2018 front position from Baumhoer et al. (2021). This step increased the likelihood that the algorithm would detect the true front in GT profiles that also sampled icebergs in the Ross Sea. It also helped the algorithm avoid interpreting upstream rifts as the front when clouds affected returns over the true ice front.

(ii) We increased the maximum length of GT along which the minimum height increase (10 m) for a potential front jump could occur, from two footprints to four. This addressed cases where the front was not detected due to a profile including one or two footprints along the front face.

(iii) We steered the algorithm away from misidentifying the margins of <10-km-wide near-front icebergs as the front by instructing it to ignore possible front locations downstream of ATL06 segments with $h_{ss} < 2$ m (i.e., those over the ocean surface or sea ice).

We note that, prior to running the ICESat-2 GT profile data through the front and R-M detection algorithms, we applied the ATL06-provided corrections for h_{ot} to the ICESat-2 ellipsoidal heights and maintained the already-applied h_{lt} corrections; the values for both of these corrections came from the GOT4.8 model. This is in contrast to our decision to replace the corrections for h_{ot} and h_{lt} that had already been applied to the ICESat data with CATS2008 and TPXO7.2 outputs.

As Becker et al. (2021) noted, many of the ICESat-2 RGTs are close to orthogonal to the RIS front; therefore, we did not reproject the associated height data. However, we did calculate the angle between each GT profile in which the true RIS front was detected and the local velocity vector, derived from the composite of the ITS_LIVE and MEaSUREs InSAR-based velocity data (Greene et al., 2022), to support our analysis of changes in R-M structures through time. Most GT profiles were within 20° of parallel to the velocities, but the majority of the GT profiles in the region east of Roosevelt Island (Region 2 from Becker et al., 2021) intersected the local velocity

vectors at angles greater than 30°. To be consistent with our decision to exclude ICESat-derived R-M characteristics from their Region 2, we did not consider ICESat-2-derived values of dh_{RM} and dx_{RM} from this region. Thus, for both missions, we only assessed R-M characteristics along the remaining six regions of the RIS front from Becker et al. (2021).

The modified version of the Becker et al. (2021) algorithm successfully detected the front along 5,974 of the 11,262 strong-beam GT profiles that sampled the RIS front between Marie Byrd Land and Ross Island on or before October 12, 2022. We attributed 4,425 of the failed front detections to the presence of clouds (determined using the ATL06 *cloud_flg_atm* parameter, as in Becker et al., 2021) and the remaining 863 to algorithm failure. In 5,375 GT profiles, the algorithm located the front within one of the six regions described in subsection 4.4.1. We manually removed eight additional GT profiles for which the algorithm located the front in the heavily rifted region seaward of Roosevelt Island or on rifts upstream of the true ice front.

4.4.3 Changes in regional R-M characteristics during the ICESat-2 era and between the ICESat and ICESat-2 eras

ICESat-2 (2018–2022)

For each of the six regions of the ice front (Figure 4.2a), we sorted all values of dh_{RM} and dx_{RM} from ICESat-2 data into four time periods: cycles 1–4 (October 2018–September 2019); 5–8 (September 2019–September 2020); 9–12 (September 2020–September 2021); and 13–17 (September 2021–October 2022). We computed histograms and mean values of the two parameters for each epoch and for each region, then combined data into the eastern front (regions 1–3), the western front (regions 4–6), and the entire front (regions 1–6).

We assessed the temporal trends in observed mean dh_{RM} and dx_{RM} for each section of the front. To evaluate the associated uncertainties, we applied a bootstrap approach to determine the statistical significance of the observed trends; that is, we compared them with simulated

trends driven by sampling error alone. This involved, for a given section of the front and R-M characteristic, randomly resampling (with replacement) 25% of the observations of dh_{RM} and dx_{RM} four separate times, taking each sample as representative of a single ∼year-long epoch. We performed this resampling n = 10,000 times, yielding 40,000 year-long samples. We calculated the mean of each sample and the trend across the four sample means to ensure robust distributions of possible trends in average dh_{RM} and dx_{RM} for each region.

The almost exact repetition of the ICESat-2 GTs allowed us to also explore the temporal evolution of dh_{RM} and dx_{RM} in individual R-M structures within our six regions. We searched for evidence of R-M change along strong-beam GT profiles that repeated at least twice between April 1, 2019, when ATLAS began pointing at its RGT, and October 12, 2022. We limited this analysis to GT profiles that were consistently within 5° of the local velocity vector so that we could be confident that we were examining the same piece of ice as the ice front advanced.

ICESat era vs. ICESat-2 era

The availability of ICESat and ICESat-2 observations across the RIS front presents an opportunity to compare R-M structures and their characteristics between the two mission periods. However, such a comparison is complicated by differences in GLAS and ATLAS sampling and along-track resolution (see inset in Figure 4.2a), which could be mistaken for actual changes in R-M characteristics through time. We developed a strategy, based on Monte Carlo methods, to evaluate whether there are statistically significant differences between ICESat and ICESat-2 R-M characteristics. The approach is detailed in the Appendix.

4.4.4 Comparison of observed and expected RIS front advance

In the absence of calving, an ice front advances at the same rate as the near-front ice velocity. If calving occurs, the ice-front advance rate is less than the ice velocity. Comparison of observed ice advance rate relative to measured ice velocity can reveal small-scale calving events

that occur when imagery is not available. To test this, and to identify regions of the RIS front that may have experienced this form of calving during the ICESat era, we advected the late-2003 RIS front position, traced from MODIS satellite imagery, seaward to its expected late-2009 position. For the ICESat-2 era, we advected the late-2018 position to its expected late-2022 position. We used velocity components from the composite of ITS_LIVE and MEaSUREs InSAR-based velocity data for both advection calculations. For both epochs, we compared the expected front position with the front position in contemporaneous MODIS satellite images.

4.5 Results

4.5.1 Spatial distribution of R-M characteristics

ICESat

Our ICESat R-M detection algorithm initially showed R-M structures in 448 of the 565 crossings of the RIS front selected (subsection 4.4.1). However, we discarded 14 profiles that crossed the front downstream of the rifts centered at ∼100 km easting or that showed poor data quality near the front; both of these issues precluded accurate determination of the front shape. Thus, we detected R-M structures in 434 (∼77%) of the 565 well-aligned ICESat front-crossing profiles; the remaining 131 (∼23%) either show berm structures near the front or contain insufficient information to characterize the front shape.

The ICESat-derived values of dh_{RM}, evaluated for each of the 434 profiles selected as described in subsection 4.4.1, range from just above 0 m to 4.78 m with a mean of 0.77 m; those of dx_{RM} range from 168 m to 1190 m with a mean of 386 m. The distributions of both parameters generally have similar shapes along the front and are, for the most part, unimodal (Figures 4.2b–4.2c). Most dh_{RM} values, and the average value for all six regions, are less than 1 m. Average dh_{RM} is highest in Region 2 (0.95 m) and lowest in Region 6 (0.53 m). The regional

mean values of dx_{RM} range from 277 m (Region 4) to 437 m (Region 2). On average, both dh_{RM} and dx_{RM} are larger on the eastern portion of the front (regions 1–3; 0.88 m and 404 m, respectively) than on the western portion of the front (regions 4–6; 0.61 m and 359 m). We note, however, that ICESat undersamples R-M structures (inset in Figure 4.2a; see Appendix below).

ICESat-2

We assessed R-M development along 5,367 strong-beam GT profiles along 218 RGTs that satisfied all of the requirements described in subsection 4.4.2. We report a similar partition in R-M vs. berm structures as in the ICESat data: 4,193 ($\sim$78%) of these GT profiles show R-M structures, and 1,174 ($\sim$22%) show berm structures or contain insufficient information to determine the front shape. This result is also consistent with that of Becker et al. (2021), who found R-M structures (berm structures) along $\sim$74% ($\sim$26%) of the RIS-front-crossing GT profiles acquired between October 2018 and July 2020.

We found significant spatial variability of dh_{RM} and dx_{RM} along the RIS front, with front-wide averages of 5.7 ± 0.1 m and 304 ± 2 m, respectively (Figures 4.2b–4.2c; Table 4.1). Uncertainties in these and the following mean values represent the standard error. Mean dh_{RM} is largest in Region 1 (11.7 ± 0.2 m) and smallest in Region 4 (3.4 ± 0.1 m). R-M structures in Region 4 also show the smallest average value of dx_{RM} (183 ± 3 m) and those in Region 2 the largest (451 ± 5 m). As for ICESat, both dh_{RM} and dx_{RM} tend to be larger on the eastern portion of the front (mean values of 7.2 ± 0.1 m and 383 ± 3 m, respectively) than on the western portion of the front (mean values of 4.5 ± 0.1 m and 233 ± 2 m). Indeed, all but one of the GT profiles for which $dh_{\mathrm{RM}} > 15$ m ($n = 41$) crossed the front in regions 1 and 3; the one crossed the front in Region 6. We also observed differences in the shapes of the regional histograms. Whereas the distributions of dh_{RM} for regions 1 and 2 and of dx_{RM} for all regions and the full front have single peaks, those of dh_{RM} for regions 3–6 and the full front are bimodal. The peaks in all five of these bimodal distributions occur at roughly the same values of dh_{RM}: $\sim$2 m and $\sim$7–8 m.

4.5.2 Intra- and intermission changes in regional R-M characteristics

We first consider temporal changes in R-M characteristics for the period 2018–2022, during which R-M structures were well resolved by ATLAS on ICESat-2. We then report the differences between R-M characteristics estimated from ICESat data for 2003–2009 and those based on ICESat-2 data.

ICESat-2-era (2018–2022) temporal variability

We calculated the distributions of dh_{RM}, for the full ice front and by region, for four roughly annual periods from late 2018 to late 2022 (Figure 4.3a). The average value of dh_{RM} for each of these distributions (Figure 4.3b) indicates regional variations in the four-year trends, although these are only statistically significant for a few regions (Table 4.1).

Our analyses of temporal changes in bulk regional R-M characteristics (described in subsection 4.4.3) indicate that dh_{RM}, using data for the full RIS front, increased between October 2018 and October 2022. This manifested in both changes in the shape of the roughly annual dh_{RM} histograms (Figure 4.3a, leftmost column) and the trend in their mean values (Figure 4.3b; Table 4.1). This trend exceeds the 95th percentile of the distribution of simulated trends in mean dh_{RM} (Figure 4.S1, leftmost column). We also found a statistically significant positive trend in mean dh_{RM} for the eastern section of the front (Figure 4.S1, center and rightmost columns) but an insignificant trend on the western section. This contrast held for the six regions making up the two sections of the front. Mean dh_{RM} increased monotonically through time in regions 1–3, and this trend was statistically significant in all three regions (Figure 4.S2). On the western front, average dh_{RM} increased monotonically and significantly only in Region 5. Region 6 showed a net 0.1 ± 0.4 m decrease, and an insignificant trend, in average dh_{RM} over the ICESat-2 period, with a 0.9 ± 0.4 m decrease between cycles 9–12 and 13–17 (Table 4.1). Region 4 (which includes Nascent Iceberg), which had the lowest mean values of dh_{RM} and dx_{RM} of all six regions during all four $\sim$year-long periods, was the only portion of the front to show a significant negative trend

in mean dh_{RM}. Region 6 was the only western-front region to exhibit larger average dh_{RM} values than an eastern-front region (Region 3); this was the case throughout the ICESat-2 record.

Both the eastern and western sections of the RIS front showed a decrease in mean dx_{RM}, but as the trend values fell between the 5th and 95th percentiles of the corresponding distributions of possible trends, we do not consider the trend to be statistically significant (Figure 4.S1). Mean dx_{RM} decreased through time in regions 1, 3, 4, and 6 and increased through time in regions 2 and 5 (Figure 4.3c; Table 4.1). The trends were significant for regions 1, 4, 5, and 6 (Figure 4.S2). For all four periods, all eastern-front regions exhibited greater average dx_{RM} values than all western-front regions.

A shorter version of our ICESat-2 data set (with data through mid-2022) includes 304 sets of strong-beam GT profiles that (1) sampled a segment of the RIS front within one of our six regions at least twice along the planned RGTs and (2) were within 5° of the local ice velocity vector. These repeating sets consist of a total of 1,075 GT profiles. A majority of the sets (173, or $\sim$57%) crossed the front in one of the western-front regions, with just four ($\sim$1%) crossing the front in Region 2 and none crossing the front in Region 1. The repeating GT profiles revealed several distinct modes of R-M temporal evolution over the ICESat-2 record, including monotonic increases in dh_{RM} (Figure 4.4b); both rapid and sustained decreases in dh_{RM} (Figures 4.4c–4.4e); and recovery of dh_{RM} after a decrease (Figures 4.4c–4.4e). (We note that we cannot rule out the possibility of higher-frequency changes in dh_{RM} and dx_{RM} for the time series shown in Figure 4.4.) These examples also illustrate the variability in R-M structure morphology and typical values of dh_{RM} and dx_{RM} on the RIS front. Our repeat-profile analysis did not yield any direct evidence of R-M-driven calving.

We considered the potential for seasonal differences in the evolution of individual R-M structures using repeated GT profiles from consecutive cycles. We found 307 pairs of consecutive-cycle repeats that sampled the front in approximately the same location; 172 showed an increase in dh_{RM} and 135 a decrease. Our data set included instances of dh_{RM} increasing and decreasing

for the four possible seasonal transitions: winter to spring; spring to summer; summer to fall; and fall to winter. However, pairs for which the first repeat occurred in the fall and the second in the winter accounted for the largest fraction (∼32%, or 55) of the pairs that showed an increase in dh_{RM}. Consecutive repeats in the summer and fall made up the largest fraction (∼32%, or 43) of decreasing-dh_{RM} pairs.

Changes in R-M structures from the ICESat to ICESat-2 eras

Comparisons between R-M characteristics obtained from ICESat and ICESat-2 along-track data requires careful treatment of the two data sets (subsection 4.4.3). The along-track location of the downsampled ICESat-2 shots—that is, of the center of the bins across which we averaged the ATL06 segment heights—had a significant impact on the synthetic profiles' ability to capture the full R-M structure resolved with ATL06 and the resulting values of dh_{RM} and dx_{RM} (Figure 4.5). For some bin-center offset values, the "rampart" in the corresponding synthetic ICESat profile was located on what would have been the front face (bottom profile in Figure 4.5), which would have resulted in a berm front-shape determination (with dh_{RM} = 0 m and dx_{RM} = 0 m). For others, ICESat would have been able to resolve most of the topography associated with the R-M structure. The synthetic ICESat profiles indicate that GLAS would not have been able to consistently reproduce the sharp ramparts shown in the ATL06 profiles (Figure 4.4). Unless it happened to sample the rampart at its seaward edge, GLAS would have instead illuminated a more rounded rampart with a maximum height 10s or even 100s of m inboard of the front (see, e.g., Figure 4.6c).

To show the influence of variable bin-center location, we report all 86 possible ICESat-derived values of dh_{RM} and dx_{RM} for each ICESat-2 R-M structure case study (distributions in insets in Figures 4.6 and 4.S3–4.S9). For all 10 case studies, the maximum possible value of dh_{RM} fell short of the ICESat-2-derived value, but the 172 m spacing of the synthetic ICESat profiles meant that this was not always true for dx_{RM}. Indeed, for six case studies, the maximum

possible ICESat-derived value of dx_{RM} exceeded the ICESat-2-derived value.

The synthetic ICESat–ICESat-2 scale factors, which we computed using the median values of the possible ICESat distributions, ranged from zero to 0.81 for dh_{RM} and from zero to 1.02 for dx_{RM}. Considered together, the median synthetic ICESat dh_{RM} and dx_{RM} values were closest to the ATL06-derived "truth" for the low dh_{RM}, high dx_{RM}, case study (Figure 4.S4), for which we calculated scale factors of 0.81 for dh_{RM} and 0.84 for dx_{RM}. The scale factors suggest that, generally speaking, the synthetic ICESat profiles can better describe an R-M structure with intermediate or high dx_{RM} (i.e., $dx_{RM} \geq 344$ m). The high dh_{RM}, low dx_{RM}, case study is somewhat of an exception to this, however, with dh_{RM} (dx_{RM}) scale factors of 0.36 (1.02) (Figure 4.S8). For the any dh_{RM}, very low dx_{RM} ($<$172 m), case study, the R-M structure was too narrow (i.e., the "true" value of dx_{RM} was too small) for it to be detected in most of the 86 synthetic ICESat profiles, leading to median values and scale factors of zero for both dh_{RM} and dx_{RM} (Figure 4.6a). Thus, we infer that ICESat would not be able to resolve an R-M structure with dx_{RM} smaller than the approximate ICESat shot spacing.

We now turn to the Monte Carlo simulations, in which we applied the category-specific scale factors to the resampled ICESat-2 dh_{RM}–dx_{RM} pairs to convert them into synthetic ICESat dh_{RM}–dx_{RM} pairs. Across the entire front, this conversion resulted in 10,668 zero-valued synthetic ICESat dh_{RM}–dx_{RM} pairs; we therefore only included 49,332 pairs in our results (Table 4.2). We kept less than half of the Region 4 pairs on this basis. Although we investigated the regional evolution of dh_{RM} and dx_{RM} between the ICESat and ICESat-2 periods, we focused mostly on changes in dh_{RM}. Most of the R-M structures resolved by ICESat-2 are less than 600 m in dx_{RM} (Figure 4.2c), or about 3.5 times the ICESat shot spacing. ICESat can yield a fairly continuous range of dh_{RM} values in spite of this coarse sampling but only discrete estimates for dx_{RM} separated by $\sim$172 m (insets in Figures 4.6 and 4.S3–4.S9); we are therefore more confident in the accuracy of the synthetic ICESat dh_{RM} values than in that of the synthetic ICESat dx_{RM} values.

For dh_{RM}, we found the greatest difference between the observed and synthetic ICESat distributions for regions 1 and 2 (Figure 4.7). For Region 1, there is minimal overlap between the upper whisker (which extends to 1.5 times the interquartile range (IQR)) of the observed ICESat distribution and the lower whisker of the synthetic ICESat distribution; for Region 2, the lower whisker of the synthetic ICESat distribution extends over the full range of the observed ICESat distribution, but the bulk of the synthetic ICESat distribution exceeds the upper whisker of the observed ICESat distribution. Overall, the shapes and descriptive statistics (Table 4.2) of the observed and synthetic distributions for these two regions are sufficiently different for us to reject the null hypothesis that bulk dh_{RM} did not change between the ICESat and ICESat-2 eras.

The synthetic ICESat dh_{RM} density histograms for the four remaining regions are bimodal and all have primary peaks at $dh_{\mathrm{RM}} \approx 1$ m—roughly where the observed ICESat peaks occur—and secondary peaks at $dh_{\mathrm{RM}} \approx 3$–5 m. For regions 3 and 6, the secondary peaks are sufficient for the synthetic ICESat medians to exceed the observed ICESat medians by more than 2 m. We conclude that R-M structures sampled by ICESat-2 in these two regions showed a larger range of dh_{RM} values, and higher values on average, than those sampled directly by ICESat. We found the least convincing evidence for bulk dh_{RM} increase for regions 4 and 5. For Region 5, the synthetic ICESat median is only 0.33 m higher than the observed ICESat median. For Region 4, the synthetic ICESat median is 0.22 m lower than its observed ICESat counterpart, although its mean and IQR are larger. There is also the most overlap between the observed ICESat-2 density histogram and the two ICESat density histograms for this region.

It was less straightforward to identify changes in dx_{RM} between the ICESat and ICESat-2 periods (Figure 4.S10; Table 4.2). For regions 1 and 4, the median of the synthetic ICESat distribution was greater than that of the observed ICESat distribution (but only just so for Region 4). For the other four regions, the observed ICESat median was considerably higher than the synthetic ICESat median. Across the front, the IQRs of the synthetic ICESat dx_{RM} data sets are smaller than those of the observed ICESat data sets, which suggests that the synthetic ICESat

data are more clustered than the observed ICESat data. This is opposite from the trend in the dh_{RM} data sets.

4.5.3 Observed vs. expected RIS front advance

The observed and predicted late-ICESat (2009; Figure 4.8a) and recent-ICESat-2 (2022; Figure 4.8b) front positions are generally in agreement. Major exceptions to this pattern, where the predicted advance exceeded the observed advance, include the crevassed and rifted region seaward of Roosevelt Island (for both ICESat and ICESat-2) and a notch in the front ∼20 km east of the easternmost tip of Ross Island (for ICESat). For each mission period, we identified two other locations where this mismatch is less pronounced but points to the possible influence of small-scale calving, particularly when considered with the annual evolution of both the local front shape (highlighted in the insets in Figures 4.8a–4.8b) and the northing of the front position (Figures 4.8c–4.8f) during late fall and early summer.

Our analysis revealed two examples of ice-front retreat and readvance during the ICESat era: at (1) ∼–175 km easting (Figure 4.8a, left inset, and Figure 4.8c) and (2) ∼160 km easting (Figure 4.8a, right inset, and Figure 4.8d). In the case of the former, the loss of ice associated with the ∼0.25 km retreat between 2005 and 2006 was more than recouped by 2007, after which the front advanced at a rate of ∼1 km a^{-1} (which is comparable to the observed velocities in this region). At ∼160 km easting, the front stepped back ∼0.5 km between 2004 and 2005 and then readvanced at a somewhat inconsistent rate until 2009. We also note the scalloped pattern of the local front in this region, which was especially evident in 2003. For both examples, the front did not reach our 2009 predicted position before the end of the ICESat mission; this discrepancy extends several km east and west from our selected transect locations.

We also observed an ICESat-2-era example of ice-front retreat and readvance, at ∼90 km easting (Figure 4.8b, right inset, and Figure 4.8f). In this location, the front retreated ∼0.7 km between 2019 and 2020 and then readvanced ∼4 km by late 2022. The ∼2 km a^{-1} local advance

rate meant that the 2022 front surpassed our predicted 2022 position, in spite of the retreat. At ∼–465 km easting (Figure 4.8b, left inset, and Figure 4.8e), we observed two instances of ∼0.1 km retreat separated by a two-year period of ∼0.4 km a^{-1} advance; the observed 2022 front fell short of the predicted front at this location.

4.6 Discussion

4.6.1 Implications of observed trends in R-M characteristics for bench dynamics

Becker et al. (2021) reported higher average values of dh_{RM} and dx_{RM} on the eastern section of the RIS front for the early ICESat-2 period (October 2018–July 2020). In this study, we analyzed R-M structures along 4,477 additional GT profiles—some from the early ICESat-2 period, which we were able to include here due to algorithm improvements, but most from mid-July 2020 to mid-October 2022. We found a similar divide between the eastern and western sections of the front for the four-year ICESat-2 record and the ICESat (2003–2009) record. The longer ICESat-2 record also allowed us to explore the temporal evolution of the regional R-M characteristics. Considering the two ICESat-2 data sets (the one presented in Becker et al. (2021) and the one presented here), average dh_{RM} for the full RIS front increased by 0.3 m with the inclusion of the GT profiles from mid-July 2020 to mid-October 2022, and average dx_{RM} increased by 1 m (Table 4.1 vs. inset table in Figure 3 of Becker et al., 2021). This is an imperfect comparison, however, as we did not include values of dh_{RM} and dx_{RM} from their Region 2 in our analysis. For all but one of the six regions included in both this work and Becker et al. (2021), mean dh_{RM} was higher for the longer ICESat-2 record. The exception was our Region 4 (their Region 5), which saw a ∼0.5 m decrease in mean dh_{RM}. The differences in mean dx_{RM} did not form as clear of a pattern; this parameter decreased in regions 1 and 4 but increased in regions 2,

3, 5, and 6. The refinement of the front and R-M detection algorithm and addition of more recent GT profiles did not significantly change the shapes of the regional dh_{RM} and dx_{RM} distributions (Figures 4.2b–4.2c vs. Figure 2b of Becker et al., 2021); in both studies, the histograms of all regional parameters are unimodal, save for the bimodal histograms of dh_{RM} for regions 3–6. Except for in Region 4, the dh_{RM} distributions in these four regions shifted toward the higher of the two peaks, which is consistent with our observation of mean values exceeding those observed by Becker et al. (2021) and ICESat-2 trends in mean dh_{RM} during the ICESat-2 period (Figure 4.3b; Table 4.1; Figure 4.S1).

Our results suggest that R-M structures on the RIS front have generally increased in height over the course of the ICESat-2 period and, along at least regions 1 and 2, since the ICESat era. We assume that the topography of a given R-M structure, and thus its value of dh_{RM}, arises from a combination of the upward bending moment associated with the submerged bench and the downward bending moment associated with the local pressure gradients along the front face. An increase in bulk dh_{RM} along these segments of the front and over these time periods implies that the upward bending moments have increased due to bench growth. Conversely, where and when dh_{RM} has decreased, e.g., in Region 4 over the ICESat-2 period and possibly between the ICESat and ICESat-2 eras, we expect that bench length and volume have decreased. Becker et al. (2021) hypothesized that dx_{RM} also scales with bench volume, but we report statistically insignificant trends in mean dx_{RM} for the eastern and western sections of the RIS front and the full front during the ICESat-2 period and statistically significant negative trends for regions 1, 4, and 6. The only statistically significant increase in dx_{RM} occurred in Region 5.

Mosbeux et al. (2020) applied both viscous and elastic frameworks to simulate the equilibrium surface deformations caused by benches with lengths between 0 and 100 m. The maximum values of dh_{RM} that we report from ICESat-2 data ($\sim$15 m) are just below their simulated values for 75 m benches for the viscous and 1-D elastic cases (16.45 m and 16.33 m; their Table 1) and for 100 m benches for the 2-D elastic case (15.61 m). (For the elastic cases, the

authors had to set the Young's modulus value to 10 MPa to obtain similar deformations as those produced in the viscous simulations.) Mosbeux et al. (2020) used a 200 m thick ice shelf in their simulations, but Becker et al. (2021) determined that the early-ICESat-2-era RIS is, on average, 241 m thick 3 km upstream of the front. We expect that a bench of a certain length would bend the thicker RIS front more than it would the thinner idealized ice shelf. Keeping this in mind, as well as the fact that ice exhibits elastic, viscous, and plastic deformation, we hypothesize that RIS bench length ranged from 0 to ∼65 m during the ICESat-2 era. For those sections of the front with significant positive trends in dh_{RM} during the ICESat-2 era (i.e., regions 1, 2, 3, and 5), we also extended the growth rates back in time to approximate when mean dh_{RM} and bench length would have been zero: midway through 2001 for Region 1; late 2008 for Region 2; early 1996 for Region 3; and late 1999 for Region 5.

Although Mosbeux et al. (2020) did not simulate the evolution of dx_{RM}, they did document the evolution of another across-front distance: the position of maximum longitudinal deviatoric stress (x*). They hypothesized that this parameter is the leading control on the size of bench-driven calving events. For both the viscous and 2-D elastic frameworks, Mosbeux et al. (2020) found that x* is inversely proportional to bench length, that is, it is closer to the front for longer benches. In the viscous case, where the R-M profile is allowed to develop until the system reaches hydrostatic equilibrium, x* is mostly a function of bench length and decreases with time. In the elastic case, it is mostly driven by the Young's modulus and approaches a minimum value of 186 m (for a Poisson's ratio value of 0.3) from the front in the limit of high bench length. These results suggest a tenuous inverse relationship between bench length and x* for a viscoelastic ice shelf, with a possible lower limit of x*. Assuming that x* is related to dx_{RM}, this supports our observations of negative trends in dx_{RM} during the ICESat-2 period, but it does not address why dh_{RM} and dx_{RM} both decreased in Region 4 and both increased in Region 5.

4.6.2 Environmental drivers of observed trends in R-M characteristics

We now examine potential drivers of the spatial variability in R-M characteristics along the RIS front during the ICESat and ICESat-2 periods, starting with why dh_{RM} and dx_{RM} tend to be larger on the eastern front than on the western front. As described above, we reason that dh_{RM} is controlled by bench volume, which could be higher on the eastern front due to thicker near-front ice or higher average bench length. Becker et al. (2021) argued that the fact that near-front ice is thicker on the eastern RIS—due to both the thickness of the upstream grounded ice and local basal melting—was at least partly responsible for their observations of higher dh_{RM} (and dx_{RM}) on the eastern portion of the front. Our "snapshot" ICESat and ICESat-2 results do little to refute this hypothesis, with both data sets showing higher average dh_{RM} and dx_{RM} on the eastern front. We also considered whether changes in near-front total ice thickness, which include changes in firn-air column thickness, between the two eras (Figure 4.9; data from Smith, Fricker, Gardner, Medley, et al., 2020) might translate to intermission differences in regional R-M characteristics. The Smith, Fricker, Gardner, Medley, et al. (2020) results show more locations of negative thickness change rates on the eastern portion of the front, with at least one area of thinning upstream of each of regions 1–3, than on the western portion of the front. Indeed, the areas just upstream of regions 4 and 5 of the front experienced a fairly strong thickening trend. Taken in isolation, these spatial patterns suggest that the geometry of the eastern (western) section of the front became less (more) conducive for R-M growth between the ICESat and ICESat-2 eras. This is inconsistent with the results of our Monte Carlo simulations, in which regions 4 and 5 show the least evidence for dh_{RM} increase between the two missions. However, these thickness-change rates and the associated cumulative thickness changes are small, especially in comparison to those observed on other Antarctic ice shelves, which suggests that ice thickness is not the only factor at play.

We now examine potential drivers of the spatial variability in R-M characteristics along the RIS front during the ICESat and ICESat-2 periods, starting with why dh_{RM} and dx_{RM} tend

to be larger on the eastern front than on the western front. As described above, we reason that dh_{RM} is controlled by bench volume, which could be higher on the eastern front due to thicker near-front ice or higher average bench length. Becker et al. (2021) argued that the fact that near-front ice is thicker on the eastern RIS—due to both the thickness of the upstream grounded ice and local basal melting—was at least partly responsible for their observations of higher dh_{RM} (and dx_{RM}) on the eastern portion of the front. Our "snapshot" ICESat and ICESat-2 results do little to refute this hypothesis, with both data sets showing higher average dh_{RM} and dx_{RM} on the eastern front. We also considered whether changes in near-front total ice thickness, which include changes in firn-air column thickness, between the two eras (Figure 4.9; data from Smith, Fricker, Gardner, Medley, et al., 2020) might translate to intermission differences in regional R-M characteristics. The Smith, Fricker, Gardner, Medley, et al. (2020) results show more locations of negative thickness change rates on the eastern portion of the front, with at least one area of thinning upstream of each of regions 1–3, than on the western portion of the front. Indeed, the areas just upstream of regions 4 and 5 of the front experienced a fairly strong thickening trend. Taken in isolation, these spatial patterns suggest that the geometry of the eastern (western) section of the front became less (more) conducive for R-M growth between the ICESat and ICESat-2 eras. This is inconsistent with the results of our Monte Carlo simulations, in which regions 4 and 5 show the least evidence for dh_{RM} increase between the two missions. However, these thickness-change rates and the associated cumulative thickness changes are small, especially in comparison to those observed on other Antarctic ice shelves, which suggests that ice thickness is not the only factor at play. We now examine potential drivers of the spatial variability in R-M characteristics along the RIS front during the ICESat and ICESat-2 periods, starting with why dh_{RM} and dx_{RM} tend to be larger on the eastern front than on the western front. As described above, we reason that dh_{RM} is controlled by bench volume, which could be higher on the eastern front due to thicker near-front ice or higher average bench length. Becker et al. (2021) argued that the fact that near-front ice is thicker on the eastern RIS—due to both the thickness of the upstream grounded

ice and local basal melting—was at least partly responsible for their observations of higher dh_{RM} (and dx_{RM}) on the eastern portion of the front. Our "snapshot" ICESat and ICESat-2 results do little to refute this hypothesis, with both data sets showing higher average dh_{RM} and dx_{RM} on the eastern front. We also considered whether changes in near-front total ice thickness, which include changes in firn-air column thickness, between the two eras (Figure 4.9; data from Smith, Fricker, Gardner, Medley, et al., 2020) might translate to intermission differences in regional R-M characteristics. The Smith, Fricker, Gardner, Medley, et al. (2020) results show more locations of negative thickness change rates on the eastern portion of the front, with at least one area of thinning upstream of each of regions 1–3, than on the western portion of the front. Indeed, the areas just upstream of regions 4 and 5 of the front experienced a fairly strong thickening trend. Taken in isolation, these spatial patterns suggest that the geometry of the eastern (western) section of the front became less (more) conducive for R-M growth between the ICESat and ICESat-2 eras. This is inconsistent with the results of our Monte Carlo simulations, in which regions 4 and 5 show the least evidence for dh_{RM} increase between the two missions. However, these thickness-change rates and the associated cumulative thickness changes are small, especially in comparison to those observed on other Antarctic ice shelves, which suggests that ice thickness is not the only factor at play.

Having considered how differences in ice thickness could affect bench thickness, we now turn our attention to processes that could affect bench length. Previous studies (Kristensen, 1983; Scambos et al., 2008; Wagner et al., 2014) implicated near-surface ocean temperature and surface waves in bench development on tabular icebergs. Becker et al. (2021) reasoned that the same factors were responsible for benches along the RIS front and that both would be limited by the presence of sea ice in the southern Ross Sea. However, spatial patterns in mean summertime sea surface temperature (SST) and 15% sea ice concentration for the period 1999–2019—namely, that solar heat absorption in the Ross Sea Polynya and adjacent open-water areas allowed for significantly warmer SSTs in the western Ross Sea—were inconsistent with their observations

of lower average dh_{RM} on the western RIS front. They speculated that small-scale near-front processes in the eastern Ross Sea concentrate ocean heat near the ocean surface, which in turn promoted bench formation and growth along the eastern front.

Here, we consider changes in the mean summertime SST field, derived from monthly averaged outputs from the fifth generation of the European Centre for Medium-Range Weather Forecasts Re-Analysis (ERA5; Hersbach et al., 2023), and the 15% sea ice concentration contour, derived from monthly satellite passive microwave data (Meier et al., 2021), between the summers leading up to and during the ICESat (December 1999–February 2000 to December 2009–February 2010) and ICESat-2 (December 2014–February 2015 to December 2020–February 2021) missions (Figure 4.9). The ICESat-era sea ice concentration contour did not extend more than 100 km seaward of the eastern RIS front but jutted out nearly 600 km seaward of the western front, possibly due to the formation of polynyas downwind of tabular icebergs C-18 and C-19, which calved in 2002 (Figure 4.1; Martin et al. (2007)). The ICESat-2-era contour was generally broader and extended farther seaward, save for between 150 and 300 km easting. The area of the eastern Ross Sea that had, on average, less than 15% sea ice concentration during the summertime roughly tripled between the ICESat and ICESat-2 periods. Although the ERA5 reanalysis outputs, and thus our estimates of change in mean summertime SST, do not consistently extend all the way to the RIS front, the available estimates near the RIS front indicate that the upper ocean has warmed between the two satellite eras. This holds for most of the Ross Sea, with the region that extends from $\sim$50 km north of the front to the ICESat-2-era 15% sea ice concentration contour experiencing warming of up to $\sim$0.75 °C. The parts of the Ross Sea that experienced the greatest SST increase were those offshore of Ross Island and north of Cape Colbeck and Region 1 of the RIS front. We note that both the segment of the front east of Ross Island and the easternmost portion of Region 1 experienced thinning between the ICESat and ICESat-2 eras (Figure 4.9) and were identified as hotspots of basal melting in airborne ice-penetrating radar data (Das et al., 2020).

The Ross Sea and its contribution to Antarctic Bottom Water have experienced a roughly linear freshening trend since the late 1950s (Jacobs and Giulivi, 2010; Jacobs et al., 2022). However, this time series is also marked by short-term variability; in the mid- to late-2010s, for example, atmospheric variability in the Pacific sector of the Southern Ocean led to increased sea ice formation over the Ross Sea continental shelf, allowing dense shelf water and the Ross Sea Bottom Water to recoup some of this salinity loss (Castagno et al., 2019; Silvano et al., 2020). Most of the freshwater driving the long-term trend originates from excess melting of ice shelves and seasonal melting of sea ice in the Amundsen Sea. The Antarctic Coastal Current delivers this freshwater to the eastern Ross Sea at a rate of $\sim$0.2 m a^{-1}, leading to summertime upper-ocean freshening that continues after the conclusion of the sea ice melt season (Porter et al., 2019). Porter et al. (2019) found that the increases in freshwater content were typically largest in the easternmost Ross Sea. But as the coastal current moves westward along the RIS front, local processes in the Ross Sea, including ice-shelf basal melting during summer, mass loss from the front face, and blowing snow, drive further freshening.

We can now revisit the Becker et al. (2021) hypothesis that small-scale ocean processes create temperature profiles conducive for bench growth on the eastern RIS front. Several lines of evidence point to upper-ocean heating offshore of the eastern front. Vertical sections of potential temperature along the RIS front from 1994, and, to a lesser extent, 1984 and 2000 show elevated ocean temperatures ($>$–1.2 °C) in the upper 100 m of the water column near the eastern section of the front (Smethie and Jacobs, 2005). A section derived from a set of expendable bathythermographs deployed in austral summer 2017 depicts a pool of warm ($>$–0.5 °C) water at roughly the same depth seaward of the western portion of Region 2 and the eastern portion of Region 3 (OGS Explora team, personal communication, 2021). Similarly, autonomous profiling float data from the mid-2010s (Porter et al., 2019) indicated that late-summer mixed layers in the easternmost Ross Sea (seaward of our Region 1) were, on average, nearly 0.5 °C warmer than those in the central Ross Sea (seaward of our regions 2–5). Finally, the changes in sea ice

concentration and SST between the ICESat and ICESat-2 eras (Figure 4.9) suggest an increase in near-surface summertime heat accumulation in the eastern Ross Sea. We propose that this thermal structure, in combination with the upper-ocean buoyancy imparted by the excess freshwater from the Amundsen Sea, causes melting of the front face and bench and R-M growth along the eastern RIS front.

Warm surface waters may cause mode-3 melting on the outermost 100 km of the ice-shelf base and the front face—a process that occurs along much of the RIS front (Horgan et al., 2011; Moholdt et al., 2014)—where the ice shelf is thin and/or when facilitated by transient currents near the front. For instance, Malyarenko et al. (2019) showed that melting of the RIS front face can produce a "wedge" of relatively fresh and buoyant water along the eastern and western portions of the ice shelf, which in turn can facilitate incursions of seasonally warmed Antarctic Surface Water (AASW) into the ice-shelf cavity and mode-3 melting. However, AASW inflow into the RIS cavity is limited to regions beneath the western front where the ice shelf is thin, and possibly only to the area east of Ross Island (Tinto et al., 2019; Stewart et al., 2019; Das et al., 2020; Figure 4.9). As the edge of the wedge closest to the ice shelf must be as thick as the ice-shelf draft, we suspect that the relatively large draft limits the contribution of basal melting to local freshwater injection along the eastern front. However, this instead promotes melting along the front face. This process and summertime sea ice melt increase the freshwater content of the Antarctic Coastal Current (which was already relatively high from the advection of Amundsen Sea freshwater) as it moves toward the western front, where ice-shelf draft is generally smaller. This freshwater flux could grow the wedge current sufficiently to drive melting of the outer portion of the ice-shelf base by increasingly warm AASW (Figure 4.9)—and suppress bench development—along the western front. In other words, we speculate that processes that drive spalling and mode-3 melting of the front face, and thus bench development, on the eastern front ultimately contribute to mode-3 basal melting upstream of the western front, especially that near Ross Island. Validation of this hypothesis will require not only continued monitoring of

R-M characteristics but also of adjacent upper-ocean temperature and salinity and, ideally, direct observations of bench shape and change.

Overall, the spatiotemporal differences in R-M characteristics along the RIS front support our hypothesis that bench development there is affected by upper-ocean heating, near-front ice thickness, and remote and local freshwater inputs. Along the eastern front, and especially in Region 1, the high values of dh_{RM} and evidence of R-M growth between the ICESat and ICESat-2 eras and during the ICESat-2 era reflect the larger ice-shelf draft, as well as broader trends of retreating sea ice and increasing SST (Figure 4.9) and relative warming of the summertime mixed layers (Porter et al., 2019; OGS Explora team, personal communication, 2021) in the adjacent region of the Ross Sea. The evolution of dh_{RM} in the regions comprising the western front is more heterogeneous, and the values of dh_{RM} are generally smaller, despite the presence of a growing and warming area of open water offshore of regions 4–6 (Figure 4.9). This suggests that something is blocking the consistent access of these warm surface waters to the western front—perhaps a seasonal wedge of freshwater that instead directs them beneath the relatively thin ice shelf. This is not to say that there are exclusively small R-M structures or berm structures (which arise, in part, from mode-3 melting) on the western front; we observed some of the largest and most pronounced R-M structures in Region 6 (Figure 4.4e).

Temporarily setting aside the east–west differences in R-M structures on the RIS front, by our hypothesis, bench growth should occur during austral summer, when sea ice retreat allows the upper ocean to warm to above freezing (Porter et al., 2019) and surface waves to access the front. During fall, winter, and spring, when sea ice typically extends all the way to the RIS front, we would expect that benches would experience minimal growth. However, our analysis of changes in R-M structures in successive ICESat-2 GT profiles (e.g., Figures 4.4b–4.4e) indicates that they can experience growth and/or erosion at various points of the year. In that data set, dh_{RM} growth was most common between repeats in austral fall and winter (as illustrated by the repeats for cycles 10 and 11 in Figure 4.4e). This challenges our argument that sea ice impedes R-M

development by dampening surface waves and raises the question of whether other processes, possibly related to mixed-layer deepening and residual heat storage through fall and winter (Porter et al., 2019), can lead to bench growth. That decreases in dh_{RM} occurred between spring and summer repeats (as illustrated by the repeats for cycles 13 and 14 in Figure 4.4d) suggests that warming of surface waters and wave action can both lengthen and erode underwater benches. These results drive us to revisit our assumption that wave action promotes bench development. It is possible that waves contribute to the development of the initial wavecut via increased turbulence and forced convection (Orheim, 1987; Wagner et al., 2014) but become less significant as the overhanging ice fails and the bench begins to form. Indeed, Wagner et al. (2014) argued that, for icebergs in Baffin Bay, wavecuts may grow most efficiently when there is minimal vertical mixing and maximum heating in the near-surface layer. Perhaps existing benches only need warm water, and not necessarily high wave action, to grow. Although we were able to resolve ocean waves in some of the GT profiles that crossed the RIS front, a thorough assessment of the contribution of surface wave action to R-M development is beyond the scope of this work.

4.6.3 R-M development in the context of the broader calving cycle

The observed trends in dh_{RM} and dx_{RM} are generally consistent with our understanding of bench development—although we have had to reconsider our assumptions about seasonality, as described above—and we are confident that the ICESat and ICESat-2 data sets include representations of R-M structures at various stages of their evolution. But we have yet to resolve a small-scale calving event associated with an R-M structure along a well-aligned satellite altimetry track. We expect that such a time series would show an R-M structure prior to calving and a berm structure after calving, reflecting the restoration of a vertical front face and the transition between dominant bending moments. Our comparison of observed and expected RIS front advance (Figure 4.8), an alternative method for identifying small-scale calving events, suggests that such calving may have taken place over the ICESat and ICESat-2 eras.

We examined four case studies that show evidence of small-scale frontal retreat in one of the six regions of the RIS front: roughly in the middle of Region 3 between late 2005 and late 2006 (Figures 4.8a and 4.8c); toward the eastern end of Region 6 between late 2004 and late 2005 (Figures 4.8a and 4.8d); at the eastern end of Region 1 between late 2018 and late 2019 and then between late 2021 and late 2022 (Figures 4.8b and 4.8e); and toward the western end of Region 5 between late 2019 and late 2020 (Figures 4.8b and 4.8f), which is approximately coincident with a 1–10 km^2 calving event that Qi et al. (2021) identified from satellite imagery. (The notch that developed ∼20 km east of Ross Island during the ICESat era appeared too wide to have been formed by a single small iceberg, so we did not include it as a case study.) Based on trends in mean dh_{RM} alone, which show evidence of growth in regions 3 and 6 between the ICESat and ICESat-2 eras (Figure 4.7; Table 4.2) and in Region 5 during the ICESat-2 era (Figure 4.3; Table 4.1; Figure 4.S2), it is feasible that benches and R-M structures along these segments of the front grew sufficiently to induce calving along basal crevasses. However, we need a better understanding of the relationships between bench length, dh_{RM}, dx_{RM}, and the strength and yield stress of ice near the RIS front to confirm this. While we cannot directly prove that these mass-loss events occurred as a result of bench-driven flexure, the amount of frontal retreat (∼0.1–∼0.7 km) is of the same order of magnitude as the local ice-shelf thickness, which is about as wide as Reeh (1968) argued that icebergs that calve from floating glaciers and ice shelves due to hydrostatic imbalances along their fronts should be. Mosbeux et al. (2020) reported similar values for their parameter x^*, which they interpreted as the dominant control on R-M-driven iceberg width. In addition, the scalloping along the front (e.g., in Figure 4.8a, right inset) implies mass loss via calving of ∼5-km-long (along front) icebergs, which is comparable to the scale of along-front variability of R-M characteristics (a few km) observed by Becker et al. (2021).

One environmental factor that we have yet to assess, and that Horgan et al. (2011) implicated in differences in cross-front elevation and melt-rate profiles along the RIS front, is time since tabular calving event. The melt rates that Horgan et al. (2011) derived from repeat-track

ICESat elevation data increased exponentially toward the front. On average, melt-rate profiles from the regions of the front that had experienced the least amount of calving since 2000 (Nascent Iceberg and C-18; Figure 4.1a) did not decrease as rapidly with distance from the front as they did in the regions making up the B-15 and C-19 calving areas. This spatial variability is seemingly linked to duration of exposure to mode-3 melting and calving-related changes in the shape of the frontal part of the ice shelf. Prior to a tabular calving event, the ice-shelf thins toward the front due to spreading and mode-3 melting; this thinning signal becomes more pronounced as melting continues in the absence of calving. After calving, the near-front cross-section returns to a more rectangular configuration, with a reduced basal slope. Calving also changes the character of the front face from rough and subvertical (pre-calving), reflecting the influence of differential mass loss, to closer to vertical (post-calving).

From our analysis of MODIS imagery, the only segments of the RIS front that have not experienced large-scale calving in the 21st century are the western portion of Nascent Iceberg and the easternmost and westernmost ∼10–20 km of the front (Figures 4.1a and 4.9). Our two data sets represent epochs immediately after calving (ICESat) and ∼two decades after calving (ICESat-2). The time since calving metric is also related to our assumption that benches that form on thicker sections of the ice front lead to larger R-M structures. Applying this hypothesis to the decades-long tabular calving cycle, we speculate that R-M structures reach their maximum height for a given segment of the front in the years following a large calving event, which removes ice that has thinned as a result of mode-3 basal melting. This appears to be the case in regions 1, 2, 3, 5, and 6, all of which mostly span sections of the front that have calved since 2000 and showed varying evidence of dh_{RM} growth during the ICESat-2 era and between the ICESat and ICESat-2 eras. The evidence of consistent dh_{RM} growth through the ICESat and ICESat-2 periods is particularly strong for regions 1–3, where large calving events occurred in early 2000. Our estimates for when mean dh_{RM} and bench length would have been zero (based on the ICESat-2-era trend; see subsection 4.6.1) in these regions—mid-2001, late 2008, and early

1996, respectively—agree somewhat well with calving in early 2000. In contrast, we expect that R-M structures on sections of the front that have not experienced recent calving (and so have been subjected to additional basal melting) would show limited or no growth. This is supported by the fact that Region 4, which contains the portion of Nascent Iceberg that has not experienced recent calving, is the only region of the front that showed a significant negative trend in dh_{RM} over the ICESat-2 era (Figure 4.S2) and a decrease in median dh_{RM} between the ICESat and ICESat-2 eras (Table 4.2).

4.6.4 Future changes in buoyancy-driven flexure and outstanding questions

Coupled climate models predict that Antarctic sea ice will decline in the 21st century (Roach et al., 2020), but there is low confidence in these projections (Fox-Kemper et al., 2021). Reid and Massom (2022) determined that the annual maximum amount of Ross Sea coastline that was completely exposed to the Southern Ocean due to lack of sea ice declined by 6 km a^{-1} between 1979 and 2020. (We note that the authors' definition of the Ross Sea included portions of the Marie Byrd Land and Victoria Land coasts.) This appears to have been driven by decreasing coastal exposure in the western Ross Sea between late-December and March. We have reported significant changes in summertime sea ice and upper-ocean thermal conditions in the Ross Sea between the ICESat and ICESat-2 periods (Figure 4.9), which we hold contributed to spatiotemporal variability in R-M characteristics along the RIS front. We reason that future changes in sea ice, regardless of their direction, will further modify both R-M evolution and the related, and possibly competing, process of mode-3 melting. In addition, Nascent Iceberg will calve at some point in the future. We argue that this will "reset" bench development along the section of Region 4 that has not recently calved and alter near-front ocean conditions.

Changes in sea ice and the configuration of the RIS front would also affect the rate and consequences of bench-driven calving. Between August 2005 and August 2020, Qi et al. (2021) estimated that the average calving rate from RIS was 5 Gt a^{-1}. We suspect that the R-M

mechanism caused some of this mass loss, but we need accurate and repeated estimates of both the R-M-driven and the overall RIS calving fluxes to confirm this. Small icebergs like those produced by the R-M mechanism fall on the lower end of the –1.5 power-law distribution of calved volume and freshwater flux put forth by Tournadre et al. (2016) and applied by England et al. (2020). However, small icebergs tend to deposit their freshwater much closer to their point of origin and the coastline than do large tabular icebergs (England et al., 2020). This can affect local salinity, stratification, and mixed-layer depth, which in turn can trigger increased sea ice formation (Merino et al., 2016). A more active R-M mechanism could erode parts of the ice shelf that provide significant buttressing to upstream grounded ice. For example, extensive small-scale calving near Ross Island and Minna Bluff, an area which is vulnerable to mode-3 basal melting, would remove ice that both is outside of the Fürst et al. (2016) safety band and that "tele-buttresses" faraway grounded ice (Reese et al., 2018).

Although we are confident in our adjustments to the Becker et al. (2021) front and R-M detection algorithm, there is still considerable room for improvement. The current version does not always correctly detect an R-M structure and/or the location and height of its rampart or moat, especially when there are data gaps near the front. We manually removed or edited the returned dh_{RM} and dx_{RM} values for a few of these examples, but the sheer number of front detections prohibited manual quality control for all possible R-M structures. Another issue that our algorithm does not currently address is the inheritance of topography from upstream rifts and suture zones. As Walker et al. (2021) warned, uplifted rift wall flanks are morphologically similar to R-M structures, and these or other surface features may be sufficiently preserved during downstream advection to combine (and confound) with bench-driven elevation signals at the ice front. In addition, the algorithm interprets broad features with very large values of dx_{RM} as R-M structures, but it is possible that these features do not arise from buoyant flexure and instead reflect advected topography. In the future, we might consider training the algorithm with various types of R-M structures to avoid these pitfalls and potential misdetections, as well as fine-tuning it to search for

evidence of calving along well-aligned repeating GTs. This would improve our understanding of the R-M life cycle and validate our theory that calving elicits a transition between R-M- and berm-type front shapes. Finally, we might modify the algorithm to look for the submerged bench itself. Fricker et al. (2021) demonstrated that the ICESat-2 ATL03 geolocated photon product can resolve secondary ice surfaces below at least 6 m of meltwater, but we could also search for the bench in ATL06 and ATL12 (the analogous ocean product) data.

Many questions remain about how R-M structures develop, which points to the need for continued (but enhanced) monitoring and modeling of these features. For instance, we expect that the ice shelf responds both elastically and viscously to the initial appearance of the buoyant bench, but it would be helpful to have an observation-based estimate of how long it takes for an R-M structure to develop after the aerial portion of the ice front begins to collapse. (This would require ICESat-2-based estimates of bench length and, preferably, subsurface observations of front geometry like those presented by Orheim, 1987, and Sutherland et al., 2019). It would also be useful to understand if and how along-front variability in column-averaged density contributes to along-front variability in flexure. Once formed, R-M structures can both grow and shrink in height (Figure 4.4), but it is unclear what causes this erosion—possibly erosion of the bench and aerial front, or accumulation of water or locally precipitated or wind-blown snow in the moat—and how R-M structures persist in the face of this process. The concept of water storage in the moat raises the question of whether R-M structures could pool and route surface meltwater, which is not currently a major factor in Antarctic mass balance but is projected to increase with climate warming (Trusel et al., 2015). Finally, we know that R-M structures also form on the large Filchner-Ronne and Amery (Walker et al., 2021) ice shelves, which are also fairly stable. But we did not search for them on smaller ice shelves, where thinning due to basal melting may encourage ice-front retreat via frequent, small-scale calving (Liu et al., 2015).

Future efforts should also focus on bench-driven small-scale calving—from RIS and from large icebergs, which could decay via the R-M mechanism—and ice–ocean interactions along

the RIS front. Calving-related topics that need more attention include the relationship between dx_{RM}, the position of maximum stress from Mosbeux et al. (2020), and the size of the associated calving event, and whether the maximum values of dh_{RM} along the RIS front reveal anything about ice strength and crevassing. Another outstanding question is how bench length relates to calving. Hughes (2002), who laid out a mathematical theory for the formation and calving of underwater ice ledges (i.e., benches) on ice walls and ice shelves, found that benches should calve when their length nears half of the subaqueous ice thickness. However, he determined that benches break along bottom crevasses at the horizontal position of the aerial ice front, not some distance upstream of the front. Again, subsurface observations of benches could help elucidate this connection. If paired with coincident temperature and salinity measurements, they could also provide critical insights into the spatial relationship between R-M development and mode-3 melting. Where mode-3 melting takes place, we are specifically interested in whether the associated ocean heat and buoyant meltwater could melt or otherwise hinder benches. It is possible that mode-3 melting acts as a stabilizing force for R-M development, reducing bench thickness and volume and thereby limiting R-M growth. Its meltwater may also regulate bench lengthening by forming a freshwater wedge, but by that logic, waterline erosion may as well.

4.7 Conclusions

Rampart-moat (R-M) surface structures form on ice shelves when waterline erosion and collapse of the aerial portion of the ice face create a buoyant underwater bench that bends the edge of the ice shelf upward. We employed NASA satellite laser altimetry data to explore their evolution along the Ross Ice Shelf (RIS) front between 2003 and 2022. Full resolution of R-M structures requires the dense spatial coverage provided by the altimeter onboard ICESat-2 (2018–present), but we demonstrated that these features also existed on the RIS front during the ICESat era (2003–2009) and could be resolved by that mission's altimeter. On average, R-M

structures from both periods are taller and wider (i.e., have larger values of dh_{RM} and dx_{RM}) on the eastern section of the RIS front. Unsurprisingly, the ICESat-2 data yielded a greater range of, and considerably higher, dh_{RM} values than the lower-resolution ICESat data, but the distributions of dx_{RM} were fairly similar.

Over the ∼four-year ICESat-2 period, R-M structures showed a statistically significant increase in dh_{RM} for the full RIS front but insignificant changes in dx_{RM}. The positive trend in dh_{RM} appeared to be driven by R-M growth on the eastern front, which contrasted with some signals on the western front, e.g., a significant decrease in dh_{RM} on the segment comprising Nascent Iceberg. The ICESat-2 data set did not show direct evidence of small-scale calving due to the bending stresses imparted by the buoyant bench, but discrepancies between expected and observed ICESat-era and ICESat-2-era front positions suggest that some small-scale frontal mass-loss process counteracted expected advance during these periods. We extended the temporal analysis to include the ICESat data by downsampling ICESat-2-derived R-M characteristics to their ICESat-resolution counterparts. We found convincing evidence of dh_{RM} growth between the ICESat and ICESat-2 periods on the eastern front and an apparent negative trend in dh_{RM} near Nascent Iceberg. The spatiotemporal patterns in R-M characteristics on the RIS front suggest that R-M evolution is affected by near-front ice thickness and ocean and sea ice conditions in the Ross Sea, as Becker et al. (2021) proposed. However, we must invoke an additional factor, tabular calving history, to explain the Nascent Iceberg anomaly. Nascent Iceberg is one of the only segments of the front that did not calve in the 21st century, and we hypothesize that the increased exposure to basal melting that accompanies lack of calving has limited local R-M growth since the ICESat period.

Antarctic ice fronts are complex environments where ice shelves, sea ice, the Southern Ocean, and the atmosphere interact in numerous ways, some of which can impact the stability of ice shelves and upstream grounded ice. It is important that coupled models incorporate small-scale processes like bench formation, which could modify the heat and salinity budgets of the near-front

ocean and/or lead to small-scale calving, especially in the context of a warming ocean. This will involve continued and improved observations of bench and R-M evolution on the RIS front and similar efforts on other ice fronts. Changes in bulk R-M characteristics may also indicate broader changes in sea ice and ocean thermal structure near ice fronts, which will be key factors in future ice-shelf and ice-sheet mass balance.

4.8 Data availability

ICESat Version 34 GLAH12 data (https://nsidc.org/data/glah12/versions/34) and ICESat-2 Version 5 ATL06 data (https://nsidc.org/data/atl06) are available for download at the National Snow and Ice Data Center (NSIDC). The latest versions of the Python code for ICESat-2 ATL06 data download and the MATLAB code for ICESat GLAH12 and ICESat-2 ATL06 front and R-M structure detection will be available via Zenodo upon submission. The gridded MOG2D dynamic atmospheric correction values applied to the ICESat elevations can be accessed at https://www.aviso.altimetry.fr/. We used imagery from the NASA Worldview application (https://worldview.earthdata.nasa.gov), part of the NASA Earth Observing System Data and Information System; MODIS thermal images from Version 2 of the Images of Antarctic Ice Shelves (https://nsidc.org/data/nsidc-0102/versions/2); elevation data from Version 1.1 of the Reference Elevation Model of Antarctica (http://data.pgc.umn.edu/elev/dem/setsm/REMA/mosaic/); and Version 2 of the 2003–2004 MODIS Mosaic of Antarctica image map (https://nsidc.org/data/nsidc-0280/versions/2). The Depoorter et al. (2013) mask is available at https://doi.pangaea.de/10.1594/PANGAEA.819150 and the 2018 Baumhoer et al. (2021) Antarctic coastline at https://download.geoservice.dlr.de/icelines/files/. Sea ice concentration data are from the NOAA/NSIDC Climate Data Record of Passive Microwave Sea Ice Concentration, Version 4 (https://nsidc.org/data/g02202/versions/4), and ERA5 monthly averaged reanalysis sea surface temperature outputs are from modified Copernicus Climate Change Service information (2022; https://cds.climate.copernicus.eu

/cdsapp#!/dataset/reanalysis-era5-single-levels-monthly-means). Neither the European Commission nor ECMWF is responsible for this use of the Copernicus information and component data. Finally, the Smith, Fricker, Gardner, Medley, et al. (2020) total ice thickness change data can be accessed at https://digital.lib.washington.edu/researchworks/handle/1773/45388.

4.9 Acknowledgments

We thank Jennifer Bohlander and Ted Scambos for sharing their ICESat-era Ross front positions and Chad Greene for allowing us to use the extrapolated Antarctic ice velocity composite that he and colleagues derived from ITS_LIVE and MEaSUREs InSAR-based velocities. We are grateful to Cyrille Mosbeux for his insights on buoyancy-driven flexure throughout this project; to Daniel Blatter for sharing his expertise on Monte Carlo simulations; and to Alena Malyarenko for her thoughts on how bench development might interact with other near-front processes. This study was funded by NASA grants 80NSSC20K0977 and NNX17AG63G and by NSF grants 1443677 and 1443498.

Chapter 4, in part, is currently being prepared for submission for publication of the material. Becker, M. K., Fricker, H. A., Padman, L., Howard, S. L., & Siegfried, M. R. The dissertation author was the primary investigator and author of this material.

4.10 Appendix: ICESat-2 downsampling and ICESat–ICESat-2 Monte Carlo simulations

The first step in the ICESat-2 downsampling process was to identify 10 categories of R-M structures based on their values of dh_{RM} and dx_{RM}, as resolved from the ATL06 product: (1) any dh_{RM} and very low dx_{RM} ($<$172 m); (2) low dh_{RM} ($<$5 m) and low dx_{RM} ($\geq$172 m and $<$344 m); (3) low dh_{RM} and intermediate dx_{RM} ($\geq$344 m and $<$516 m); (4) low dh_{RM} and high dx_{RM}

($\geq$516 m); (5) intermediate dh_{RM} ($\geq$5 m and $<$10 m) and low dx_{RM}; (6) intermediate dh_{RM} and intermediate dx_{RM}; (7) intermediate dh_{RM} and high dx_{RM}; (8) high dh_{RM} ($\geq$10 m) and low dx_{RM}; (9) high dh_{RM} and intermediate dx_{RM}; and (10) high dh_{RM} and high dx_{RM}. We defined these categories to encompass all of the ATL06-derived dh_{RM}–dx_{RM} combinations reported in this study. For each category, we identified a representative GT profile (or case study) and took the algorithm-generated values of dh_{RM} and dx_{RM} as the "true" dimensions of the R-M structure in that profile. We then generated synthetic ICESat profiles by averaging the ATL06 segment heights across 65 m (ICESat's approximate footprint) bins, spaced by 172 m (ICESat's approximate along-track spacing). To account for the effect of along-track shot location on ICESat's ability to resolve an R-M structure, we varied the along-track location of the bin centers by 2 m increments from 0 m to 170 m, yielding 86 synthetic ICESat profiles per case study.

For each synthetic ICESat profile, we computed dh_{RM} and dx_{RM} using a similar method as we did for the real ICESat profiles. However, we did not require that a moat be detected in order to search for a rampart; we simultaneously searched for a rampart within a 200 m window centered on the ICESat-2-detected front and a moat in a 1.9 km window upstream of the rampart window. This allowed for the simulation of ICESat profiles that showed a berm-type front shape. Thus, for each case study, we generated distributions of 86 dh_{RM} and dx_{RM} values that could theoretically be derived from ICESat shots that sampled the representative R-M structure. We took the median of each distribution as the synthetic ICESat value for that R-M characteristic and calculated a scale factor to relate it to the corresponding value from ICESat-2.

Equipped with a strategy for controlling for the differences in resolution between ICESat and ICESat-2, we implemented a simple Monte Carlo simulation to compare the regional distributions of dh_{RM} and dx_{RM} from the two missions. For each region, we treated the ICESat-2 distributions of dh_{RM} and dx_{RM} as inputs and resampled each n = 10,000 times with replacement. We then paired the dh_{RM} and dx_{RM} samples together to form 10,000 dh_{RM}–dx_{RM} pairs (that described 10,000 theoretical, but statistically plausible, R-M structures) per region. For

each resampled pair, we applied the appropriate synthetic ICESat–ICESat-2 scale factors, which yielded the dimensions of the theoretical ICESat-2-era R-M structure that would have resulted from ICESat sampling. As our regional analysis only includes ICESat- and ICESat-2-derived dh_{RM} and dx_{RM} values that are greater than zero—that is, it excludes profiles that sampled berm structures—we removed all synthetic ICESat values of dh_{RM} and dx_{RM} equal to zero. We compared the resulting regional synthetic ICESat distributions for both R-M characteristics with their observed ICESat counterparts, testing the null hypothesis that there is no difference between the bulk ICESat-era and ICESat-2-era (synthetic ICESat) R-M characteristics.

Table 4.1: Mean values of R-M characteristics (dh_{RM} and dx_{RM}) during ICESat-2 cycles 1–4, 5–8, 9–12, 13–17, and 1–17 ("All cycles") for each of the six regions of the RIS front, the eastern and western portions of the front (regions 1–3 and 4–6, respectively), and the full front ("All"). Uncertainties represent the standard error of the mean values.

	Cycles 1–4		Cycles 5–8		Cycles 9–12		Cycles 13–17		All cycles	
Region(s)	dh_{RM} [m]	dx_{RM} [m]	dh_{RM} [m]	dx_{RM} [m]	dh_{RM} [m]	dx_{RM} [m]	dh_{RM} [m]	dx_{RM} [m]	dh_{RM} [m]	dx_{RM} [m]
1	10.5 ± 0.4	456 ± 13	11.3 ± 0.4	456 ± 14	12.1 ± 0.4	428 ± 12	12.4 ± 0.4	425 ± 14	11.7 ± 0.2	440 ± 7
2	6.4 ± 0.2	451 ± 12	6.8 ± 0.3	448 ± 11	7.7 ± 0.3	450 ± 8	8.3 ± 0.2	453 ± 8	7.4 ± 0.1	451 ± 5
3	4.8 ± 0.2	319 ± 7	5.3 ± 0.2	318 ± 6	5.4 ± 0.2	321 ± 5	5.6 ± 0.2	315 ± 5	5.3 ± 0.1	318 ± 3
East (1–3)	6.5 ± 0.2	391 ± 7	6.9 ± 0.2	383 ± 6	7.4 ± 0.2	382 ± 5	7.6 ± 0.2	378 ± 5	7.2 ± 0.1	383 ± 3
4	3.6 ± 0.2	191 ± 6	3.5 ± 0.2	185 ± 6	3.2 ± 0.2	175 ± 6	3.3 ± 0.2	182 ± 6	3.4 ± 0.1	183 ± 3
5	3.8 ± 0.2	225 ± 7	3.9 ± 0.2	235 ± 6	4.1 ± 0.2	232 ± 5	4.2 ± 0.1	237 ± 6	4.0 ± 0.1	233 ± 3
6	5.8 ± 0.3	291 ± 10	6.4 ± 0.3	299 ± 8	6.6 ± 0.3	283 ± 7	5.7 ± 0.3	266 ± 8	6.1 ± 0.1	283 ± 4
West (4–6)	4.4 ± 0.1	234 ± 5	4.5 ± 0.1	237 ± 4	4.6 ± 0.1	231 ± 4	4.4 ± 0.1	230 ± 4	4.5 ± 0.1	233 ± 2
All	5.4 ± 0.1	307 ± 5	5.6 ± 0.1	308 ± 4	6.0 ± 0.1	303 ± 4	5.9 ± 0.1	300 ± 4	5.7 ± 0.1	304 ± 2

Table 4.2: Sample size (n) and mean, standard deviation (SD), median, and interquartile range (IQR) values of R-M characteristics for the observed and synthetic ICESat (derived from ICESat-2) distributions for each of the six regions of the front.

Region	Observed ICESat (2003–2009)									Synthetic ICESat (2018–2022)								
	n	dh_{RM} [m]				dx_{RM} [m]				n	dh_{RM} [m]				dx_{RM} [m]			
		Mean	*SD*	*Median*	*IQR*	*Mean*	*SD*	*Median*	*IQR*		*Mean*	*SD*	*Median*	*IQR*	*Mean*	*SD*	*Median*	*IQR*
1	35	0.74	0.55	0.64	0.83	364	141	340	170	9,568	5.54	2.12	5.18	1.89	410	75	401	96
2	85	0.95	0.86	0.78	0.71	437	159	508	171	9,424	4.48	1.96	4.66	2.11	391	85	396	110
3	139	0.88	1.00	0.55	0.87	393	181	340	256	9,654	2.49	1.86	2.59	3.15	241	81	235	118
4	38	0.84	0.81	0.63	1.08	277	148	170	171	4,662	1.10	1.30	0.41	1.98	188	60	172	78
5	51	0.57	0.74	0.35	0.61	310	145	339	339	7,840	1.44	1.30	0.68	2.34	189	66	172	70
6	86	0.53	0.47	0.43	0.54	425	195	341	172	8,184	2.69	2.02	3.08	3.71	252	77	250	126

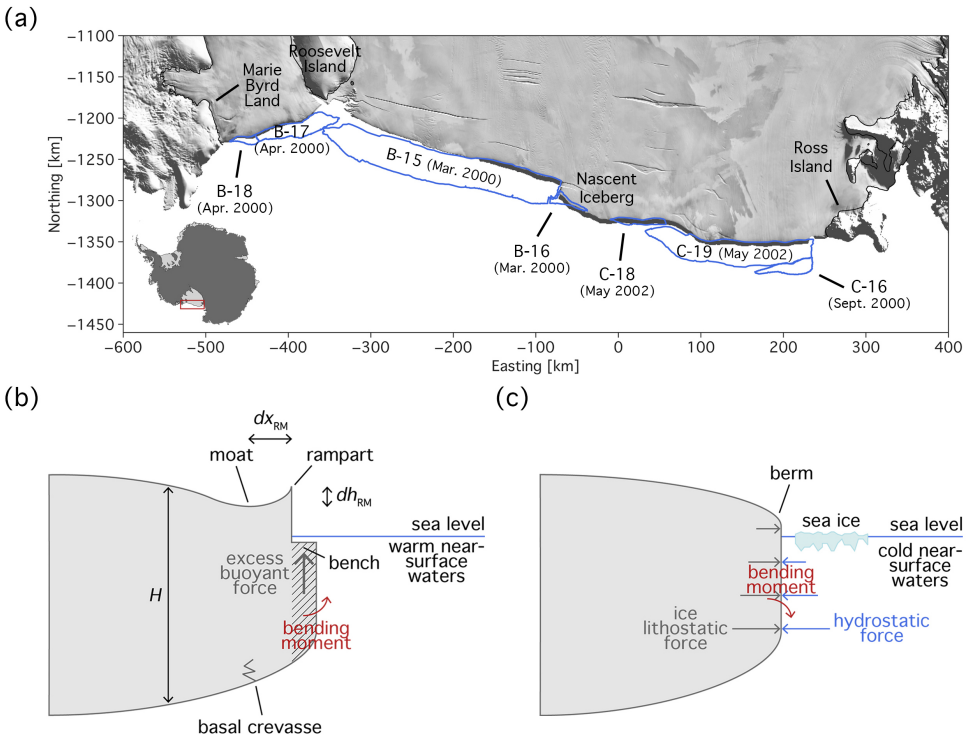

Figure 4.1: (a) Approximate locations and timings (Lazzara et al., 2008; MacAyeal et al., 2008) of early-2000s major Ross Ice Shelf (RIS) calving events B-15, B-16, B-17, B-18, C-16, C-18, and C-19, traced from Moderate Resolution Imaging Spectroradiometer (MODIS) visible images from mid- to late March 2000 downloaded from NASA Worldview (B-15, B-16, B-17, and B-18), MODIS visible images from late September 2000 (C-16), and MODIS thermal images from April and May 2002 (Scambos et al., 2022) (C-18 and C-19). The background is the MODIS Mosaic of Antarctica 2003–2004 Image Map (Haran et al., 2005; Scambos et al., 2007), with the Depoorter et al. (2013) RIS mask (thin black line) superimposed. The projection is Antarctic Polar Stereographic with a standard latitude of 71°S and a standard longitude of 0°. Schematics of ice-shelf (b) rampart-moat (R-M; as in Figure 1b of Becker et al., 2021) and (c) berm surface structures and the environmental conditions under which they form. Near-front basal melting contributes to the shape of both the ice-shelf base and the surface in each case. While these schematics are meant to represent endmembers for which the (b) upward and (c) downward bending moments dominate, in reality, the R-M structure results from a combination of the two bending moments. In (b), the vertical scale of the rampart-moat feature (a few meters from the top of the rampart to the bottom of the moat) and the horizontal scale of the bench (a few tens of meters long; the bench is represented by the hatched area) are exaggerated relative to the ice-shelf thickness ($\sim$300 m on the upstream edge of each schematic). The moat is typically a few ice thicknesses ($<$1 km) upstream of the rampart.

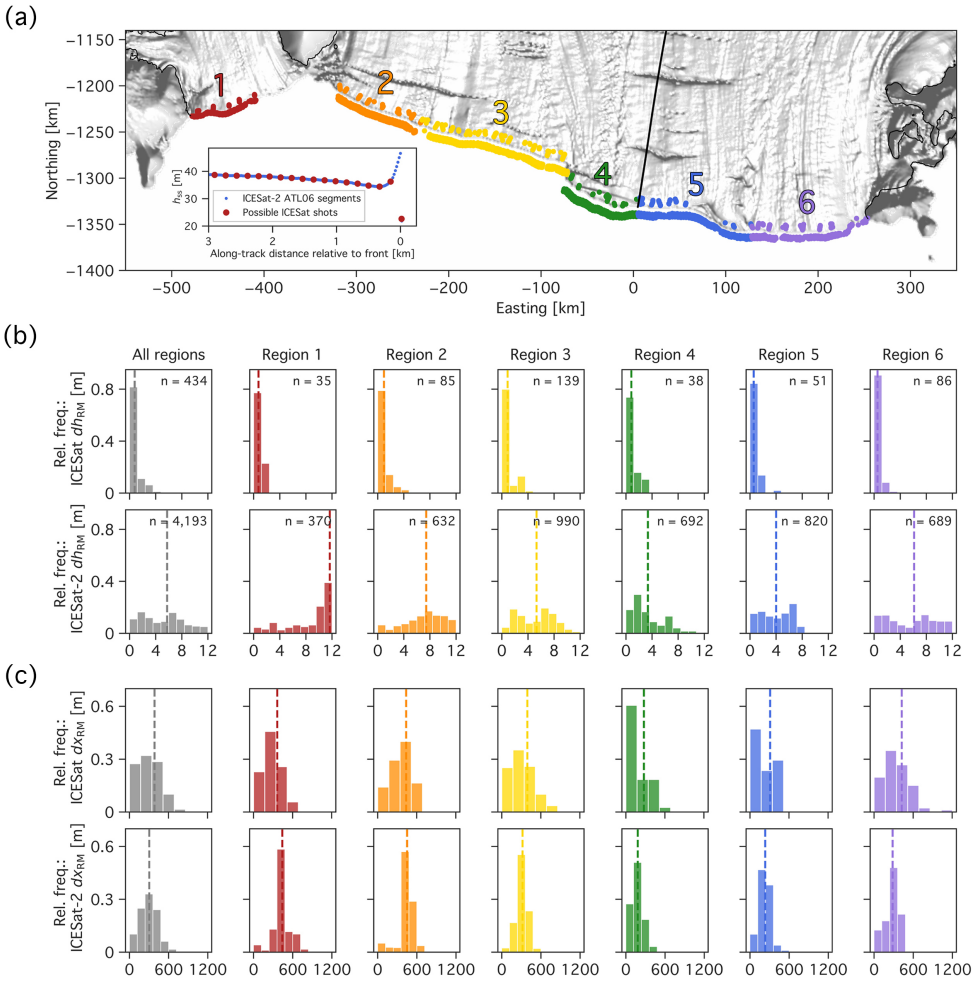

Figure 4.2: (a) Locations of the six regions of the RIS front used in the regional statistical analysis of R-M characteristics, superimposed onto a hill-shaded version of the Reference Elevation Model of Antarctica (REMA) mosaic (Howat et al., 2019). Colored dots show the rampart locations for all ICESat and ICESat-2 profiles with R-M structures included in the regional analysis. The thin black line indicates the Depoorter et al. (2013) RIS mask and the thick black line the streamline marking the approximate boundary between shelf ice from the West and East Antarctic ice sheets. The projection is Antarctic Polar Stereographic with a standard latitude of 71°S and a standard longitude of 0°. Inset shows a possible ICESat profile (large red dots) of height above instantaneous sea surface (h_{ss}) derived from the ICESat-2 ATL06 profile (small blue dots) across an R-M structure for beam gt1r for the Cycle 5 repeat of RGT 1372 (also shown in Figure 4.S8). Relative frequency histograms of (b) dh_{RM} and (c) dx_{RM} for the full front ("All regions") and each region shown in (a) and for each mission (top row of each panel, ICESat; bottom row of each panel, ICESat-2). Dashed vertical lines indicate regional mean values. Annotations in the upper right of the histogram plots in (b) provide the number of profiles with R-M structures in each region (n).

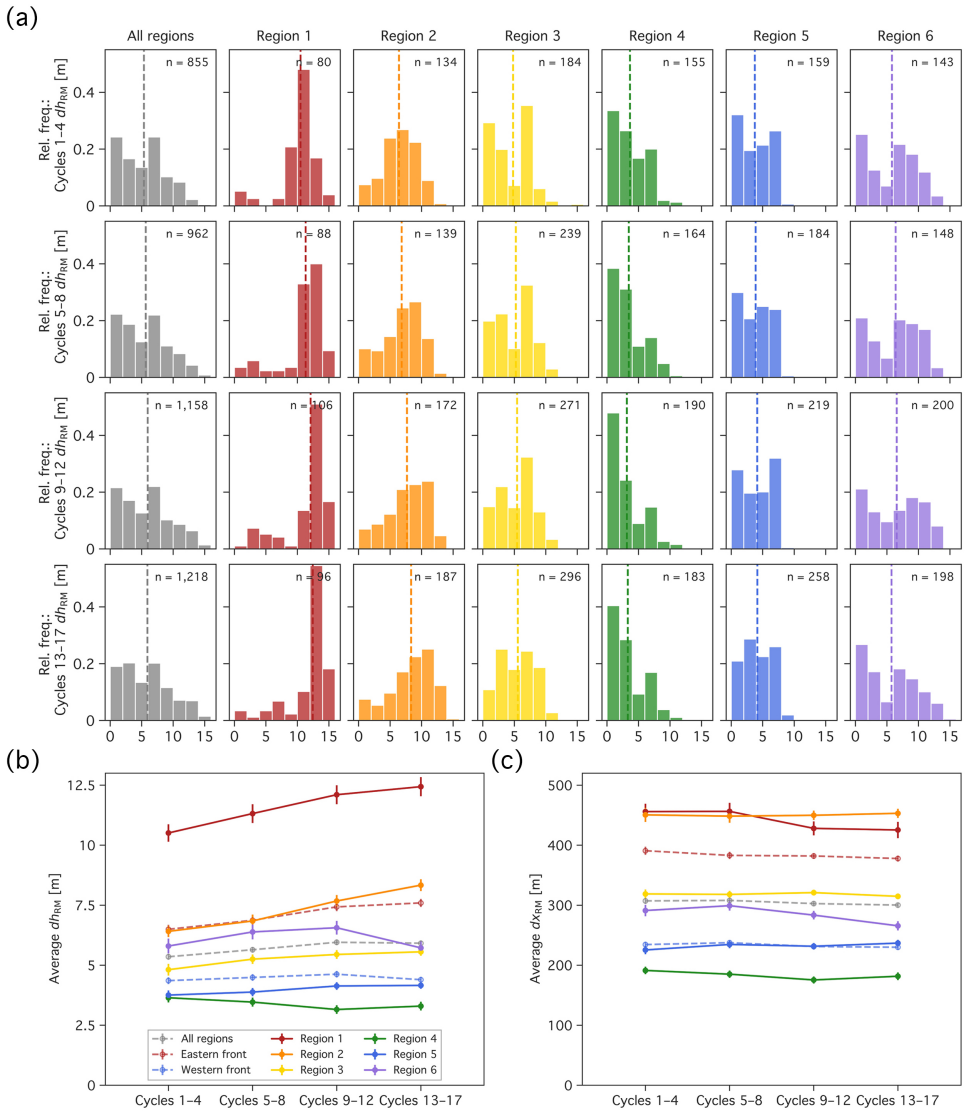

Figure 4.3: (a) Relative frequency histograms of dh_{RM} for the full front ("All regions") and each of the six regions of the RIS front over four time periods during the ICESat-2 mission: cycles 1–4 (October 2018–September 2019); 5–8 (September 2019–September 2020); 9–12 (September 2020–September 2021); and 13–17 (September 2021–October 2022). As in Figure 4.2, dashed vertical lines indicate mean values, and annotations in the upper right of the histogram plots provide the number of profiles with R-M structures in each region and for each time period (n). Time series of the mean values of (b) dh_{RM} and (c) dx_{RM} during the four time periods for the full front ("All regions"), the eastern and western portions of the front (regions 1–3 and 4–6, respectively), and each region of the front. Error bars represent the standard error of the mean values.

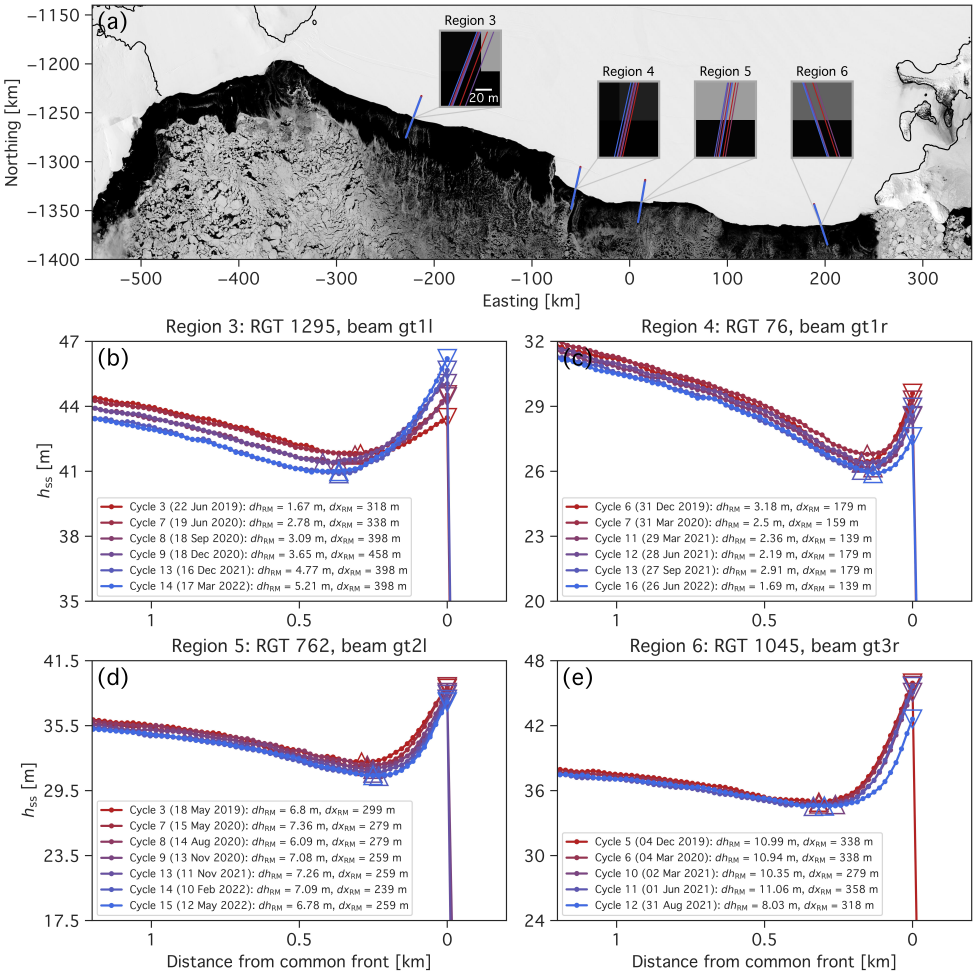

Figure 4.4: (a) MODIS image from November 21, 2021, downloaded from NASA Worldview, overlaid with the locations of four sets of repeating ICESat-2 ground track (GT) profiles (one for each of regions 3, 4, 5, and 6 of the RIS front) that show persistent R-M structures and crossed the front within 5° of the local velocity vector. The thin black line indicates the Depoorter et al. (2013) RIS mask. The projection is Antarctic Polar Stereographic with a standard latitude of 71°S and a standard longitude of 0°. The insets emphasize the high precision of the repeats; the scale bar in the leftmost inset applies to all four insets. (b)–(e) Stacked across-front ATL06 profiles of h_{ss}, all referenced to the location of the front in the earliest repeat, for each set of repeating GT profiles whose location is given in (a). For each profile, the standard (inverted) triangle indicates the location of the moat (rampart), and the corresponding legend entry includes the values of dh_{RM} and dx_{RM} and relevant timing information. The set in (b) shows a monotonic increase in dh_{RM} over the ICESat-2 period; the sets in (c), (d), and (e) show cycles of R-M structure erosion and regrowth.

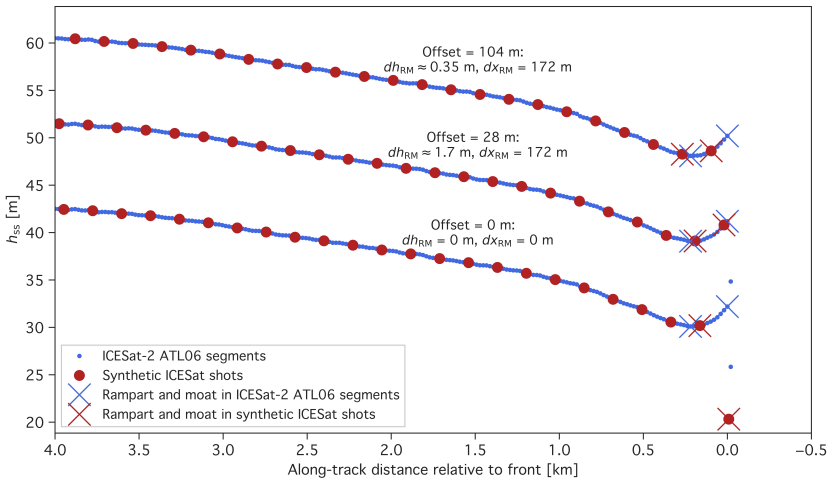

Figure 4.5: Three of the 86 possible synthetic ICESat profiles (large red dots, with rampart and moat locations marked as red crosses) that could be derived from the ICESat-2 ATL06 GT profile (small blue dots, with rampart and moat locations marked as blue crosses) selected as the low dh_{RM}, low dx_{RM}, case study (the Cycle 11 repeat for beam gt2r for RGT 0213). We generated each synthetic ICESat profile using a specific offset value for the center of the bins across which we averaged the ATL06 segment heights; the offset value and corresponding values of dh_{RM} and dx_{RM} are shown in the annotations. The center synthetic ICESat profile (offset = 28 m) yielded the highest value of dh_{RM} for this case study; the top synthetic ICESat profile (offset = 104 m) yielded the value of dh_{RM} closest to the median of the 86 possible values. The bottom profile-pair (offset = 0 m) shows the true h_{ss} values for the ATL06 and synthetic ICESat profiles; the other two profile-pairs have been shifted upward for better visualization.

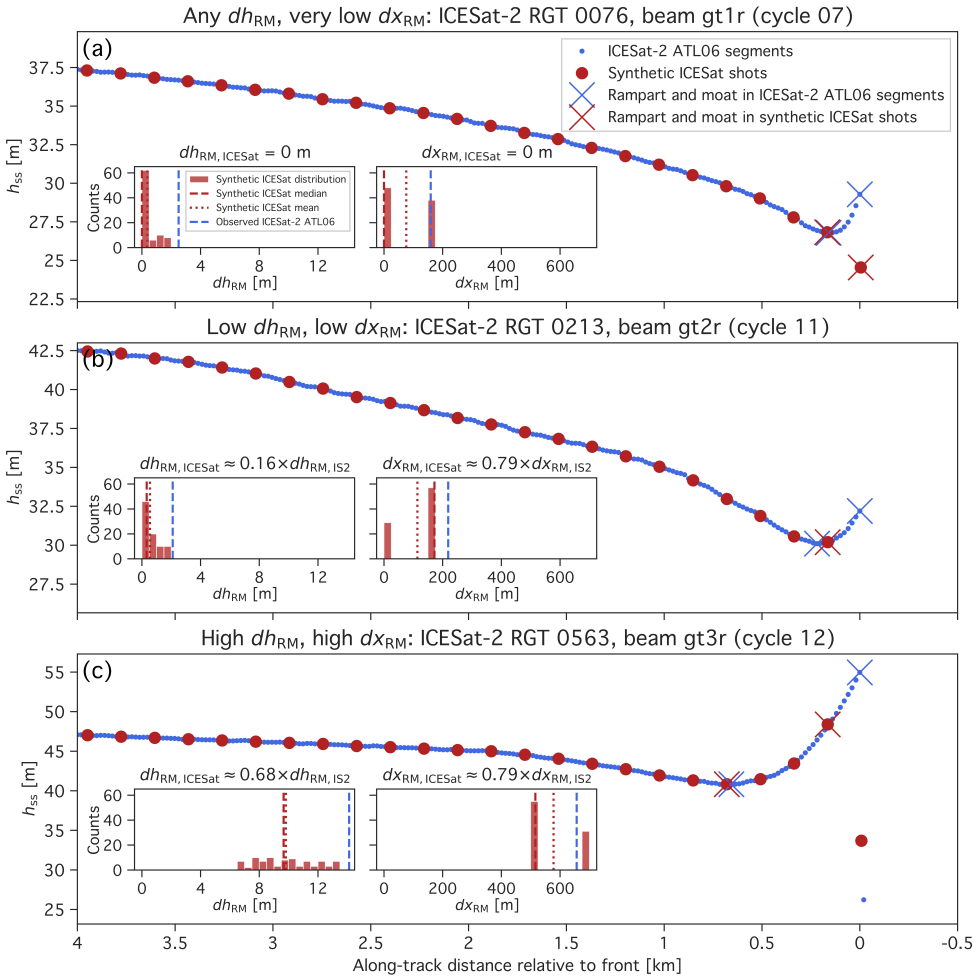

Figure 4.6: Example synthetic ICESat profiles (large red dots, with rampart and moat locations marked as red crosses) derived from the ICESat-2 ATL06 GT profiles (small blue dots, with rampart and moat locations marked as blue crosses) selected as the (a) any dh_{RM}, very low dx_{RM}, (b) low dh_{RM}, low dx_{RM}, and (c) high dh_{RM}, high dx_{RM}, case studies. We generated the three synthetic ICESat profiles using an offset value of zero for the center of the bins across which we averaged the ATL06 segment heights; for the synthetic ICESat profile in (b), this meant that the rampart point is out of the frame and on the front face. (See Figure 4.5 for its location.) Insets in each panel show the distributions of the 86 possible synthetic ICESat values of dh_{RM} and dx_{RM} (red bars), the medians (dashed red lines) and means (dotted red lines) of the distributions, and the corresponding observed ATL06 values (dashed blue lines). Scale factors relating the medians of the synthetic ICESat distributions to the ATL06-derived values are above the distributions.

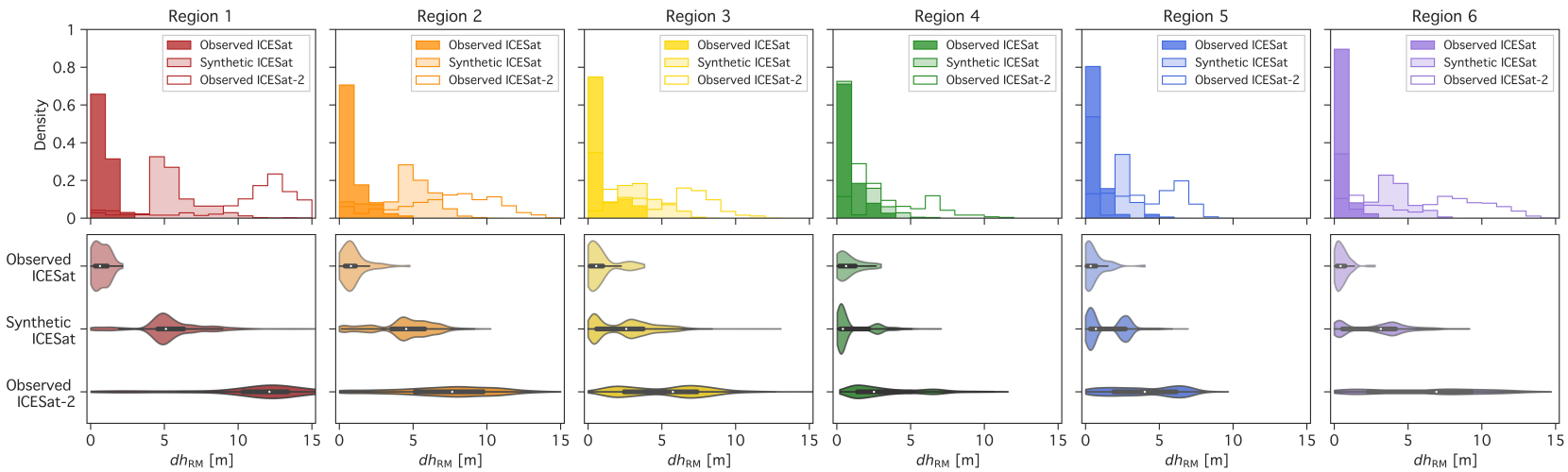

Figure 4.7: (top row) Observed ICESat (dark-shaded bars), synthetic ICESat (light-shaded bars), and observed ICESat-2 (unfilled bars) density histograms of dh_{RM} for each of the six regions of the front. (bottom row) Violin plots of (from top to bottom) observed ICESat, synthetic ICESat, and observed ICESat-2 dh_{RM} for each of the six regions of the front.

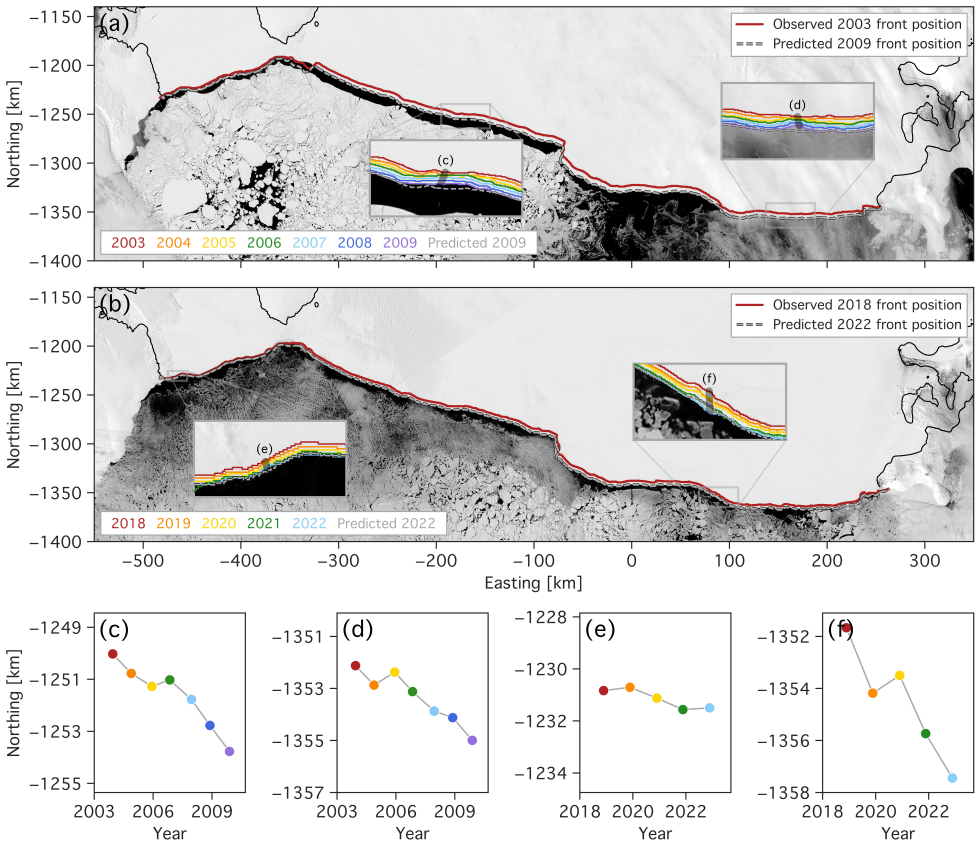

Figure 4.8: (a) Predicted RIS front position for November 22, 2009 (dashed gray line), i.e., approximately a month after the end of the final ICESat laser operational period, derived from the advection of a December 2003 front position (solid red line), traced from MODIS imagery. We advected this position using velocities from a composite (Greene et al., 2022) of NASA Making Earth System data records for Use in Research Environments (MEaSUREs) ITS_LIVE (Gardner et al., 2022) and MEaSUREs InSAR-based velocity data (Rignot et al., 2011b, 2017; Mouginot et al., 2012, 2017). The true and predicted front positions are superimposed on a MODIS image from November 22, 2009, downloaded from NASA Worldview, to enable their comparison for that date. The thin black line indicates the Depoorter et al. (2013) RIS mask. The projection is Antarctic Polar Stereographic with a standard latitude of 71°S and a standard longitude of 0°. (b) Same as (a), but for November 24, 2022, i.e., just over four years after ICESat-2 began collecting data, via the advection of a November 2018 front position. Insets show (a) 2003–2009 and (b) 2018–2022 annual front positions, also traced from late-year MODIS imagery, and (a) 2009 and (b) 2022 predicted front positions (legend in bottom left) for regions where the predicted front position is seaward of the observed front position and/or a scalloped front shape suggests the removal of ice via small-scale calving. (c)–(f) Time series of the northing of the front position for four specific transects (shaded boxes in insets in (a) and (b)), that are roughly aligned with local ice velocity.

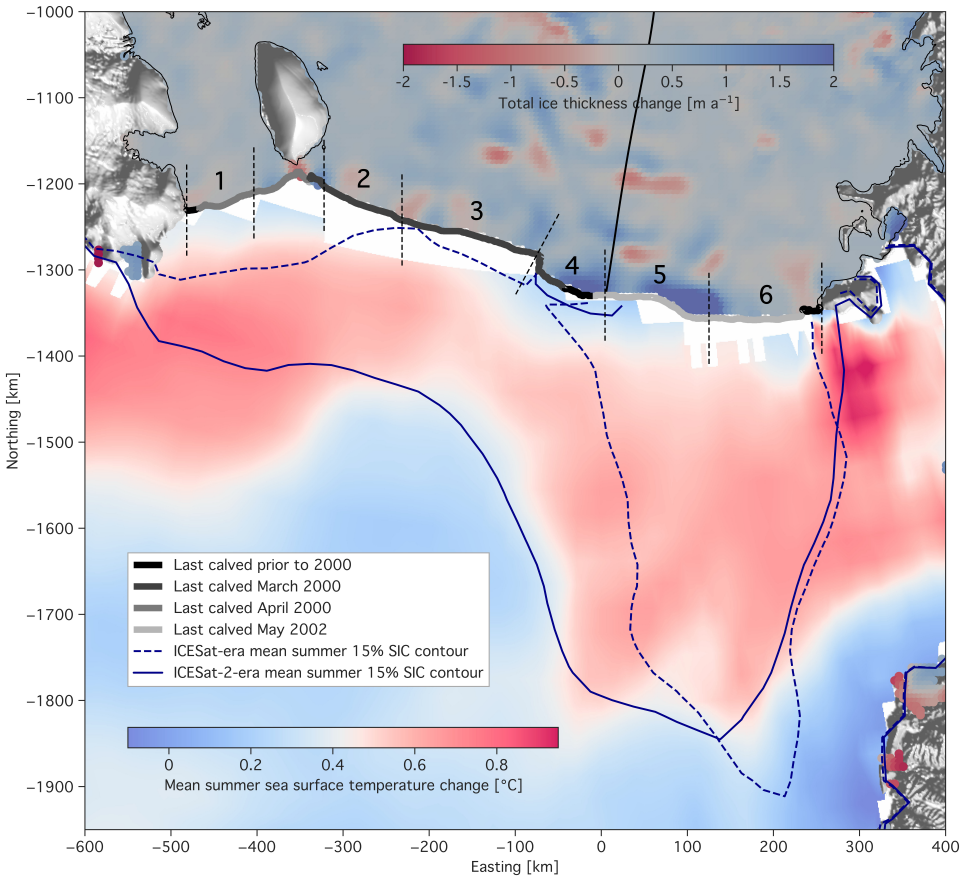

Figure 4.9: Potential factors in R-M evolution along the RIS front during the ICESat and ICESat-2 eras. Ice-shelf background (in darkened blue–red shading) is the unfiltered map of total ice-shelf thickness change rates for 2003–2019 from Smith, Fricker, Gardner, Medley, et al. (2020), superimposed onto the hill-shaded REMA mosaic. Time since major calving event is indicated by the shaded dots along the front. The change in mean summertime sea surface temperature (Hersbach et al., 2023) between the summers before and during the ICESat (December 1999–February 2000 to December 2009–February 2010) and ICESat-2 (December 2014–February 2015 to December 2020–February 2021) missions is shown by blue–red shading. Dashed and solid blue lines show the mean summertime 15% sea ice concentration contour (Meier et al., 2021) for the same ICESat and ICESat-2 periods, respectively. The region locations, RIS mask, and boundary streamline between shelf ice from the West and East Antarctic ice sheets are as in Figure 4.2a. The projection is Antarctic Polar Stereographic with a standard latitude of 71°S and a standard longitude of 0°.

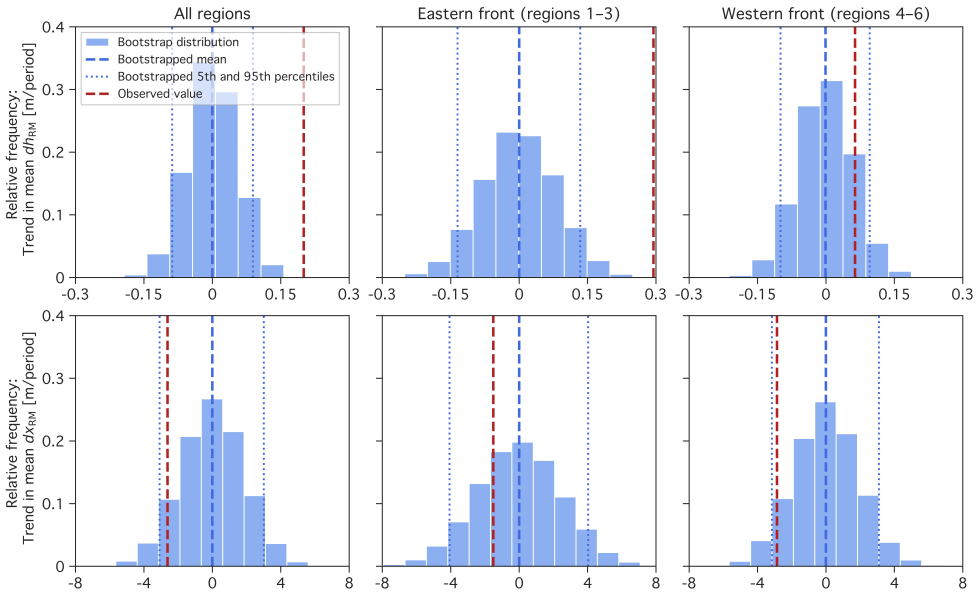

Figure 4.S1: Comparison of ICESat-2-era trends in observed and bootstrapped mean dh_{RM} (top) and dx_{RM} (bottom) values for the full (left), eastern (middle), and western (right) front. For each region and R-M characteristic, the observed trend value is indicated with a dashed red line, and all bootstrapped statistics (the relative frequency histogram of 10,000 simulated trend values and the mean, 5th percentile, and 95th percentile of the distribution) are in blue. Trend values are reported in m per ∼year-long time period, with the four time periods defined as in Figure 4.3.

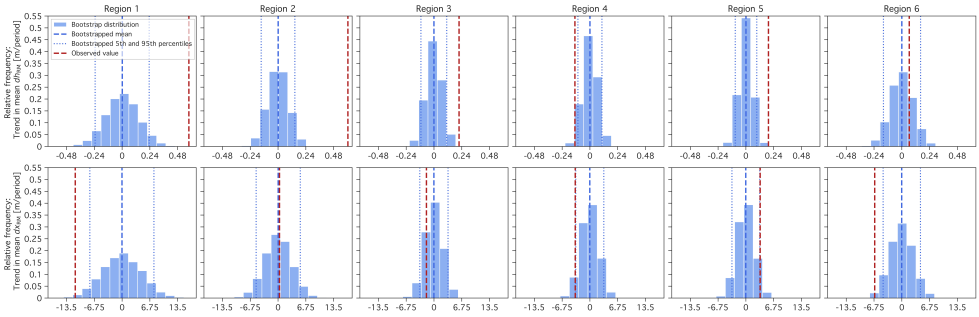

Figure 4.S2: Same as Figure 4.S1, but for the six regions of the RIS front.

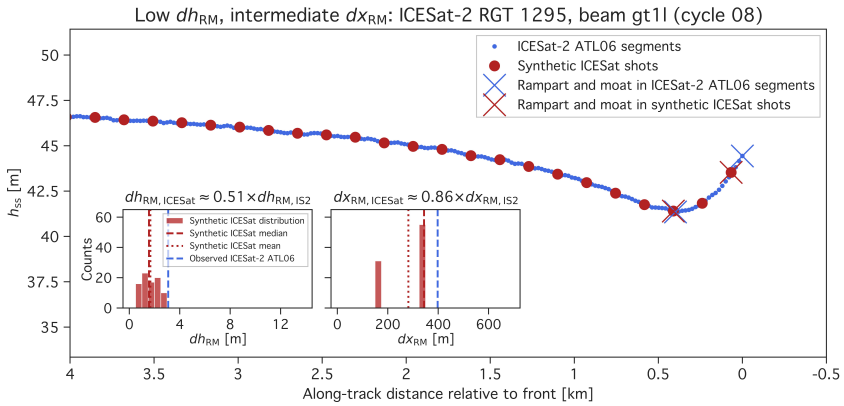

Figure 4.S3: Example synthetic ICESat profile (large red dots, with rampart and moat locations marked as red crosses) derived from the ICESat-2 ATL06 GT profile (small blue dots, with rampart and moat locations marked as blue crosses) selected as the low dh_{RM}, intermediate dx_{RM}, case study. We generated the synthetic ICESat profile using an offset value of zero for the center of the bins across which we averaged the ATL06 segment heights. Insets show the distributions of the 86 possible synthetic ICESat values of dh_{RM} and dx_{RM} (red bars), the medians (dashed red lines) and means (dotted red lines) of the distributions, and the corresponding observed ATL06 values (dashed blue lines). Scale factors relating the medians of the synthetic ICESat distributions to the ATL06-derived values are above the distributions.

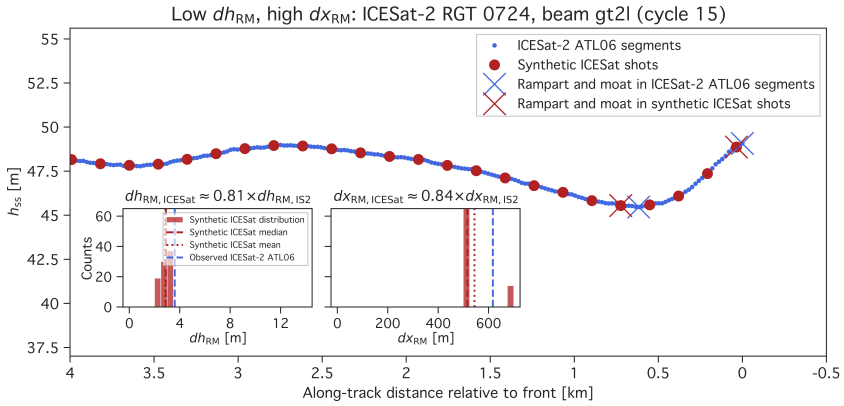

Figure 4.S4: Same as Figure 4.S3, but for the low dh_{RM}, high dx_{RM}, case study.

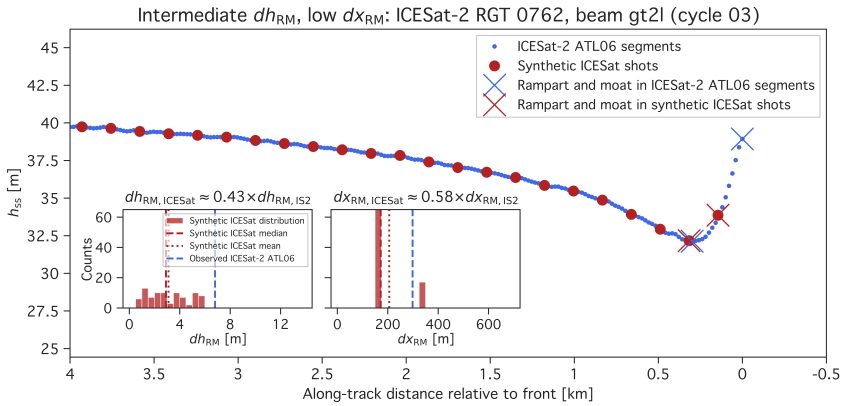

Figure 4.S5: Same as Figure 4.S3, but for the intermediate dh_{RM}, low dx_{RM}, case study.

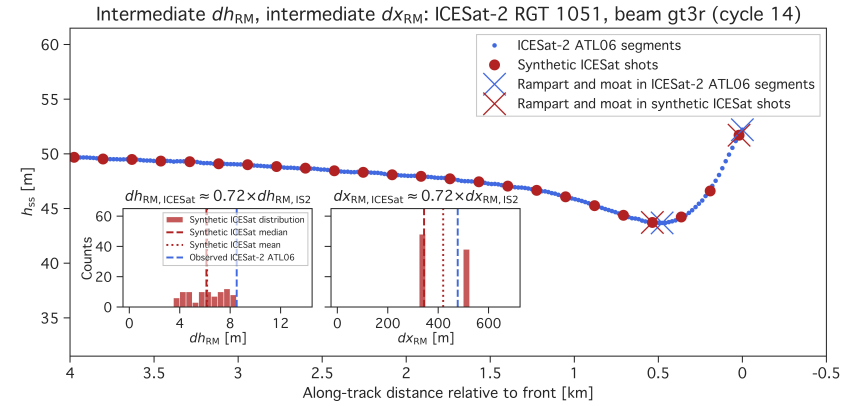

Figure 4.S6: Same as Figure 4.S3, but for the intermediate dh_{RM}, intermediate dx_{RM}, case study.

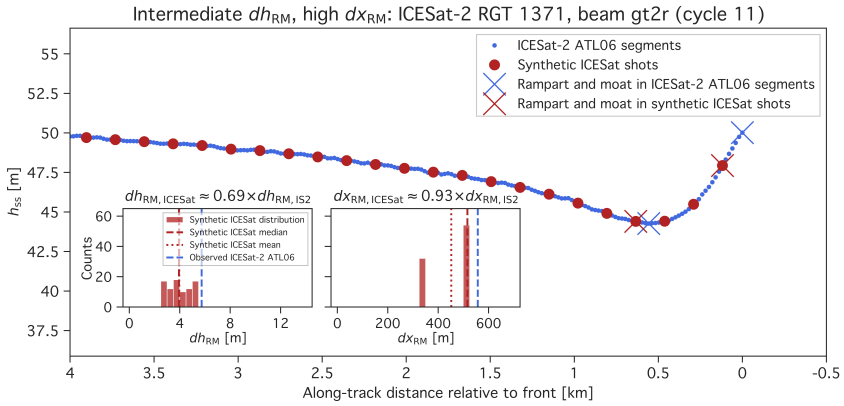

Figure 4.S7: Same as Figure 4.S3, but for the intermediate dh_{RM}, high dx_{RM}, case study.

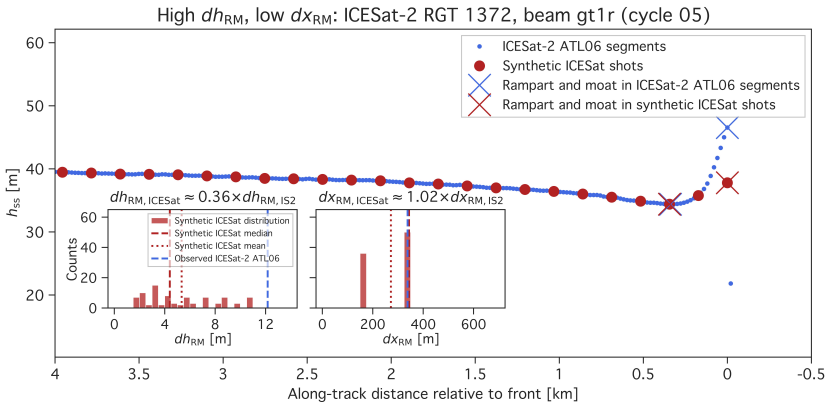

Figure 4.S8: Same as Figure 4.S3, but for the high dh_{RM}, low dx_{RM}, case study.

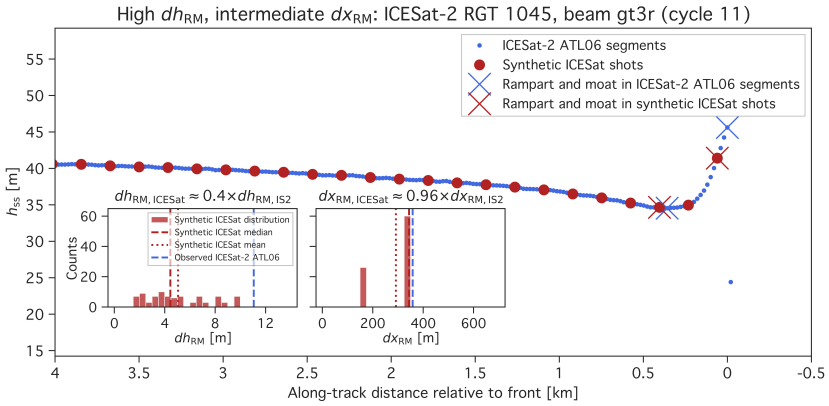

Figure 4.S9: Same as Figure 4.S3, but for the high dh_{RM}, intermediate dx_{RM}, case study.

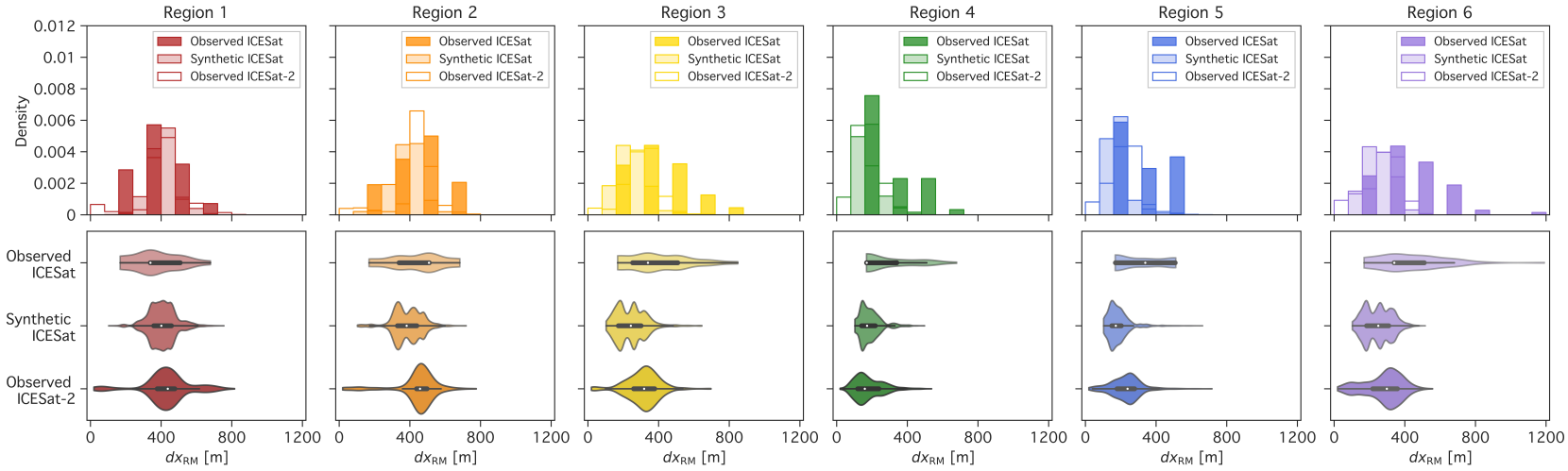

Figure 4.S10: Same as Figure 4.7, but for dx_{RM}.

Chapter 5

Conclusions

5.1 Major contributions of the dissertation

The overarching objective of this dissertation was to expand our knowledge of mass-balance processes on Antarctica's Ross Ice Shelf (RIS) that are driven by interactions with the ocean. The primary data sources in this dissertation were laser altimetry from NASA's Ice, Cloud, and land Elevation Satellite-2 (ICESat-2) mission (2018–present) and aerogeophysical data from the Ross Ocean and ice Shelf Environment, and Tectonic setting Through Aerogeophysical surveys and modeling (ROSETTA-Ice) project (2015–2017). I designed the research in this dissertation around four sets of research questions. I summarize the contributions that my coauthors and I made toward answering each question below.

5.1.1 Research question 1: Can we confirm the presence and spatial distribution of basal marine ice on RIS?

In **Chapter 2**, we calculated the difference between hydrostatic heights and thicknesses estimated from (1) ICESat-2 altimetry and (2) ROSETTA-Ice radio-echo sounding data to explore where basal marine ice may exist on RIS. The thicknesses from ICESat-2 were $>$50 m greater than

those from airborne radar (with >40 m uncertainties at 95% confidence intervals) in an along-flow band that begins southwest of Crary Ice Rise and extends several hundreds of kilometers to the interior of the ice shelf. The radar profiles showed power loss near this band; we assume that this loss is due to the presence of marine ice, which attenuates radar signals. Our results provide ice-shelf-wide estimates of hydrostatic height and thickness differences and allow for a more precise delineation of areas that may have basal marine ice; this represents progress from an earlier attempt to characterize the properties of the RIS base with just airborne radar and point measurements of marine-ice thickness and accretion rates from boreholes. However, our results are limited by large uncertainties, which often exceed the thickness-difference measurements, and errors in the column-averaged ice density. Additional profiles of ice-shelf density from across RIS, as well as improvements to the radar processing methods, are needed to accurately map the basal marine-ice layer from airborne and spaceborne platforms.

5.1.2 Research question 2: Does the near-front shape of the RIS base reflect spatial variability in mode-3 melting?

In the second part of **Chapter 2**, motivated by observations of exponentially increasing melt rates near the RIS front (Horgan et al., 2011), we used 24 ice-shelf thickness profiles upstream of and across the RIS front from the two ROSETTA-Ice radars to describe the topography of the RIS base. We modeled the outer 60 and 10 km of each filtered radar thickness profile with an exponential function and found along-front variability in both the rate parameter of the best-fitting exponential and how well the exponential described the basal topography. The fits were nearly always better for the outer 10 km of the thickness profiles than for the outer 60 km. Generally, for the outer 10 km, the modeled rate parameters were highest and the quality of fit the best for profiles that crossed the RIS front near known areas of "mode-3" melting of the front face and the outermost portion of the ice-shelf base (Jacobs et al., 1992). The modeled thickness profiles near Nascent Iceberg, the only section of the RIS front that has not experienced large-scale iceberg

calving in the 21st century, show relatively shallow thickness gradients in the outer 60 km but do not always fit the observations well. We conclude that the near-front shape of the RIS base does evolve in response to along-front differences in the occurrence and duration of mode-3 melting.

5.1.3 Research question 3: Does the RIS front bend in response to the melting-driven development of a buoyant submerged bench? If so, where and by how much?

In the final part of **Chapter 2**, we presented observations from the ROSETTA-Ice lidar and radar data sets of "rampart-moat" (R-M) surface profiles <1 km from the RIS front. We simulated this deformation using an elastic-beam model with a point buoyancy forcing at one end to represent a submerged bench of ice. This modeling result, in combination with radar evidence of internal-layer deformation that mirrors the surface deformation, suggests that such benches do develop at the RIS front and drive flexure of the outer part of the ice shelf (and possibly calving, as has been observed on icebergs). (I note that the modeling work of Mosbeux et al. (2020), for which I was a coauthor, also furthered our understanding of buoyancy-driven ice-shelf flexure and potential associated calving.)

In **Chapter 3**, we developed an algorithm to locate the ice front in ICESat-2 profiles and search for and describe the key dimensions of R-M structures (namely, the relative height difference, dh_{RM}, and the relative along-track distance difference, dx_{RM}, between the rampart and moat). We applied this algorithm to all ICESat-2 profiles that crossed the RIS front between October 2018 and July 2020. Our results reveal that R-M structures exist along the RIS front, with an average dh_{RM} of 5.4 m, but are larger on the eastern portion of the front. This spatial pattern persisted when we extended the data set to October 2022 and only used strong-beam ICESat-2 profiles (**Chapter 4**); mean dh_{RM} for this longer period was 5.7 m. We attributed the along-front variability to differences in ice thickness and to the summertime sea ice concentration

and upper-ocean heating along the ice front that promote bench development. We also discussed how bench development might interact, codevelop, and compete with mode-3 melting, which occurs in response to similar near-front ocean conditions.

5.1.4 Research question 4: How has buoyancy-driven flexure along the RIS front changed in the early 21st century? How might RIS frontal topography change in the future?

In **Chapter 4**, we applied a slightly modified version of the algorithm developed in **Chapter 3** to examine how bulk R-M characteristics on the RIS front have evolved over the four years of ICESat-2 data acquisition. R-M structures showed a statistically significant increase in dh_{RM}, with the eastern front contributing more to this trend than the western front, and a statistically insignificant change in dx_{RM}. ICESat-2's predecessor, ICESat (2003–2009), was also able to resolve R-M structures but, due to its relatively coarse spatial sampling, typically underestimated dh_{RM}. We downsampled the ICESat-2-derived R-M characteristics to compare them to those derived from ICESat and thus extended our record of R-M structures on the RIS front. This analysis indicated that, on average, R-M structures grew on the eastern front between the ICESat and ICESat-2 eras but shrank on the region of the front encompassing Nascent Iceberg. We proposed that this decrease in dh_{RM} occurred because Nascent Iceberg has not calved in the 21st century, making it relatively more exposed to mode-3 melting. This melting thins the near-front ice, leading to decreased bench volume and, we hypothesize, a reduction in both the bench-driven upward bending moment and R-M growth.

We demonstrated that conditions in the Ross Sea became more favorable for bench development between the ICESat (2003–2009) and ICESat-2 (2018–2022) eras. Projected changes in sea ice concentration (e.g., Bracegirdle et al., 2008) may continue this trend but may also facilitate the possibly competing process of mode-3 melting. R-M-driven calving would

eliminate the associated bench and R-M structure and "reset" bench development. Although we found no direct evidence of this calving in the ICESat-2 repeat-track record, there is a mismatch between observed and predicted ice-front positions during the ICESat and ICESat-2 eras, which implies that there may have been some activity involving small-scale frontal mass loss.

5.2 Future work and outlook

Several observational gaps hinder our ability to fully characterize the processes that affect the mass balance of RIS. Accurate mapping of the fairly modest layer of marine ice that forms on the RIS base will require additional field measurements of vertical and horizontal variations in firn and ice density. Additional ground-based estimates of basal melt rates and ocean observations beneath and in front of the ice shelf (e.g., Stewart et al., 2019), as well as ICESat-2-based estimates of near-front melt rates similar to those provided by Horgan et al. (2011), can better constrain the driving mechanisms, dynamics, and impacts of mode-3 melting on RIS.

I envision multiple avenues of observation- and modeling-based research related to R-M structures. Future efforts should focus on incorporating buoyancy-driven flexure on ice shelves into coupled models used to predict the behavior of the Antarctic Ice Sheet. This is motivated by recent modeling that showed that buoyant calving (albeit due to subaerial slumping) can trigger cliff failure (with possible implications for the marine ice-cliff instability) on slabs of ice with dimensions similar to those of outlet glaciers in Greenland and Thwaites and Pine Island glaciers in Antarctica (Bassis et al., 2021). Observations of R-M-style uplift on some thick glaciers in Greenland suggest that they may be experiencing cliff failure initiated by buoyant calving, but dynamic thinning and small ($\sim$25 kPa) amounts of back stress can stave off runaway collapse. Observations like those presented in this dissertation will be useful for separating the waterline-melting- and slumping-driven components of frontal uplift and buoyant calving in the context of ice-cliff dynamics.

ICESat-2 is unrivaled in its capacity to resolve R-M structures, underscoring the importance of continued support for satellite missions that provide dense coverage over polar regions. Outstanding questions about how R-M structures evolve will require continued monitoring and modeling. One such question is the relationship between dh_{RM} and dx_{RM} on RIS. The ICESat-2 data set indicates that the upper limit of dh_{RM} increases linearly with increasing dx_{RM} and that dx_{RM} itself does not extend past an upper value (Figure 5.1). This envelope is most pronounced on the western RIS front (regions 4–6). While the regional differences in this relationship could result from the varying environmental drivers discussed in **chapters 3 and 4**, they may also reflect along-front differences in ice-shelf rheology and density, again highlighting the need for additional density measurements. Ice-shelf rheology appears to be a critical factor in the size and frequency of R-M-driven calving (Mosbeux et al., 2020). In addition, one element that is missing from our simple elastic-beam model and the frameworks used by Mosbeux et al. (2020) is the contribution of thermally driven flexure, caused by warming of the lower ice shelf, to R-M structure development.

Direct observations of the submerged bench itself will also enhance our understanding of buoyancy-driven flexure, allowing for validation and improved representations of bench dimensions in ice-shelf models. ICESat-2 may be able to provide such observations, as its 532 nm wavelength allows for penetration through up to $\sim$40 m of water (Parrish et al., 2019) and reflection from a secondary surface, such as the ice surface beneath supraglacial melt ponds (Fricker et al., 2021). Relevant field measurements might include subsurface multibeam sonar observations of the bench acquired with pole-mounted (e.g., Fried et al., 2015; Sutherland et al., 2019) or autonomous systems. These data are especially informative when accompanied by multiple upper-ocean temperature profiles (e.g., Wagner et al., 2014).

Our altimetry-based technique for investigating buoyancy-driven flexure should also be extended to other ice shelves in Antarctica and the remaining ice shelves in Greenland and continued on marine-terminating glaciers and icebergs. Large icebergs appear to be particularly

susceptible to calving and breakup via buoyancy-driven flexure (England et al., 2020). In Antarctica, efforts should be focused on regions of ice-shelf fronts that play an active role in buttressing grounded ice (Fürst et al., 2016; Reese et al., 2018). To clarify the relationship between R-M development and mode-3 melting, we suggest first targeting the fronts of Filchner-Ronne and Amery ice shelves, which, like RIS, experience significant frontal melting. However, quantifying flexure on ice shelves that lose mass predominantly via "mode-2" melting could also shed light on the role of mode-3 melting in bench formation and persistence. Ideally, these analyses would be accompanied by observations of the vertical distribution of ocean heat (especially in the upper ocean) just offshore of the ice-shelf fronts, similar to those documented by Porter et al. (2019).

A key takeaway from this research is the ability of modern satellite laser altimetry data—particularly those data from ICESat-2—to resolve small-scale ice-shelf mass-balance processes that had previously only been theorized to occur and/or whose elevation signals are too small to have been resolved by earlier altimeters. The utility of ICESat-2 will only increase as its time series continues. Future advances in satellite laser altimetry resolution and technology will improve spatial and temporal coverage and our ability to monitor changes in ocean-driven ice-shelf processes.

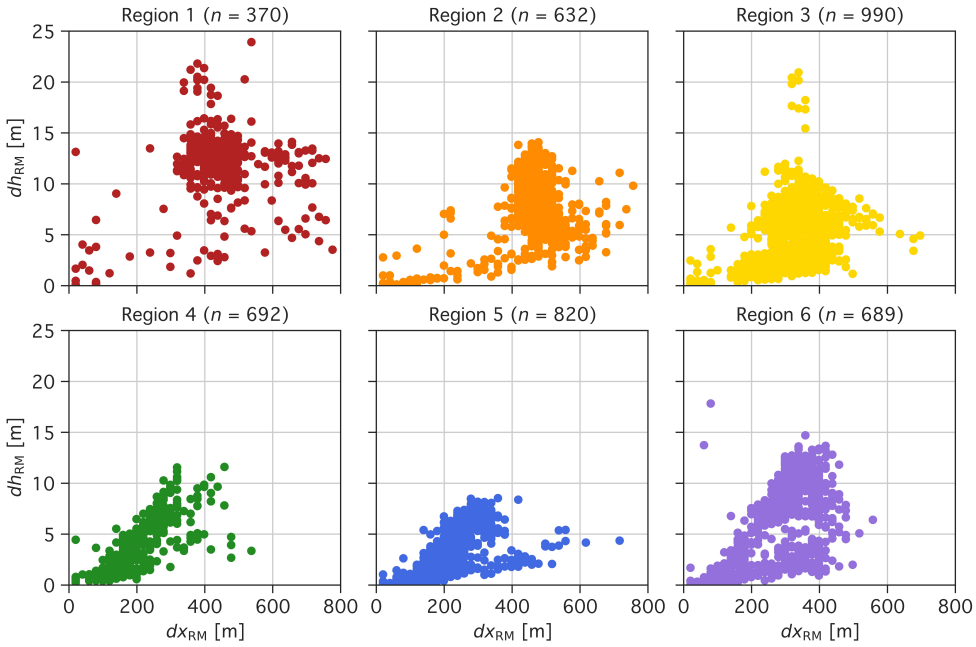

Figure 5.1: Scatterplots of rampart-moat (R-M) structure relative height differences (dh_{RM}) versus length scales (dx_{RM}), derived from strong-beam Ice, Cloud, and land Elevation Satellite-2 (ICESat-2) profiles between October 14, 2018, and October 12, 2022, for each of the six regions of the Ross Ice Shelf front delineated in **Chapter 4** of this dissertation. In the title for each regional panel, n denotes the number of ICESat-2 profiles with R-M structures included in the analysis.

References

Abdalla, S., Kolahchi, A. A., Ablain, M., Adusumilli, S., Bhowmick, S. A., Alou-Font, E., Amarouche, L., Andersen, O. B., Antich, H., Aouf, L., Arbic, B., Armitage, T., Arnault, S., Artana, C., Aulicino, G., Ayoub, N., Badulin, S., Baker, S., Banks, C., Bao, L., Barbetta, S., Barceló-Llull, B., Barlier, F., Basu, S., Bauer-Gottwein, P., Becker, M., Beckley, B., Bellefond, N., Belonenko, T., Benkiran, M., Benkouider, T., Bennartz, R., Benveniste, J., Bercher, N., Berge-Nguyen, M., Bettencourt, J., Blarel, F., Blazquez, A., Blumstein, D., Bonnefond, P., Borde, F., Bouffard, J., Boy, F., Boy, J.-P., Brachet, C., Brasseur, P., Braun, A., Brocca, L., Brockley, D., Brodeau, L., Brown, S., Bruinsma, S., Bulczak, A., Buzzard, S., Cahill, M., Calmant, S., Calzas, M., Camici, S., Cancet, M., Capdeville, H., Carabajal, C. C., Carrere, L., Cazenave, A., Chassignet, E. P., Chauhan, P., Cherchali, S., Chereskin, T., Cheymol, C., Ciani, D., Cipollini, P., Cirillo, F., Cosme, E., Coss, S., Cotroneo, Y., Cotton, D., Couhert, A., Coutin-Faye, S., Crétaux, J.-F., Cyr, F., d'Ovidio, F., Darrozes, J., David, C., Dayoub, N., Staerke, D. D., Deng, X., Desai, S., Desjonqueres, J.-D., Dettmering, D., Bella, A. D., Díaz-Barroso, L., Dibarboure, G., Dieng, H. B., Salvatore Dinardo and, H. D., Dodet, G., Doglioli, A., Domeneghetti, A., Donahue, D., Dong, S., Donlon, C., Dorandeu, J., Drezen, C., Drinkwater, M., Penhoat, Y. D., Dushaw, B., Egido, A., Erofeeva, S., Escudier, P., Esselborn, S., Exertier, P., Fablet, R., Falco, C., Farrell, S. L., Faugere, Y., Femenias, P., Fenoglio, L., Fernandes, J., Fernández, J. G., Ferrage, P., Ferrari, R., Fichen, L., Filippucci, P., Flampouris, S., Fleury, S., Fornari, M., Forsberg, R., Frappart, F., laure Frery, M., Garcia, P., Garcia-Mondejar, A., Gaudelli, J., Gaultier, L., Getirana, A., Gibert, F., Gil, A., Gilbert, L., Gille, S., Giulicchi, L., Gómez-Enri, J., Gómez-Navarro, L., Gommenginger, C., Gourdeau, L., Griffin, D., Groh, A., Guerin, A., Guerrero, R., Guinle, T., Gupta, P., Gutknecht, B. D., Hamon, M., Han, G., Hauser, D., Helm, V., Hendricks, S., Hernandez, F., Hogg, A., Horwath, M., Idžanović, M., Janssen, P., Jeansou, E., Jia, Y., Jia, Y., Jiang, L., Johannessen, J. A., Kamachi, M., Karimova, S., Kelly, K., Kim, S. Y., King, R., Kittel, C. M., Klein, P., Klos, A., Knudsen, P., Koenig, R., Kostianoy, A., Kouraev, A., Kumar, R., Labroue, S., Lago, L. S., Lambin, J., Lasson, L., Laurain, O., Laxenaire, R., Lázaro, C., Gac, S. L., Sommer, J. L., Traon, P.-Y. L., Lebedev, S., Léger, F., Legresy, B., Lemoine, F., Lenain, L., Leuliette, E., Levy, M., Lillibridge, J., Liu, J., Llovel, W., Lyard, F., Macintosh, C., Varona, E. M., Manfredi, C., Marin, F., Mason, E., Massari, C., Mavrocordatos, C., Maximenko, N., McMillan, M., Medina, T., Melet, A., Meloni, M., Mertikas, S., Metref, S., Meyssignac, B., Minster, J.-F., Moreau, T., Moreira, D., Morel, Y., Morrow, R., Moyard, J., Mulet, S., Naeije, M., Nerem, R. S., Ngodock, H., Nielsen,

K., Øie Nilsen, J. E., Niño, F., Loddo, C. N., Noûs, C., Obligis, E., Otosaka, I., Otten, M., Ozbahceci, B. O., Raj, R. P., Paiva, R., Paniagua, G., Paolo, F., Paris, A., Pascual, A., Passaro, M., Paul, S., Pavelsky, T., Pearson, C., Penduff, T., Peng, F., Perosanz, F., Picot, N., Piras, F., Poggiali, V., Poirier, E., de León, S. P., Prants, S., Prigent, C., Provost, C., Pujol, M.-I., Qiu, B., Quilfen, Y., Rami, A., Raney, R. K., Raynal, M., Remy, E., Rémy, F., Restano, M., Richardson, A., Richardson, D., Ricker, R., Ricko, M., Rinne, E., Rose, S. K., Rosmorduc, V., Rudenko, S., Ruiz, S., Ryan, B. J., Salaün, C., Sanchez-Roman, A., Sørensen, L. S., Sandwell, D., Saraceno, M., Scagliola, M., Schaeffer, P., Scharffenberg, M. G., Scharroo, R., Schiller, A., Schneider, R., Schwatke, C., Scozzari, A., Ser-giacomi, E., Seyler, F., Shah, R., Sharma, R., Shaw, A., Shepherd, A., Shriver, J., Shum, C., Simons, W., Simonsen, S. B., Slater, T., Smith, W., Soares, S., Sokolovskiy, M., Soudarin, L., Spatar, C., Speich, S., Srinivasan, M., Srokosz, M., Stanev, E., Staneva, J., Steunou, N., Stroeve, J., Su, B., Sulistioadi, Y. B., Swain, D., Sylvestre-baron, A., Taburet, N., Tailleux, R., Takayama, K., Tapley, B., Tarpanelli, A., Tavernier, G., Testut, L., Thakur, P. K., Thibaut, P., Thompson, L., Tintoré, J., Tison, C., Tourain, C., Tournadre, J., Townsend, B., Tran, N., Trilles, S., Tsamados, M., Tseng, K.-H., Ubelmann, C., Uebbing, B., Vergara, O., Verron, J., Vieira, T., Vignudelli, S., Shiffer, N. V., Visser, P., Vivier, F., Volkov, D., von Schuckmann, K., Vuglinskii, V., Vuilleumier, P., Walter, B., Wang, J., Wang, C., Watson, C., Wilkin, J., Willis, J., Wilson, H., Woodworth, P., Yang, K., Yao, F., Zaharia, R., Zakharova, E., Zaron, E. D., Zhang, Y., Zhao, Z., Zinchenko, V., & Zlotnicki, V. (2021). Altimetry for the future: Building on 25 years of progress. *Advances in Space Research*, *68*(2), 319–363. doi: 10.1016/j.asr.2021.01.022

Abram, N., Gattuso, J.-P., Prakash, A., Cheng, L., Chidichimo, M. P., Crate, S., Enomoto, H., Garschagen, M., Gruber, N., Harper, S., Holland, E., Kudela, R. M., Rice, J., Steffen, K., & von Schuckmann, K. (2019). Framing and context of the report. In H.-O. Pörtner, D. C. Roberts, V. Masson-Delmotte, P. Zhai, M. Tignor, E. Poloczanska, K. Mintenbeck, A. Alegría, M. Nicolai, A. Okem, J. Petzold, B. Rama, & N. M. Weyer (Eds.), *IPCC Special Report on the Ocean and Cryosphere in a Changing Climate* (pp. 73–129). Cambridge University Press. doi: 10.1017/9781009157964.003

Adusumilli, S., Fricker, H. A., Medley, B., Padman, L., & Siegfried, M. R. (2020). Interannual variations in meltwater input to the Southern Ocean from Antarctic ice shelves. *Nature Geoscience*, *13*(9), 616–620. doi: 10.1038/s41561-020-0616-z

Andersen, O., Knudsen, P., & Stenseng, L. (2015). The DTU13 MSS (mean sea surface) and MDT (mean dynamic topography) from 20 years of satellite altimetry. In S. Jin & R. Barzaghi (Eds.), *IGFS 2014, International Association of Geodesy Symposia* (Vol. 144, pp. 111–121). Springer. doi: 10.1007/1345_2015_182

Anderson, J. B., Conway, H., Bart, P. J., Witus, A. E., Greenwood, S. L., McKay, R. M., Hall, B. L., Ackert, R. P., Licht, K., Jakobsson, M., & Stone, J. O. (2014). Ross Sea paleo-ice sheet drainage and deglacial history during and since the LGM. *Quaternary Science Reviews*, *100*, 31–54. doi: 10.1016/j.quascirev.2013.08.020

Armstrong McKay, D. I., Staal, A., Abrams, J. F., Winkelmann, R., Sakschewski, B., Loriani, S., Fetzer, I., Cornell, S. E., Rockström, J., & Lenton, T. M. (2022). Exceeding 1.5°C global warming could trigger multiple climate tipping points. *Science*, *377*(6611), eabn7950. doi: 10.1126/science.abn7950

Arzeno, I. B., Beardsley, R. C., Limeburner, R., Owens, B., Padman, L., Springer, S. R., Stewart, C. L., & Williams, M. J. M. (2014). Ocean variability contributing to basal melt rate near the ice front of Ross Ice Shelf, Antarctica. *Journal of Geophysical Research: Oceans*, *119*(7), 4214–4233. doi: 10.1002/2014JC009792

Barnard, P. L., Erikson, L. H., Foxgrover, A. C., Finzi Hart, J. A., Limber, P., O'Neill, A. C., van Ormondt, M., Vitousek, S., Wood, N., Hayden, M. K., & Jones, J. M. (2019). Dynamic flood modeling essential to assess the coastal impacts of climate change. *Scientific Reports*, *9*(1), 4309. doi: 10.1038/s41598-019-40742-z

Bassis, J. N., Berg, B., Crawford, A. J., & Benn, D. I. (2021). Transition to marine ice cliff instability controlled by ice thickness gradients and velocity. *Science*, *372*(6548), 1342–1344. doi: 10.1126/science.abf6271

Bassis, J. N., & Walker, C. C. (2012). Upper and lower limits on the stability of calving glaciers from the yield strength envelope of ice. *Proceedings of the Royal Society A: Mathematical, Physical and Engineering Sciences*, *468*(2140), 913–931. doi: 10.1098/rspa.2011.0422

Baumhoer, C. A., Dietz, A. J., Kneisel, C., Paeth, H., & Kuenzer, C. (2021). Environmental drivers of circum-Antarctic glacier and ice shelf front retreat over the last two decades. *The Cryosphere*, *15*(5), 2357–2381. doi: 10.5194/tc-15-2357-2021

Becker, M. K., Howard, S. L., Fricker, H. A., Padman, L., Mosbeux, C., & Siegfried, M. R. (2021). Buoyancy-driven flexure at the front of Ross Ice Shelf, Antarctica, observed with ICESat-2 laser altimetry. *Geophysical Research Letters*, *48*(12), e2020GL091207. doi: 10.1029/2020GL091207

Bentley, C. R. (1990). The Ross Ice Shelf Geophysical and Glaciological Survey (RIGGS): Introduction and summary of measurements performed. In C. R. Bentley & D. E. Hayes (Eds.), *The Ross Ice Shelf: Glaciology and Geophysics* (pp. 1–20). Wiley Online Library. doi: 10.1029/AR042p0001

Blindow, N. (1994). The central part of the Filchner-Ronne Ice Shelf, Antarctica: Internal structures revealed by 40MHz monopulse RES. *Annals of Glaciology*, *20*, 365–371. doi: 10.3189/1994AoG20-1-365-371

Boghosian, A. L., Pratt, M. J., Becker, M. K., Cordero, S. I., Dhakal, T., Kingslake, J., Locke, C. D., Tinto, K. J., & Bell, R. E. (2019). Inside the ice shelf: Using augmented reality to visualise 3D lidar and radar data of Antarctica. *The Photogrammetric Record*, *34*(168), 346–364. doi: 10.1111/phor.12298

Borsa, A. A., Moholdt, G., Fricker, H. A., & Brunt, K. M. (2014). A range correction for ICESat and its potential impact on ice-sheet mass balance studies. *The Cryosphere*, *8*(2), 345–357. doi: 10.5194/tc-8-345-2014

Bracegirdle, T. J., Connolley, W. M., & Turner, J. (2008). Antarctic climate change over the twenty first century. *Journal of Geophysical Research: Atmospheres*, *113*(D3), D03103. doi: 10.1029/2007JD008933

Briese, C., Pfennigbauer, M., Lehner, H., Ullrich, A., Wagner, W., & Pfeifer, N. (2012). Radiometric calibration of multi-wavelength airborne laser scanning data. *ISPRS Annals of the Photogrammetry, Remote Sensing and Spatial Information Sciences*, *I-7*, 335–340. doi: 10.5194/isprsannals-I-7-335-2012

Bromirski, P. D., Sergienko, O. V., & MacAyeal, D. R. (2010). Transoceanic infragravity waves impacting Antarctic ice shelves. *Geophysical Research Letters*, *37*(2), L02502. doi: 10.1029/2009GL041488

Brunt, K. M., Neumann, T. A., & Smith, B. E. (2019). Assessment of ICESat-2 ice sheet surface heights, based on comparisons over the interior of the Antarctic Ice Sheet. *Geophysical Research Letters*, *46*(22), 13072–13078. doi: 10.1029/2019GL084886

Brunt, K. M., Okal, E. A., & MacAyeal, D. R. (2011). Antarctic ice-shelf calving triggered by the Honshu (Japan) earthquake and tsunami, March 2011. *Journal of Glaciology*, *57*(205), 785–788. doi: 10.3189/002214311798043681

Carter, S. P., Blankenship, D. D., Young, D. A., & Holt, J. W. (2009). Using radar-sounding data to identify the distribution and sources of subglacial water: Application to Dome C, East Antarctica. *Journal of Glaciology*, *55*(194), 1025–1040. doi: 10.3189/002214309790794931

Castagno, P., Capozzi, V., DiTullio, G. R., Falco, P., Fusco, G., Rintoul, S. R., Spezie, G., & Budillon, G. (2019). Rebound of shelf water salinity in the Ross Sea. *Nature Communications*, *10*(1), 5441. doi: 10.1038/s41467-019-13083-8

Cook, S., Galton-Fenzi, B. K., Ligtenberg, S. R. M., & Coleman, R. (2018). Brief communication: Widespread potential for seawater infiltration on Antarctic ice shelves. *The Cryosphere*, *12*(12), 3853–3859. doi: 10.5194/tc-12-3853-2018

Craven, M., Allison, I., Fricker, H. A., & Warner, R. (2009). Properties of a marine ice layer under the Amery Ice Shelf, East Antarctica. *Journal of Glaciology*, *55*(192), 717–728. doi: 10.3189/002214309789470941

Das, I., Padman, L., Bell, R. E., Fricker, H. A., Tinto, K. J., Hulbe, C. L., Siddoway, C. S., Dhakal, T., Frearson, N. P., Mosbeux, C., Cordero, S. I., & Siegfried, M. R. (2020). Multidecadal basal melt rates and structure of the Ross Ice Shelf, Antarctica, using airborne ice penetrat-

ing radar. *Journal of Geophysical Research: Earth Surface*, *125*(3), e2019JF005241. doi: 10.1029/2019JF005241

DeConto, R. M., & Pollard, D. (2016). Contribution of Antarctica to past and future sea-level rise. *Nature*, *531*(7596), 591–597. doi: 10.1038/nature17145

Deems, J. S., Painter, T. H., & Finnegan, D. C. (2013). Lidar measurement of snow depth: A review. *Journal of Glaciology*, *59*(215), 467–479. doi: 10.3189/2013JoG12J154

Depoorter, M. A., Bamber, J. L., Griggs, J. A., Lenaerts, J. T. M., Ligtenberg, S. R. M., van den Broeke, M. R., & Moholdt, G. (2013). Calving fluxes and basal melt rates of Antarctic ice shelves. *Nature*, *502*(7469), 89–92. doi: 10.1038/nature12567

Dinniman, M. S., Klinck, J. M., & Smith Jr, W. O. (2011). A model study of Circumpolar Deep Water on the West Antarctic Peninsula and Ross Sea continental shelves. *Deep Sea Research Part II: Topical Studies in Oceanography*, *58*(13–16), 1508–1523. doi: 10.1016/j.dsr2.2010.11.013

Dupont, T. K., & Alley, R. B. (2005). Assessment of the importance of ice-shelf buttressing to ice-sheet flow. *Geophysical Research Letters*, *32*(4), L04503. doi: 10.1029/2004GL022024

Edwards, T. L., Brandon, M. A., Durand, G., Edwards, N. R., Golledge, N. R., Holden, P. B., Nias, I. J., Payne, A. J., Ritz, C., & Wernecke, A. (2019). Revisiting Antarctic ice loss due to marine ice-cliff instability. *Nature*, *566*(7742), 58–64. doi: 10.1038/s41586-019-0901-4

Egbert, G. D., & Erofeeva, S. Y. (2002). Efficient inverse modeling of barotropic ocean tides. *Journal of Atmospheric and Oceanic Technology*, *19*(2), 183–204. doi: 10.1175/1520-0426(2002)019<0183:EIMOBO>2.0.CO;2

England, M. R., Wagner, T. J. W., & Eisenman, I. (2020). Modeling the breakup of tabular icebergs. *Science Advances*, *6*(51), eabd1273. doi: 10.1126/sciadv.abd1273

Fahnestock, M. A., Scambos, T. A., Bindschadler, R. A., & Kvaran, G. (2000). A millennium of variable ice flow recorded by the Ross Ice Shelf, Antarctica. *Journal of Glaciology*, *46*(155), 652–664. doi: 10.3189/172756500781832693

Fox-Kemper, B., Hewitt, H. T., Xiao, C., Aðalgeirsdóttir, G., Drijfhout, S. S., Edwards, T. L., Golledge, N. R., Hemer, M., Kopp, R. E., Krinner, G., Mix, A., Notz, D., Nowicki, S., Nurhati, I. S., Ruiz, L., Sallée, J.-B., Slangen, A. B. A., & Yu, Y. (2021). Ocean, cryosphere and sea level change. In V. Masson-Delmotte, P. Zhai, A. Pirani, S. L. Connors, C. Péan, S. Berger, N. Caud, Y. Chen, L. Goldfarb, M. I. Gomis, M. Huang, K. Leitzell, E. Lonnoy, J. B. R. Matthews, T. K. Maycock, T. Waterfield, O. Yelekçi, R. Yu, & B. Zhou (Eds.), *Climate Change 2021: The Physical Science Basis. Contribution of Working Group I to the Sixth Assessment Report of the Intergovernmental Panel on Climate Change* (pp. 1211–1362). Cambridge University Press. doi: 10.1017/9781009157896.011

Fretwell, P., Pritchard, H. D., Vaughan, D. G., Bamber, J. L., Barrand, N. E., Bell, R., Bianchi, C., Bingham, R., Blankenship, D. D., Casassa, G., Catania, G., Callens, D., Conway, H., Cook, A. J., Corr, H. F. J., Damaske, D., Damm, V., Ferraccioli, F., Forsberg, R., Fujita, S., Gim, Y., Gogineni, P., Griggs, J. A., Hindmarsh, R. C. A., Holmlund, P., Holt, J. W., Jacobel, R. W., Jenkins, A., Jokat, W., Jordan, T., King, E. C., Kohler, J., Krabill, W., Riger-Kusk, M., Langley, K. A., Leitchenkov, G., Leuschen, C., Luyendyk, B. P., Matsuoka, K., Mouginot, J., Nitsche, F. O., Nogi, Y., Nost, O. A., Popov, S. V., Rignot, E., Rippin, D. M., Rivera, A., Roberts, J., Ross, N., Siegert, M. J., Smith, A. M., Steinhage, D., Studinger, M., Sun, B., Tinto, B. K., Welch, B. C., Wilson, D., Young, D. A., Xiangbin, C., & Zirizzotti, A. (2013). Bedmap2: Improved ice bed, surface and thickness datasets for Antarctica. *The Cryosphere*, *7*(1), 375–393. doi: 10.5194/tc-7-375-2013

Fricker, H. A., Arndt, P., Brunt, K. M., Datta, R. T., Fair, Z., Jasinski, M. F., Kingslake, J., Magruder, L. A., Moussavi, M., Pope, A., Spergel, J. J., Stoll, J. D., & Wouters, B. (2021). ICESat-2 meltwater depth estimates: Application to surface melt on Amery Ice Shelf, East Antarctica. *Geophysical Research Letters*, *48*(8), e2020GL090550. doi: 10.1029/2020GL090550

Fricker, H. A., Bassis, J. N., Minster, B., & MacAyeal, D. R. (2005). ICESat's new perspective on ice shelf rifts: The vertical dimension. *Geophysical Research Letters*, *32*(23). doi: 10.1029/2005GL025070

Fricker, H. A., & Padman, L. (2006). Ice shelf grounding zone structure from ICESat laser altimetry. *Geophysical Research Letters*, *33*(15), L15502. doi: 10.1029/2006GL026907

Fricker, H. A., Popov, S., Allison, I., & Young, N. (2001). Distribution of marine ice beneath the Amery Ice Shelf. *Geophysical Research Letters*, *28*(11), 2241–2244. doi: 10.1029/2000GL012461

Fricker, H. A., Young, N. W., Allison, I., & Coleman, R. (2002). Iceberg calving from the Amery Ice Shelf, East Antarctica. *Annals of Glaciology*, *34*, 241–246. doi: 10.3189/172756402781817581

Fried, M. J., Catania, G. A., Bartholomaus, T. C., Duncan, D., Davis, M., Stearns, L. A., Nash, J., Shroyer, E., & Sutherland, D. (2015). Distributed subglacial discharge drives significant submarine melt at a Greenland tidewater glacier. *Geophysical Research Letters*, *42*(21), 9328–9336. doi: 10.1002/2015GL065806

Fujino, K., Lewis, E. L., & Perkin, R. G. (1974). The freezing point of seawater at pressures up to 100 bars. *Journal of Geophysical Research*, *79*(12), 1792–1797. doi: 10.1029/JC079i012p01792

Fürst, J. J., Durand, G., Gillet-Chaulet, F., Tavard, L., Rankl, M., Braun, M., & Gagliardini, O. (2016). The safety band of Antarctic ice shelves. *Nature Climate Change*, *6*(5), 479–482.

doi: 10.1038/nclimate2912

Gardner, A., Fahnestock, M., & Scambos, T. (2022). MEaSUREs ITS_LIVE regional glacier and ice sheet surface velocities (Version 1) [Data set]. *NASA National Snow and Ice Data Center Distributed Active Archive Center*. doi: 10.5067/6II6VW8LLWJ7

Gilardoni, M., Reguzzoni, M., & Sampietro, D. (2016). GECO: A global gravity model by locally combining GOCE data and EGM2008. *Studia Geophysica et Geodaetica*, *60*, 228–247. doi: 10.1007/s11200-015-1114-4

Greene, C. A., Gardner, A. S., Schlegel, N.-J., & Fraser, A. D. (2022). Antarctic calving loss rivals ice-shelf thinning. *Nature*, *609*(7929), 948–953. doi: 10.1038/s41586-022-05037-w

Greene, C. A., Gwyther, D. E., & Blankenship, D. D. (2017). Antarctic Mapping Tools for MATLAB. *Computers & Geosciences*, *104*, 151–157. doi: 10.1016/j.cageo.2016.08.003

Griesel, A., Mazloff, M. R., & Gille, S. T. (2012). Mean dynamic topography in the Southern Ocean: Evaluating Antarctic Circumpolar Current transport. *Journal of Geophysical Research: Oceans*, *117*(C1). doi: 10.1029/2011JC007573

Griggs, J. A., & Bamber, J. L. (2011). Antarctic ice-shelf thickness from satellite radar altimetry. *Journal of Glaciology*, *57*(203), 485–498. doi: 10.3189/002214311796905659

Gudmundsson, G. H., Paolo, F. S., Adusumilli, S., & Fricker, H. A. (2019). Instantaneous Antarctic Ice Sheet mass loss driven by thinning ice shelves. *Geophysical Research Letters*, *46*(23), 13903–13909. doi: 10.1029/2019GL085027

Haran, T., Bohlander, J., Scambos, T., Painter, T., & Fahnestock, M. (2005). MODIS Mosaic of Antarctica 2003–2004 (MOA2004) image map (Version 1) [Data set]. *National Snow and Ice Data Center*. doi: 10.7265/N5ZK5DM5

Hersbach, H., Bell, B., Berrisford, P., Biavati, G., Horányi, A., Muñoz Sabater, J., Nicolas, J., Peubey, C., Radu, R., Rozum, I., Schepers, D., Simmons, A., Soci, C., Dee, D., & Thépaut, J.-N. (2019). ERA5 monthly averaged data on single levels from 1979 to present [Data set]. *Copernicus Climate Change Service (C3S) Climate Data Store (CDS)*. doi: 10.24381/cds.f17050d7

Hersbach, H., Bell, B., Berrisford, P., Biavati, G., Horányi, A., Muñoz Sabater, J., Nicolas, J., Peubey, C., Radu, R., Rozum, I., Schepers, D., Simmons, A., Soci, C., Dee, D., & Thépaut, J.-N. (2023). ERA5 monthly averaged data on single levels from 1940 to present [Data set]. *Copernicus Climate Change Service (C3S) Climate Data Store (CDS)*. doi: 10.24381/cds.f17050d7

Holland, D. M., Jacobs, S. S., & Jenkins, A. (2003). Modelling the ocean circulation beneath the Ross Ice Shelf. *Antarctic Science*, *15*(1), 13–23. doi: 10.1017/S0954102003001019

Holland, P. R., Corr, H. F. J., Vaughan, D. G., Jenkins, A., & Skvarca, P. (2009). Marine ice in Larsen Ice Shelf. *Geophysical Research Letters*, *36*(11). doi: 10.1029/2009GL038162

Horgan, H. J., Walker, R. T., Anandakrishnan, S., & Alley, R. B. (2011). Surface elevation changes at the front of the Ross Ice Shelf: Implications for basal melting. *Journal of Geophysical Research: Oceans*, *116*(C2), C02005. doi: 10.1029/2010JC006192

Horvat, C., Blanchard-Wrigglesworth, E., & Petty, A. (2020). Observing waves in sea ice with ICESat-2. *Geophysical Research Letters*, *47*(10), e2020GL087629. doi: 10.1029/2020GL087629

Howard, S. L., Erofeeva, S., & Padman, L. (2019). CATS2008: Circum-Antarctic Tidal Simulation version 2008 [Data set]. *United States Antarctic Program Data Center*. doi: 10.15784/601235

Howat, I. M., Porter, C., Smith, B. E., Noh, M.-J., & Morin, P. (2019). The Reference Elevation Model of Antarctica. *The Cryosphere*, *13*(2), 665–674. doi: 10.5194/tc-13-665-2019

Hughes, T. (2002). Calving bays. *Quaternary Science Reviews*, *21*(1–3), 267–282. doi: 10.1016/S0277-3791(01)00092-0

IPCC. (2007). *Climate Change 2007: Synthesis Report. Contribution of Working Groups I, II and III to the Fourth Assessment Report of the Intergovernmental Panel on Climate Change* (Core Writing Team, R. K. Pachauri, & A. Reisinger, Eds.). Geneva, Switzerland: Author. doi: 10.1017/CBO9780511546013

Jacobs, S. S., & Giulivi, C. F. (2010). Large multidecadal salinity trends near the Pacific–Antarctic continental margin. *Journal of Climate*, *23*(17), 4508–4524. doi: 10.1175/2010JCLI3284.1

Jacobs, S. S., Giulivi, C. F., & Dutrieux, P. (2022). Persistent Ross Sea freshening from imbalance West Antarctic ice shelf melting. *Journal of Geophysical Research: Oceans*, *127*(3), e2021JC017808. doi: 10.1029/2021JC017808

Jacobs, S. S., Helmer, H. H., Doake, C. S. M., Jenkins, A., & Frolich, R. M. (1992). Melting of ice shelves and the mass balance of Antarctica. *Journal of Glaciology*, *38*(130), 375–387. doi: 10.3189/S0022143000002252

James, T. D., Murray, T., Selmes, N., Scharrer, K., & O'Leary, M. (2014). Buoyant flexure and basal crevassing in dynamic mass loss at Helheim Glacier. *Nature Geoscience*, *7*(8), 593–596. doi: 10.1038/ngeo2204

Jenkins, A., Dutrieux, P., Jacobs, S. S., McPhail, S. D., Perrett, J. R., Webb, A. T., & White, D. (2010). Observations beneath Pine Island Glacier in West Antarctica and implications for its retreat. *Nature Geoscience*, *3*(7), 468–472. doi: 10.1038/ngeo890

Joughin, I., & MacAyeal, D. R. (2005). Calving of large tabular icebergs from ice shelf rift systems. *Geophysical Research Letters*, *32*(2), L02501. doi: 10.1029/2004GL020978

Joughin, I., & Padman, L. (2003). Melting and freezing beneath Filchner-Ronne Ice Shelf, Antarctica. *Geophysical Research Letters*, *30*(9). doi: 10.1029/2003GL016941

Joughin, I., Smith, B. E., & Medley, B. (2014). Marine ice sheet collapse potentially under way for the Thwaites Glacier Basin, West Antarctica. *Science*, *344*(6185), 735–738. doi: 10.1126/science.1249055

Joughin, I., & Vaughan, D. G. (2004). Marine ice beneath the Filchner-Ronne Ice Shelf, Antarctica: A comparison of estimated thickness distributions. *Annals of Glaciology*, *39*, 511–517. doi: 10.3189/172756404781814717

Kingslake, J., Scherer, R. P., Albrecht, T., Coenen, J., Powell, R. D., Reese, R., Stansell, N. D., Tulaczyk, S., Wearing, M. G., & Whitehouse, P. L. (2018). Extensive retreat and re-advance of the West Antarctic Ice Sheet during the Holocene. *Nature*, *558*(7710), 430–434. doi: 10.1038/s41586-018-0208-x

Klein, E., Mosbeux, C., Bromirski, P. D., Padman, L., Bock, Y., Springer, S. R., & Fricker, H. A. (2020). Annual cycle in flow of Ross Ice Shelf, Antarctica: Contribution of variable basal melting. *Journal of Glaciology*, *66*(259), 861–875. doi: 10.1017/jog.2020.61

Kristensen, M. (1983). Iceberg calving and deterioration in Antarctica. *Progress in Physical Geography: Earth and Environment*, *7*(3), 313–328. doi: 10.1177/030913338300700301

Kristensen, M., Squire, V. A., & Moore, S. C. (1982). Tabular icebergs in ocean waves. *Nature*, *297*(5868), 669–671. doi: 10.1038/297669a0

Kulessa, B., Jansen, D., Luckman, A. J., King, E. C., & Sammonds, P. R. (2014). Marine ice regulates the future stability of a large Antarctic ice shelf. *Nature Communications*, *5*(1), 3707. doi: 10.1038/ncomms4707

Lambrecht, A., Sandhäger, H., Vaughan, D. G., & Mayer, C. (2007). New ice thickness maps of Filchner-Ronne Ice Shelf, Antarctica, with specific focus on grounding lines and marine ice. *Antarctic Science*, *19*(4), 521–532. doi: 10.1017/S0954102007000661

Lazzara, M. A., Jezek, K. C., Scambos, T. A., MacAyeal, D. R., & van der Veen, C. J. (1999). On the recent calving of icebergs from the Ross Ice Shelf. *Polar Geography*, *23*(3), 201–212. doi: 10.1080/10889379909377676

Lazzara, M. A., Jezek, K. C., Scambos, T. A., MacAyeal, D. R., & van der Veen, C. J. (2008). On the recent calving of icebergs from the Ross Ice Shelf. *Polar Geography*, *31*(1-2), 15–26. doi: 10.1080/10889370802175937

LeDoux, C. M., Hulbe, C. L., Forbes, M. P., Scambos, T. A., & Alley, K. (2017). Structural provinces of the Ross Ice Shelf, Antarctica. *Annals of Glaciology*, *58*(75pt1), 88–98. doi: 10.1017/aog.2017.24

Lenaerts, J. T. M., Vizcaino, M., Fyke, J., van Kampenhout, L., & van den Broeke, M. R. (2016). Present-day and future Antarctic Ice Sheet climate and surface mass balance in the Community Earth System Model. *Climate Dynamics*, *47*, 1367–1381. doi: 10.1007/s00382-015-2907-4

Lewis, E. L., & Perkin, R. G. (1986). Ice pumps and their rates. *Journal of Geophysical Research: Oceans*, *91*(C10), 11756–11762. doi: 10.1029/JC091iC10p11756

Li, Y., McGillicuddy Jr, D. J., Dinniman, M. S., & Klinck, J. M. (2017). Processes influencing formation of low-salinity high-biomass lenses near the edge of the Ross Ice Shelf. *Journal of Marine Systems*, *166*, 108–119. doi: 10.1016/j.jmarsys.2016.07.002

Ligtenberg, S. R. M., Helsen, M. M., & van den Broeke, M. R. (2011). An improved semi-empirical model for the densification of Antarctic firn. *The Cryosphere*, *5*(4), 809–819. doi: 10.5194/tc-5-809-2011

Liu, Y., Moore, J. C., Cheng, X., Gladstone, R. M., Bassis, J. N., Liu, H., Wen, J., & Hui, F. (2015). Ocean-driven thinning enhances iceberg calving and retreat of Antarctic ice shelves. *Proceedings of the National Academy of Sciences*, *112*(11), 3263–3268. doi: 10.1073/pnas.1415137112

MacAyeal, D. R., Okal, E. A., Aster, R. C., Bassis, J. N., Brunt, K. M., Cathles, L. M., Drucker, R., Fricker, H. A., Kim, Y.-J., Martin, S., Okal, M. H., Sergienko, O. V., Sponsler, M. P., & Thom, J. E. (2006). Transoceanic wave propagation links iceberg calving margins of Antarctica with storms in tropics and Northern Hemisphere. *Geophysical Research Letters*, *33*(17), L17502. doi: 10.1029/2006GL027235

MacAyeal, D. R., Okal, M. H., Thom, J. E., Brunt, K. M., Kim, Y.-J., & Bliss, A. K. (2008). Tabular iceberg collisions within the coastal regime. *Journal of Glaciology*, *54*(185), 371–386. doi: 10.3189/002214308784886180

MacGregor, J. A., Boisvert, L. N., Medley, B., Petty, A. A., Harbeck, J. P., Bell, R. E., Blair, J. B., Blanchard-Wrigglesworth, E., Buckley, E. M., Christoffersen, M. S., Cochran, J. R., Csathó, B. M., de Marco, E. L., Dominguez, R. T., Fahnestock, M. A., Farrell, S. L., Gogineni, S. P., Greenbaum, J. S., Hansen, C. M., Hofton, M. A., Holt, J. W., Jezek, K. C., Koenig, L. S., Kurtz, N. T., Kwok, R., Larsen, C. F., Leuschen, C. J., Locke, C. D., Manizade, S. S., Martin, S., Neumann, T. A., Nowicki, S. M. J., Paden, J. D., Richter-Menge, J. A., Rignot, E. J., Rodríguez-Morales, F., Siegfried, M. R., Smith, B. E., Sonntag, J. G., Studinger, M., Tinto, K. J., Truffer, M., Wagner, T. P., Woods, J. E., Young, D. A., & Yungel, J. K. (2021). The scientific legacy of NASA's Operation IceBridge. *Reviews of Geophysics*, *59*,

e2020RG000712. doi: 10.1029/2020RG000712

MacGregor, J. A., Catania, G. A., Markowski, M. S., & Andrews, A. G. (2012). Widespread rifting and retreat of ice-shelf margins in the eastern Amundsen Sea Embayment between 1972 and 2011. *Journal of Glaciology*, *58*(209), 458–466. doi: 10.3189/2012JoG11J262

Magruder, L. A., Brunt, K. M., & Alonzo, M. (2020). Early ICESat-2 on-orbit geolocation validation using ground-based corner cube retro-reflectors. *Remote Sensing*, *12*(21), 3653. doi: 10.3390/rs12213653

Malyarenko, A., Robinson, N. J., Williams, M. J. M., & Langhorne, P. J. (2019). A wedge mechanism for summer surface water inflow into the Ross Ice Shelf cavity. *Journal of Geophysical Research: Oceans*, *124*(2), 1196–1214. doi: 10.1029/2018JC014594

Markus, T., Neumann, T., Martino, A., Abdalati, W., Brunt, K., Csatho, B., Farrell, S., Fricker, H., Gardner, A., Harding, D., Jasinski, M., Kwok, R., Magruder, L., Lubin, D., Luthcke, S., Morison, J., Nelson, R., Neuenschwander, A., Palm, S., Popescu, S., Shum, C., Schutz, B. E., Smith, B., Yang, Y., & Zwally, J. (2017). The Ice, Cloud, and land Elevation Satellite-2 (ICESat-2): Science requirements, concept, and implementation. *Remote Sensing of Environment*, *190*, 260–273. doi: 10.1016/j.rse.2016.12.029

Martin, S., Drucker, R. S., & Kwok, R. (2007). The areas and ice production of the western and central Ross Sea polynyas, 1992–2002, and their relation to the B-15 and C-19 iceberg events of 2000 and 2002. *Journal of Marine Systems*, *68*(1–2), 201–214. doi: 10.1016/j.jmarsys.2006.11.008

Massom, R. A., & Stammerjohn, S. E. (2010). Antarctic sea ice change and variability—physical and ecological implications. *Polar Science*, *4*(2), 149–186. doi: 10.1016/j.polar.2010.05.001

Medley, B., Neumann, T., Zwally, H. J., Smith, B. E., & Stevens, C. M. (2022a). NASA GSFC Firn Densification Model version 1.2.1 (GSFC-FDMv1.2.1) for the Greenland and Antarctic ice sheets: 1980–2022 (Version 1.2.1, Release 2) [Data set]. *Zenodo*. doi: 10.5281/zenodo.7221954

Medley, B., Neumann, T. A., Zwally, H. J., Smith, B. E., & Stevens, C. M. (2022b). Simulations of firn processes over the Greenland and Antarctic ice sheets: 1980–2021. *The Cryosphere*, *16*(10), 3971–4011. doi: 10.5194/tc-16-3971-2022

Meier, W. N., Fetterer, F., Savoie, M., Mallory, S., Duerr, R., & Stroeve, J. (2017). NOAA/NSIDC climate data record of passive microwave sea ice concentration (Version 3) [Data set]. *National Snow and Ice Data Center*. doi: 10.7265/N59P2ZTG

Meier, W. N., Fetterer, F., Windnagel, A. K., & Stewart, J. S. (2021). NOAA/NSIDC climate data record of passive microwave sea ice concentration (Version 4) [Data set]. *National*

Snow and Ice Data Center. doi: 10.7265/efmz-2t65

Meredith, M., Sommerkorn, M., Cassotta, S., Derksen, C., Ekaykin, A., Hollowed, A., Kofinas, G., Mackintosh, A., Melbourne-Thomas, J., Muelbert, M. M. C., Ottersen, G., Pritchard, H., & Schuur, E. A. G. (2019). Polar regions. In H.-O. Pörtner, D. C. Roberts, V. Masson-Delmotte, P. Zhai, M. Tignor, E. Poloczanska, K. Mintenbeck, A. Alegría, M. Nicolai, A. Okem, J. Petzold, B. Rama, & N. M. Weyer (Eds.), *IPCC Special Report on the Ocean and Cryosphere in a Changing Climate* (pp. 203–320). Cambridge University Press. doi: 10.1017/9781009157964.005

Merino, N., Le Sommer, J., Durand, G., Jourdain, N. C., Madec, G., Mathiot, P., & Tournadre, J. (2016). Antarctic icebergs melt over the Southern Ocean: Climatology and impact on sea ice. *Ocean Modelling*, *104*, 99–110. doi: 10.1016/j.ocemod.2016.05.001

Mitrovica, J. X., Gomez, N., Morrow, E., Hay, C., Latychev, K., & Tamisiea, M. E. (2011). On the robustness of predictions of sea level fingerprints. *Geophysical Journal International*, *187*(2), 729–742. doi: 10.1111/j.1365-246X.2011.05090.x

Moholdt, G., Padman, L., & Fricker, H. A. (2014). Basal mass budget of Ross and Filchner-Ronne ice shelves, Antarctica, derived from Lagrangian analysis of ICESat altimetry. *Journal of Geophysical Research: Earth Surface*, *119*(11), 2361–2380. doi: 10.1002/2014JF003171

Morlighem, M., Rignot, E., Binder, T., Blankenship, D., Drews, R., Eagles, G., Eisen, O., Ferraccioli, F., Forsberg, R., Fretwell, P., Goel, V., Greenbaum, J. S., Gudmundsson, H., Guo, J., Helm, V., Hofstede, C., Howat, I., Humbert, A., Jokat, W., Karlsson, N. B., Lee, W. S., Matsuoka, K., Millan, R., Mouginot, J., Paden, J., Pattyn, F., Roberts, J., Rosier, S., Ruppel, A., Seroussi, H., Smith, E. C., Steinhage, D., Sun, B., van den Broeke, M. R., van Ommen, T. D., van Wessem, M., & Young, D. A. (2020). Deep glacial troughs and stabilizing ridges unveiled beneath the margins of the Antarctic Ice Sheet. *Nature Geoscience*, *13*(2), 132–137. doi: 10.1038/s41561-019-0510-8

Mosbeux, C., Padman, L., Klein, E., Bromirski, P. D., & Fricker, H. A. (2023). Seasonal variability in Antarctic ice shelf velocities forced by sea surface height variations. *The Cryosphere*, *17*(7), 2585–2606. doi: 10.5194/tc-17-2585-2023

Mosbeux, C., Wagner, T. J. W., Becker, M. K., & Fricker, H. A. (2020). Viscous and elastic buoyancy stresses as drivers of ice-shelf calving. *Journal of Glaciology*, *66*(258), 643–657. doi: 10.1017/jog.2020.35

Mouginot, J., Rignot, E., Scheuchl, B., & Millan, R. (2017). Comprehensive annual ice sheet velocity mapping using Landsat-8, Sentinel-1, and RADARSAT-2 data. *Remote Sensing*, *9*(4), 364. doi: 10.3390/rs9040364

Mouginot, J., Scheuchl, B., & Rignot, E. (2012). Mapping of ice motion in Antarctica using synthetic-aperture radar data. *Remote Sensing*, *4*(9), 2753–2767. doi: 10.3390/rs4092753

Mouginot, J., Scheuchl, B., & Rignot, E. (2017). MEaSUREs Antarctic boundaries for IPY 2007–2009 from satellite radar (Version 2) [Data set]. *NASA National Snow and Ice Data Center Distributed Active Archive Center*. doi: 10.5067/AXE4121732AD

Nakayama, Y., Manucharyan, G., Zhang, H., Dutrieux, P., Torres, H. S., Klein, P., Seroussi, H., Schodlok, M., Rignot, E., & Menemenlis, D. (2019). Pathways of ocean heat towards Pine Island and Thwaites grounding lines. *Scientific Reports*, *9*(1), 16649. doi: 10.1038/s41598-019-53190-6

Neal, C. S. (1979). The dynamics of the Ross Ice Shelf revealed by radio echo-sounding. *Journal of Glaciology*, *24*(90), 295–307. doi: 10.3189/S0022143000014817

Nerem, R. S., Beckley, B. D., Fasullo, J. T., Hamlington, B. D., Masters, D., & Mitchum, G. T. (2018). Climate-change-driven accelerated sea-level rise detected in the altimeter era. *Proceedings of the National Academy of Sciences*, *115*(9), 2022–2025. doi: 10.1073/pnas.1717312115

Neumann, T. A., Brenner, A., Hancock, D., Robbins, J., Saba, J., Harbeck, K., Gibbons, A., Lee, J., Luthcke, S. B., & Rebold, T. (2020). ATLAS/ICESat-2 L2A global geolocated photon data (Version 3) [Data set]. *NASA National Snow and Ice Data Center Distributed Active Archive Center*. doi: 10.5067/ATLAS/ATL03.003

Neumann, T. A., Martino, A. J., Markus, T., Bae, S., Bock, M. R., Brenner, A. C., Brunt, K. M., Cavanaugh, J., Fernandes, S. T., Hancock, D. W., Harbeck, K., Lee, J., Kurtz, N. T., Luers, P. J., Luthcke, S. B., Magruder, L., Pennington, T. A., Ramos-Izquierdo, L., Rebold, T., Skoog, J., & Thomas, T. C. (2019). The Ice, Cloud, and land Elevation Satellite-2 mission: A global geolocated photon product derived from the Advanced Topographic Laser Altimeter System. *Remote Sensing of Environment*, *233*, 111325. doi: 10.1016/j.rse.2019.111325

Oppenheimer, M., Glavovic, B. C., Hinkel, J., van de Wal, R., Magnan, A. K., Abd-Elgawad, A., Cai, R., Cifuentes-Jara, M., DeConto, R. M., Ghosh, T., Hay, J., Isla, F., Marzeion, B., Meyssignac, B., & Sebesvari, Z. (2019). Sea level rise and implications for low-lying islands, coasts and communities. In H.-O. Pörtner, D. C. Roberts, V. Masson-Delmotte, P. Zhai, M. Tignor, E. Poloczanska, K. Mintenbeck, A. Alegría, M. Nicolai, A. Okem, J. Petzold, B. Rama, & N. M. Weyer (Eds.), *IPCC Special Report on the Ocean and Cryosphere in a Changing Climate* (pp. 321–445). Cambridge University Press. doi: 10.1017/9781009157964.006

Orheim, O. (1987). Evolution of under water sides of ice shelves and icebergs. *Annals of Glaciology*, *9*, 176–182. doi: 10.3189/S0260305500000574

Padman, L., Fricker, H. A., Coleman, R., Howard, S., & Erofeeva, L. (2002). A new tide model for the Antarctic ice shelves and seas. *Annals of Glaciology*, *34*, 247–254. doi:

10.3189/172756402781817752

Paolo, F. S., Fricker, H. A., & Padman, L. (2015). Volume loss from Antarctic ice shelves is accelerating. *Science*, *348*(6232), 327–331. doi: 10.1126/science.aaa0940

Parrish, C. E., Magruder, L. A., Neuenschwander, A. L., Forfinski-Sarkozi, N., Alonzo, M., & Jasinski, M. (2019). Validation of ICESat-2 ATLAS bathymetry and analysis of ATLAS's bathymetric mapping performance. *Remote Sensing*, *11*(14), 1634. doi: 10.3390/rs11141634

Pavlis, N. K., Holmes, S. A., Kenyon, S. C., & Factor, J. K. (2012). The development and evaluation of the Earth Gravitational Model 2008 (EGM2008). *Journal of Geophysical Research: Solid Earth*, *117*(B4). doi: 10.1029/2011JB008916

Peng, G., Meier, W. N., Scott, D. J., & Savoie, M. H. (2013). A long-term and reproducible passive microwave sea ice concentration data record for climate studies and monitoring. *Earth System Science Data*, *5*(2), 311–318. doi: 10.5194/essd-5-311-2013

Porter, D. F., Springer, S. R., Padman, L., Fricker, H. A., Tinto, K. J., Riser, S. C., Bell, R. E., & the ROSETTA-Ice Team. (2019). Evolution of the seasonal surface mixed layer of the Ross Sea, Antarctica, observed with autonomous profiling floats. *Journal of Geophysical Research: Oceans*, *124*(7), 4934–4953. doi: 10.1029/2018JC014683

Pritchard, H. D., Ligtenberg, S. R. M., Fricker, H. A., Vaughan, D. G., van den Broeke, M. R., & Padman, L. (2012). Antarctic ice-sheet loss driven by basal melting of ice shelves. *Nature*, *484*(7395), 502–505. doi: 10.1038/nature10968

Qi, M., Liu, Y., Liu, J., Cheng, X., Lin, Y., Feng, Q., Shen, Q., & Yu, Z. (2021). A 15-year circum-Antarctic iceberg calving dataset derived from continuous satellite observations. *Earth System Science Data*, *13*(9), 4583–4601. doi: 10.5194/essd-13-4583-2021

Reeh, N. (1968). On the calving of ice from floating glaciers and ice shelves. *Journal of Glaciology*, *7*(50), 215–232. doi: 10.3189/S0022143000031014

Reese, R., Gudmundsson, G. H., Levermann, A., & Winkelmann, R. (2018). The far reach of ice-shelf thinning in Antarctica. *Nature Climate Change*, *8*(1), 53–57. doi: 10.1038/s41558-017-0020-x

Reid, P. A., & Massom, R. A. (2022). Change and variability in Antarctic coastal exposure, 1979–2020. *Nature Communications*, *13*(1), 1164. doi: 10.1038/s41467-022-28676-z

Rignot, E., Jacobs, S., Mouginot, J., & Scheuchl, B. (2013). Ice-shelf melting around Antarctica. *Science*, *341*(6143), 266–270. doi: 10.1126/science.1235798

Rignot, E., Mouginot, J., Morlighem, M., Seroussi, H., & Scheuchl, B. (2014). Widespread,

rapid grounding line retreat of Pine Island, Thwaites, Smith, and Kohler glaciers, West Antarctica, from 1992 to 2011. *Geophysical Research Letters*, *41*(10), 3502–3509. doi: 10.1002/2014GL060140

Rignot, E., Mouginot, J., & Scheuchl, B. (2011a). Antarctic grounding line mapping from differential satellite radar interferometry. *Geophysical Research Letters*, *38*(10). doi: 10.1029/2011GL047109

Rignot, E., Mouginot, J., & Scheuchl, B. (2011b). Ice flow of the Antarctic Ice Sheet. *Science*, *333*(6048), 1427–1430. doi: 10.1126/science.1208336

Rignot, E., Mouginot, J., & Scheuchl, B. (2017). MEaSUREs InSAR-based Antarctica ice velocity map (Version 2) [Data set]. *NASA National Snow and Ice Data Center Distributed Active Archive Center*. doi: 10.5067/D7GK8F5J8M8R

Roach, L. A., Dörr, J., Holmes, C. R., Massonnet, F., Blockley, E. W., Notz, D., Rackow, T., Raphael, M. N., O'Farrell, S. P., Bailey, D. A., & Bitz, C. M. (2020). Antarctic sea ice area in CMIP6. *Geophysical Research Letters*, *47*(9), e2019GL086729. doi: 10.1029/2019GL086729

Robin, G. d. Q. (1979). Formation, flow, and disintegration of ice shelves. *Journal of Glaciology*, *24*(90), 259–271. doi: 10.3189/S0022143000014787

Rott, H., Rack, W., Skvarca, P., & De Angelis, H. (2002). Northern Larsen Ice Shelf, Antarctica: Further retreat after collapse. *Annals of Glaciology*, *34*, 277–282. doi: 10.3189/172756402781817716

Sayag, R., & Worster, M. G. (2013). Elastic dynamics and tidal migration of grounding lines modify subglacial lubrication and melting. *Geophysical Research Letters*, *40*(22), 5877–5881. doi: 10.1002/2013GL057942

Scambos, T., Hulbe, C., & Fahnestock, M. (2003). Climate-induced ice shelf disintegration in the Antarctic Peninsula. In E. Domack, A. Levente, A. Burnet, R. Bindschadler, P. Convey, & M. Kirby (Eds.), *Antarctic Peninsula climate variability: Historical and paleoenvironmental perspectives* (pp. 79–92). American Geophysical Union. doi: 10.1029/AR079p0079

Scambos, T., Ross, R., Bauer, R., Yermolin, Y., Skvarca, P., Long, D., Bohlander, J., & Haran, T. (2008). Calving and ice-shelf break-up processes investigated by proxy: Antarctic tabular iceberg evolution during northward drift. *Journal of Glaciology*, *54*(187), 579–591. doi: 10.3189/002214308786570836

Scambos, T., Sergienko, O., Sargent, A., MacAyeal, D., & Fastook, J. (2005). ICESat profiles of tabular iceberg margins and iceberg breakup at low latitudes. *Geophysical Research Letters*, *32*(23), L23S09. doi: 10.1029/2005GL023802

Scambos, T., Wallin, B., & Bohlander, J. (2022). Images of Antarctic ice shelves (Version 2) [Data set]. *NASA National Snow and Ice Data Center Distributed Active Archive Center*. doi: 10.5067/W87VCY3CW0MJ

Scambos, T. A., Bohlander, J. A., Shuman, C. A., & Skvarca, P. (2004). Glacier acceleration and thinning after ice shelf collapse in the Larsen B embayment, Antarctica. *Geophysical Research Letters*, *31*(18), L18402. doi: 10.1029/2004GL020670

Scambos, T. A., Haran, T. M., Fahnestock, M. A., Painter, T. H., & Bohlander, J. (2007). MODIS-based Mosaic of Antarctica (MOA) data sets: Continent-wide surface morphology and snow grain size. *Remote Sensing of Environment*, *111*(2–3), 242–257. doi: 10.1016/j.rse.2006.12.020

Scheick, J., & the icepyx Development Team. (2019). icepyx: Python tools for obtaining and working with ICESat-2 data [Software]. Retrieved from `https://github.com/icesat2py/icepyx`

Schoof, C. (2007). Ice sheet grounding line dynamics: Steady states, stability, and hysteresis. *Journal of Geophysical Research: Earth Surface*, *112*(F3). doi: 10.1029/2006JF000664

Schröder, L., Horwath, M., Dietrich, R., Helm, V., van den Broeke, M. R., & Ligtenberg, S. R. M. (2019). Four decades of Antarctic surface elevation changes from multi-mission satellite altimetry. *The Cryosphere*, *13*(2), 427–449. doi: 10.5194/tc-13-427-2019

Schutz, B. E., Zwally, H. J., Shuman, C. A., Hancock, D., & DiMarzio, J. P. (2005). Overview of the ICESat mission. *Geophysical Research Letters*, *32*(21), L21S01. doi: 10.1029/2005GL024009

Sergienko, O. V. (2010). Elastic response of floating glacier ice to impact of long-period ocean waves. *Journal of Geophysical Research: Earth Surface*, *115*(F4), F04028. doi: 10.1029/2010JF001721

Shepherd, A., Fricker, H. A., & Farrell, S. L. (2018). Trends and connections across the Antarctic cryosphere. *Nature*, *558*(7709), 223–232. doi: 10.1038/s41586-018-0171-6

Shepherd, A., Ivins, E., Rignot, E., Smith, B., van den Broeke, M., Velicogna, I., Whitehouse, P., Briggs, K., Joughin, I., Krinner, G., Nowicki, S., Payne, T., Scambos, T., Schlegel, N., A, G., Agosta, C., Ahlstrøm, A., Babonis, G., Barletta, V., Blazquez, A., Bonin, J., Csatho, B., Cullather, R., Felikson, D., Fettweis, X., Forsberg, R., Gallee, H., Gardner, A., Gilbert, L., Groh, A., Gunter, B., Hanna, E., Harig, C., Helm, V., Horvath, A., Horwath, M., Khan, S., Kjeldsen, K. K., Konrad, H., Langen, P., Lecavalier, B., Loomis, B., Luthcke, S., McMillan, M., Melini, D., Mernild, S., Mohajerani, Y., Moore, P., Mouginot, J., Moyano, G., Muir, A., Nagler, T., Nield, G., Nilsson, J., Noel, B., Otosaka, I., Pattle, M. E., Peltier, W. R., Pie, N., Rietbroek, R., Rott, H., Sandberg-Sørensen, L., Sasgen, I., Save, H., Scheuchl, B., Schrama, E., Schröder, L., Seo, K.-W., Simonsen, S., Slater, T., Spada, G., Sutterley, T.,

Talpe, M., Tarasov, L., van de Berg, W. J., van der Wal, W., van Wessem, M., Vishwakarma, B. D., Wiese, D., & Wouters, B. (2018). Mass balance of the Antarctic Ice Sheet from 1992 to 2017. *Nature*, *558*(7709), 219–222. doi: 10.1038/s41586-018-0179-y

Shuman, C. A., Zwally, H. J., Schutz, B. E., Brenner, A. C., DiMarzio, J. P., Suchdeo, V. P., & Fricker, H. A. (2006). ICESat Antarctic elevation data: Preliminary precision and accuracy assessment. *Geophysical Research Letters*, *33*(7), L07501. doi: 10.1029/2005GL025227

Silvano, A., Foppert, A., Rintoul, S. R., Holland, P. R., Tamura, T., Kimura, N., Castagno, P., Falco, P., Budillon, G., Haumann, F. A., Garabato, A. C. N., & Macdonald, A. M. (2020). Recent recovery of Antarctic Bottom Water formation in the Ross Sea driven by climate anomalies. *Nature Geoscience*, *13*(12), 780–786. doi: 10.1038/s41561-020-00655-3

Smethie Jr, W. M., & Jacobs, S. S. (2005). Circulation and melting under the Ross Ice Shelf: Estimates from evolving CFC, salinity and temperature fields in the Ross Sea. *Deep Sea Research Part I: Oceanographic Research Papers*, *52*(6), 959–978. doi: 10.1016/j.dsr.2004.11.016

Smith, B., Adusumilli, S., Csathó, B. M., Felikson, D., Fricker, H. A., Gardner, A., Holschuh, N., Lee, J., Nilsson, J., Paolo, F. S., Siegfried, M. R., Sutterley, T., & the ICESat-2 Science Team. (2021). ATLAS/ICESat-2 L3A land ice height (Version 5) [Data set]. *NASA National Snow and Ice Data Center Distributed Active Archive Center*. doi: 10.5067/ATLAS/ATL06.005

Smith, B., Fricker, H. A., Gardner, A., Siegfried, M. R., Adusumilli, S., Csathó, B. M., Holschuh, N., Nilsson, J., Paolo, F. S., & the ICESat-2 Science Team. (2020). ATLAS/ICESat-2 L3A land ice height (Version 3) [Data set]. *NASA National Snow and Ice Data Center Distributed Active Archive Center*. doi: 10.5067/ATLAS/ATL06.003

Smith, B., Fricker, H. A., Gardner, A. S., Medley, B., Nilsson, J., Paolo, F. S., Holschuh, N., Adusumilli, S., Brunt, K., Csatho, B., Harbeck, K., Markus, T., Neumann, T., Siegfried, M. R., & Zwally, H. J. (2020). Pervasive ice sheet mass loss reflects competing ocean and atmosphere processes. *Science*, *368*(6496), 1239–1242. doi: 10.1126/science.aaz5845

Smith, B., Fricker, H. A., Holschuh, N., Gardner, A. S., Adusumilli, S., Brunt, K. M., Csatho, B., Harbeck, K., Huth, A., Neumann, T., Nilsson, J., & Siegfried, M. R. (2019). Land ice height-retrieval algorithm for NASA's ICESat-2 photon-counting laser altimeter. *Remote Sensing of Environment*, *233*, 111352. doi: 10.1016/j.rse.2019.111352

Smith, B., Sutterley, T., Dickinson, S., Jelley, B. P., Felikson, D., Neumann, T. A., Fricker, H. A., Gardner, A., Padman, L., Markus, T., Kurtz, N., Bhardwaj, S., Hancock, D., & Lee, J. (2022). ATLAS/ICESat-2 L3B gridded Antarctic and Arctic land ice height (Version 2) [Data set]. *NASA National Snow and Ice Data Center Distributed Active Archive Center*. doi: 10.5067/ATLAS/ATL14.002

Smith, B. E., Fricker, H. A., Joughin, I. R., & Tulaczyk, S. (2009). An inventory of active subglacial lakes in Antarctica detected by ICESat (2003–2008). *Journal of Glaciology*, *55*(192), 573–595. doi: 10.3189/002214309789470879

Spector, P., Stone, J., Cowdery, S. G., Hall, B., Conway, H., & Bromley, G. (2017). Rapid early-Holocene deglaciation in the Ross Sea, Antarctica. *Geophysical Research Letters*, *44*(15), 7817–7825. doi: 10.1002/2017GL074216

Stevens, C., Hulbe, C., Brewer, M., Stewart, C., Robinson, N., Ohneiser, C., & Jendersie, S. (2020). Ocean mixing and heat transport processes observed under the Ross Ice Shelf control its basal melting. *Proceedings of the National Academy of Sciences*, *117*(29), 16799–16804. doi: 10.1073/pnas.1910760117

Stewart, C. L., Christoffersen, P., Nicholls, K. W., Williams, M. J. M., & Dowdeswell, J. A. (2019). Basal melting of Ross Ice Shelf from solar heat absorption in an ice-front polynya. *Nature Geoscience*, *12*(6), 435–440. doi: 10.1038/s41561-019-0356-0

Sutherland, D. A., Jackson, R. H., Kienholz, C., Amundson, J. M., Dryer, W. P., Duncan, D., Eidam, E. F., Motyka, R. J., & Nash, J. D. (2019). Direct observations of submarine melt and subsurface geometry at a tidewater glacier. *Science*, *365*(6451), 369–374. doi: 10.1126/science.aax3528

Sutterley, T. C., Alley, K., Brunt, K., Howard, S., Padman, L., & Siegfried, M. (2017). pyTMD: Python-based tidal prediction software [Software]. *Zenodo*. doi: 10.5281/zenodo.5555395

Thomas, R. H. (1979). Ice shelves: A review. *Journal of Glaciology*, *24*(90), 273–286. doi: 10.3189/S0022143000014799

Tinto, K. J., Padman, L., Siddoway, C. S., Springer, S. R., Fricker, H. A., Das, I., Caratori Tontini, F., Porter, D. F., Frearson, N. P., Howard, S. L., Siegfried, M. R., Mosbeux, C., Becker, M. K., Bertinato, C., Boghosian, A., Brady, N., Burton, B. L., Chu, W., Cordero, S. I., Dhakal, T., Dong, L., Gustafson, C. D., Keeshin, S., Locke, C., Lockett, A., O'Brien, G., Spergel, J. J., Starke, S. E., Tankersley, M., Wearing, M. G., & Bell, R. E. (2019). Ross Ice Shelf response to climate driven by the tectonic imprint on seafloor bathymetry. *Nature Geoscience*, *12*(6), 441–449. doi: 10.1038/s41561-019-0370-2

Tournadre, J., Bouhier, N., Girard-Ardhuin, F., & Rémy, F. (2016). Antarctic icebergs distributions 1992–2014. *Journal of Geophysical Research: Oceans*, *121*(1), 327–349. doi: 10.1002/2015JC011178

Trusel, L. D., Frey, K. E., Das, S. B., Karnauskas, K. B., Kuipers Munneke, P., van Meijgaard, E., & van den Broeke, M. R. (2015). Divergent trajectories of Antarctic surface melt under two twenty-first-century climate scenarios. *Nature Geoscience*, *8*(12), 927–932. doi: 10.1038/ngeo2563

van den Broeke, M. (2008). Depth and density of the Antarctic firn layer. *Arctic, Antarctic, and Alpine Research*, *40*(2), 432–438. doi: 10.1657/1523-0430(07-021)[BROEKE]2.0.CO;2

Vaughan, D. G. (1995). Tidal flexure at ice shelf margins. *Journal of Geophysical Research: Solid Earth*, *100*(B4), 6213–6224. doi: 10.1029/94JB02467

Wagner, T. J. W., James, T. D., Murray, T., & Vella, D. (2016). On the role of buoyant flexure in glacier calving. *Geophysical Research Letters*, *43*(1), 232–240A. doi: 10.1002/2015GL067247

Wagner, T. J. W., Wadhams, P., Bates, R., Elosegui, P., Stern, A., Vella, D., Abrahamsen, E. P., Crawford, A., & Nicholls, K. W. (2014). The "footloose" mechanism: Iceberg decay from hydrostatic stresses. *Geophysical Research Letters*, *41*(15), 5522–5529. doi: 10.1002/2014GL060832

Walker, C. C., Becker, M. K., & Fricker, H. A. (2021). A high resolution, three-dimensional view of the D-28 calving event from Amery Ice Shelf with ICESat-2 and satellite imagery. *Geophysical Research Letters*, *48*(3), e2020GL091200. doi: 10.1029/2020GL091200

Walker, C. C., & Gardner, A. S. (2019). Evolution of ice shelf rifts: Implications for formation mechanics and morphological controls. *Earth and Planetary Science Letters*, *526*, 115764. doi: 10.1016/j.epsl.2019.115764

Wise, M. G., Dowdeswell, J. A., Jakobsson, M., & Larter, R. D. (2017). Evidence of marine ice-cliff instability in Pine Island Bay from iceberg-keel plough marks. *Nature*, *550*(7677), 506–510. doi: 10.1038/nature24458

Wuite, J., Nagler, T., Gourmelen, N., Escorihuela, M. J., Hogg, A. E., & Drinkwater, M. R. (2019). Sub-annual calving front migration, area change and calving rates from swath mode CryoSat-2 altimetry, on Filchner-Ronne Ice Shelf, Antarctica. *Remote Sensing*, *11*(23), 2761. doi: 10.3390/rs11232761

Yokoyama, Y., Anderson, J. B., Yamane, M., Simkins, L. M., Miyairi, Y., Yamazaki, T., Koizumi, M., Suga, H., Kusahara, K., Prothro, L., Hasumi, H., Southon, J. R., & Ohkouchi, N. (2016). Widespread collapse of the Ross Ice Shelf during the late Holocene. *Proceedings of the National Academy of Sciences*, *113*(9), 2354–2359. doi: 10.1073/pnas.1516908113

Zotikov, I. A., Zagorodnov, V. S., & Raikovsky, J. V. (1980). Core drilling through the Ross Ice Shelf (Antarctica) confirmed basal freezing. *Science*, *207*(4438), 1463–1465. doi: 10.1126/science.207.4438.1463

Zwally, H. J., Schutz, R., Hancock, D., & DiMarzio, J. (2014). GLAS/ICESat L2 global Antarctic and Greenland ice sheet altimetry data (HDF5) (Version 34) [Data set]. *NASA National Snow and Ice Data Center Distributed Active Archive Center*. doi: 10.5067/ICESAT/GLAS/DATA209